Missouri S&T Library and Learning Resources

Scholars' Mine

Doctoral Dissertations | Student Theses and Dissertations

Fall 2017

Continuous focusing and separation of microparticles with acoustic and magnetic fields

Ran Zhou

Follow this and additional works at: https://scholarsmine.mst.edu/doctoral_dissertations

 Part of the Mechanical Engineering Commons

Department: Mechanical and Aerospace Engineering

Recommended Citation

Zhou, Ran, "Continuous focusing and separation of microparticles with acoustic and magnetic fields" (2017). *Doctoral Dissertations*. 2636.
https://scholarsmine.mst.edu/doctoral_dissertations/2636

This thesis is brought to you by Scholars' Mine, a service of the Missouri S&T Library and Learning Resources. This work is protected by U. S. Copyright Law. Unauthorized use including reproduction for redistribution requires the permission of the copyright holder. For more information, please contact scholarsmine@mst.edu.

CONTINUOUS FOCUSING AND SEPARATION OF MICROPARTICLES WITH ACOUSTIC AND MAGNETIC FIELDS

by

RAN ZHOU

A DISSERTATION

Presented to the Graduate Faculty of the

MISSOURI UNIVERSITY OF SCIENCE AND TECHNOLOGY

In Partial Fulfillment of the Requirements for the Degree

DOCTOR OF PHILOSOPHY

in

MECHANICAL ENGINEERING

2017

Approved by

Cheng Wang
K. M. Isaac
K. Chandrashekhara
Kelly Homan
Chang-Soo Kim

Copyright 2017

RAN ZHOU

All Rights Reserved

PUBLICATION DISSERTATION OPTION

This dissertation consists of the following five articles that have been published as follows:

Paper I. Pages 6–29 have been published in Journal of Micromechanics and Microengineering.

Paper II. Pages 30–56 have been published in Microfluidics and Nanofluidics.

Paper III. Pages 57–84 have been published in Biomicrofluidics.

Paper IV. Pages 85–115 have been published in Microfluidics and Nanofluidics.

Paper V. Pages 116–134 have been published in Lab on a Chip.

ABSTRACT

Microfluidics enables a diverse range of manipulations (e.g., focusing, separating, trapping, and enriching) of micrometer-sized objects, and has played an increasingly important role for applications that involve single cell biology and the detection and diagnosis of diseases. In microfluidic devices, methods that are commonly used to manipulate cells or particles include the utilization of hydrodynamic effects and externally applied field gradients that induce forces on cells/particles, such as electrical fields, optical fields, magnetic fields, and acoustic fields.

However, these conventional methods often involve complex designs or strongly depend on the properties of the flow medium or the interaction between the fluid and fluidic channels, so this dissertation aims to propose and demonstrate novel and low-cost techniques to fabricate microfluidic devices to separate microparticles with different sizes, materials and shapes by the optimized acoustic and magnetic fields. The first method is to utilize acoustic bubble-enhanced pinched flow for microparticle separation; the microfluidic separation of magnetic particles with soft magnetic microstructures is achieved in the second part; the third technique separates and focuses microparticles by multiphase ferrofluid flows; the fourth method realizes the fabrication and integration of microscale permanent magnets for particle separation in microfluidics; magnetic separation of microparticles by shape is proposed in the fifth technique.

The methods demonstrated in this dissertation not only address some of the limitations of conventional microdevices, but also provide simple and efficient method for the separation of microparticles and biological cells with different sizes, materials and shapes, and will benefit practical microfluidic platforms concerning micron sized particles/cells.

ACKNOWLEDGMENTS

First and foremost, I would like to express my sincere gratitude to my advisor, Dr. Cheng Wang, for his encouragement, insightful guidance, and support during my graduate study at Missouri University of Science and Technology. He patiently guided me through every stage of my research while granted me a great deal of independence. His encouragement endowed me with tremendous confidence in exploring unknown scientific territory and challenging myself to be my best. His diligence and rigorous altitude to research and work will have a significant influence on my future life. It has been a privilege and a great honor to have worked with him.

I would also like to extend my appreciation to all my dissertation committee members, Dr. K. M. Isaac, Dr. K. Chandrashekhara, Dr. Kelly Homan and Dr. Chang-Soo Kim. Without their guidance and valuable comments, it is impossible for me to complete my dissertation.

The dissertation was supported by the Department of Mechanical and Aerospace Engineering at Missouri University of Science and Technology, Rolla, Missouri, which are gratefully acknowledged. I would like to express my deep thanks to my labmates and my friends, Mr. Jie Zhang, Mr. Christopher Sobecki, Mr. Ziyan Zhang, Mr. David Brames, Mr. Ning Liu, Mr. Wedam Nyaaba, Mr. Chao Zhang, Ms. Li Guan, Mr. James Werner, Mr. Rui Liu for their support during my study in Rolla.

Last but not the least, I wish to extend my special and sincere thanks to my parents for their love and unwavering support.

TABLE OF CONTENTS

Page

SECTION

LIST OF ILLUSTRATIONS

PAPER II

PAPER III

SECTION

1. INTRODUCTION

For many lab-on-a-chip and microfluidic platforms, in particular those designed for biology, biomedical and medicine applications, separation of micron-sized particles is a crucial prerequisite step for the downstream processing steps [1, 2, 3, 4, 5]. The separation step provides the necessary purification, isolation and enrichment in order to allow the subsequent detection, quantification, characterization and diagnosis of the target objects, e.g. specific biological cells [6, 7, 8, 9]. Since most of the biological cells/particles of interest exist in fluid medium, separation in microfluidic environment has gathered great interest. Recent progress in microfluidics has provided a variety of novel techniques for micro-particle separation [10, 11, 12].

Generally, the separation strategies based on microfluidic technology can be classified into two categories: active and passive methods [13]. In the former, external force fields, for example electric [14, 15, 16], optical [17, 18], and magnetic forces [19, 20] are utilized to cause different movements among micron-sized objects that have different physical properties including size, conductivity, and magnetic susceptibility. For the passive techniques, the separation relies on the proper design of hydrodynamic flows, fluidic networks, placement of obstacles and filters. Some examples of passive techniques include pinched flow fractionation, deterministic lateral displacement [21], hydrodynamic filtering [22], and inertial separation [23, 24]. Passive methods based on hydrodynamic effects often rely on the appropriate channel designs to direct the particles of different sizes into separate flow streamlines. The dimensions of the channels have implications for the applicable separation sizes. Therefore, this research will mainly discuss the continuous focusing and separation of microparticles with acoustic and magnetic fields.

On the one hand, acoustically driven microbubbles are an excellent agent to induce microscale hydrodynamic flows. Microbubble streaming flows have demonstrated a wide range of applications, including fluid pumping [25], mixing [26], particle focusing [27, 28], particle sorting [29] and biological cell trapping [30]. In previous work, the sorting of microparticles relies on a trap-and-release mechanism [29]. The superposition of bubble streaming and Poiseuille flows forms a closed upstream vortex. Large particles are trapped into the vortex, and released afterwards from the cluster. Due to the narrow focused particle trajectories, particles of different sizes are separated to different outlets [29]. This trap-and-release mechanism has also been utilized to focus microparticles [27]. In addition to steady streaming flow, the secondary Bjerknes force may also play an important role when the fluid and particle have different densities. The interplay between the drag force due to streaming flow and Bjerknes force allows attraction or repulsion between the particle and the bubble. This subtle and interesting mechanism has been exploited for versatile particle manipulation, including selective trapping and sorting of microparticle based on particle size and density [31].

On the other hand, magnetism and magnetic particles or beads have long been used for bioseparation applications in biomedical sciences and clinical medicines [32, 33]. For example, immunomagnetic separation (IMS) is a standard laboratory technique for isolating cells, proteins, and nucleic acids. In this technique, magnetic particles conjugated with antibodies bind to antigens of the targeted cells' surface, and thus allow the cells to be isolated, purified and collected with a mangetic force field. Over the last decade, magnetism has been integrated with microfluidics to harness the advantages of miniaturization, automation and integration, and the term "magnetofluidics" has been coined [19, 34, 35, 36, 37, 38]. The use of magnetofluidics for bioseparation has received growing interest due to a number of unique advantages: low cost, insensitivity to temperature or pH, and remote actuation without direct contact. The two general methods for utilizing magnetic fields are: positive and negative magnetophoresis. In positive magnetophoresis, magnetic particles migrate

towards regions of higher magnetic field gradient. Commonly, magnetic particles are deflected from the direction of laminar flow by a perpendicular magnetic field. The deflection velocity depends on the magnetic susceptibility, particle size, and flow rate. Thus, magnetic particles of different sizes can be separated from each other and from non-magnetic materials [39]. This mechanism has been used to trap cells by labeling the target bioparticles with functionalized magnetic beads [19]. In negative magnetophoresis, diamagnetic particles that are suspended in magnetic solutions are repelled away from regions of higher magnetic field gradients (e.g., magnet sources) due to magnetic buoyancy force [40]. Further, most synthetic and biological particles are diamagnetic; therefore, label-free manipulation can be attained with negative magnetophoresis for practical applications.

Till now, there have been lots of methods to manipulate, focus and separate microparticles and cells with microfluidics, but most conventional technologies without optimization have different shortcomings to achieve high-efficiency focusing and separation of microparticles for clinical and research use. Accordingly, the objective of this doctorate research is to develop novel methods for enhancing the separation performance of particles according to the difference in size, material and shape by using acoustic field and magnetic field. This project will also provide numerical models and simulations that can predict the device performance and guide the designs for practical applications.

2. ORGANIZATION OF DISSERTATION

Many technical developments have been made in this study on above research objectives. In this dissertation, only the five major developments are presented due to the page limit. Paper I focuses on the acoustic bubble enhanced pinched flow fractionation for microparticle separation. Paper II is an application of soft magnetic microstructures for the microfluidic separation of magnetic particles. Paper III is to use multiphase ferrofluid flows for micro-particle focusing and separation. Paper IV presents a simple and effective fabrication technique to integrate microscale permanent magnets for particle separation. Paper V proposes a novel method for magnetic separation of microparticles by shape.

All of the five articles share a same research topic: continuous focusing and separation of microparticles with acoustic and magnetic fields, while each of them has a different focus.

Paper I proposes and demonstrates a novel and simple technique to enhance the particle separation performance of conventional PFF devices. Our device integrates a microbubble element into the pinched segment to locally alter the flow behaviors. The method demonstrated in this work not only addresses some of the limitations of conventional PFF, but also benefits applications where flexible tuning of particle positions or separation is required due to the ease of changing driving voltage.

The soft magnetic microstructures is applied to microfluidic separation of magnetic particles with in Paper II. The method is based on a microsolidics technique. The mangetic microstructures are made by injecting and curing a mixture of iron powder and PDMS in a structural microchannel next to the fluidic channel. Various factors are investigated that influence the sorting performance, including the shape of iron-PDMS microstructure, mass

ratio of iron powder, microfluidic channel width and total flow rate. A numerical method is also developed that can predict the particle separation and show good agreement with experimental measurements.

To overcome the limitations associated existing techniques, a simple and novel strategy to achieve focusing and separating of diamagnetic microparticles with laminar fluid interfaces and micro-fabricated magnets are proposed in Paper III. In this technique, a ferrofluid and a non-magnetic fluid co-flowing in a microfluidic channel form a stable fluid interface. Under the magnetic fields from the neighboring microscale magnet, diamagnetic particles that are suspended in the ferrofluid phase migrate towards and accumulate at the fluid interface, leading to particle focusing. This mechanism can be further exploited to separate particles of different sizes.

In Paper IV, a miniaturized and integrated microfluidic device that can pull magnetic particles from one laminar flow path to another by applying local magnetic field gradients are proposed, and thus selectively remove them from flowing fluids. To accomplish this, high-gradient microscale magnet is fabricated and integrated at one side of a microfluidic channel by a simple single-layer and single-mask microsolidics fabrication technique.

In Paper V, a simple and effective mechanism that can achieve shape-based separation of magnetic particles in microscale flows were demonstrated. In this method, a uniform magnetic field is applied perpendicularly to the flow direction, and causes shape-dependent lateral migration of the particles. Using high-speed imaging, the rotational dynamics of the ellipsoidal particles are studied.

PAPER

I. ACOUSTIC BUBBLE ENHANCED PINCHED FLOW FRACTIONATION FOR MICROPARTICLE SEPARATION

Ran Zhou, Cheng Wang

Department of Mechanical & Aerospace Engineering

Missouri University of Science and Technology

Rolla, Missouri 65409

Tel: (573) 341-4636, Fax: (573) 341-4607

Email: wancheng@mst.edu

ABSTRACT

Pinched flow fractionation is a simple method for separating micron-sized particles by size, but has certain intrinsic limitations, e.g. requirement of a pinched segment similar to particle size and limited separation distance. In this paper, we developed an acoustic bubble enhanced pinched flow fractionation (PFF) method for microparticle separation. The proposed technique utilized microbubble streaming flows to overcome the limitations of conventional PFF. Our device has demonstrated separation of different sized microparticles (diameters 10 and 2 μm) with a larger pinched segment (60 μm), and at different buffer/particle solution flow rate ratios (5 – 25). The separation distances between particles are larger (as large as 2 times) than those achieved with conventional PFF. In addition, the separation position and distance can be adjusted by changing the driving voltage. The robust performance is due to the unique features of the flow field inside the pinched segment. We investigated several factors, including flow rate ratio, total flow rate and driving voltage, that affect the separation performance.

1. INTRODUCTION

For many lab-on-a-chip and micro Total Analysis Systems (μTAS) platforms, in particular those designed for biology, biomedical and medicine applications, separation of micron-sized particles is a crucial prerequisite step for the downstream processing steps [1, 2, 3, 4, 5]. The separation step provides the necessary purification, isolation and enrichment in order to allow the subsequent detection, quantification, characterization and diagnosis of the target objects, e.g. specific biological cells [6, 7, 8, 9]. Since most of the biological cells/particles of interest exist in fluid medium, separation in microfluidic environment has gathered great interest. Recent progress in microfluidics has provided a variety of novel techniques for micro-particle separation [10, 11, 12].

Size is one of the important attributes of particles or bio-particles, and size based separation has been a focus in the field of microfluidics. Generally, the separation strategies based on microfluidic technology can be classified into two categories: active and passive methods [13]. In the former, external force fields, for example electric [14, 15, 16], optical [17, 18], and magnetic forces [19, 20] are utilized to cause different movements among micron-sized objects that have different physical properties including size, conductivity, and magnetic susceptibility. For the passive techniques, the separation relies on the proper design of hydrodynamic flows, fluidic networks, placement of obstacles and filters. Some examples of passive techniques include pinched flow fractionation, deterministic lateral displacement [21], hydrodynamic filtering [22], and inertial separation [23, 24].

Devices based on passive methods are generally easier to operate [10, 22]. Among the various passive techniques, pinched flow fractionation (PFF) is considered one of the most convenient one owing to its simple working principle [25]. In PFF, two liquid streams – one containing particle mixture and one being buffer fluid – are introduced from two inlets and meet in a narrow channel, known as the pinched segment. By adjusting the flow ratio between the two liquids, the width of the liquid stream is adjusted so that the particles are

pushed against the channel wall in the pinched segment. Upon exiting from the pinched segment, particles of different sizes follow different streamlines to a broadened region, and the separation distance between the particles is amplified due to the channel expansion.

In spite of its simplicity in concept, conventional PFF device has certain limitations including the requirement of a narrow pinched segment and limited separation distance. A number of modifications have since been proposed by various researchers to improve the performance of PFF devices [26, 27, 28, 29, 30]. For example, the hydrodynamic resistance were adjusted by placing asymmetric branches after the pinched segment to cause a preferential flow into certain outlet [26]. Vig and Kristensen integrated a snakelike structure in the broadening segment to further amplify the separation distance between particles [27]. In other studies, channel with extreme aspect ratios [29] or pinched segment with tilted sidewalls [30] were utilized to increase the separation inside the pinched segment. Combining active methods into conventional PFF can improve the performance as well. For example, Lee *et al.* employed an optical scattering force from a continuous laser to enhance the separation distance, because optical force is different for particles of different size [28].

Acoustically driven microbubbles are an excellent agent to induce microscale hydrodynamic flows. Microbubble streaming flows have demonstrated a wide range of applications, including fluid pumping [31], mixing [32], particle focusing [33, 34], particle sorting [35] and biological cell trapping [36]. In previous work, the sorting of microparticles relies on a trap-and-release mechanism [35]. The superposition of bubble streaming and Poiseuille flows forms a closed upstream vortex. Large particles are trapped into the vortex, and released afterwards from the cluster. Due to the narrow focused particle trajectories, particles of different sizes are separated to different outlets [35]. This trap-and-release mechanism has also been utilized to focus microparticles [33]. In addition to steady streaming flow, the secondary Bjerknes force may also play an important role when the fluid and particle have different densities. The interplay between the drag force due to streaming flow and Bjerknes force allows attraction or repulsion between the particle and the bubble. This

subtle and interesting mechanism has been exploited for versatile particle manipulation, including selective trapping and sorting of microparticle based on particle size and density [37].

In this paper, we propose and demonstrate a novel and simple technique to enhance the particle separation performance of conventional PFF devices. Our device integrates a microbubble element into the pinched segment to locally alter the flow behaviors. When actuated remotely by the pressure field induced by a piezoelectric transducer, the microbubble generates steady streaming flow, and thus modifies the flow characteristic inside the pinched segment. Different from previous works that utilized trap-and-release mechanism [33, 35], the current technique does not require a upstream vortex to trap particles. Instead, the bubble streaming flow accelerates the flow near the bubble. This local velocity acceleration enhances the separation among particles of different sizes. Moreover, the operation of the microbubble and particle separation can be easily tuned by controlling the driving amplitude. In the following sections, we first describe the experimental details, and then explain the working principle of our proposed technique. We study the effect of flow rate ratio, total flow rate and driving voltage on the separation performance.

2. EXPERIMENT

2.1. Microfluidic Devices. Fig. 1 shows a schematic illustration of the microdevice for particle separation. A side channel was fabricated within the pinched segment region on the side wall to form a microbubble. Microdevices were fabricated in (Polydimethylsiloxane) PDMS using soft lithography technique [38]. Master molds were manufactured by lithographic patterning a dry film (MM540, DuPont) of a thickness of 35 μm. Briefly, a layer of dry film resist was first laminated onto a copper plate using a thermal laminator. After ultra-violet (UV) exposure through a transparency photo mask (10,000 dpi, CAD/Art Services Inc), the exposed dry film was developed, rinsed and dried to obtain the master mold. PDMS base and initiator were throughly mixed, degassed, and then cast on the

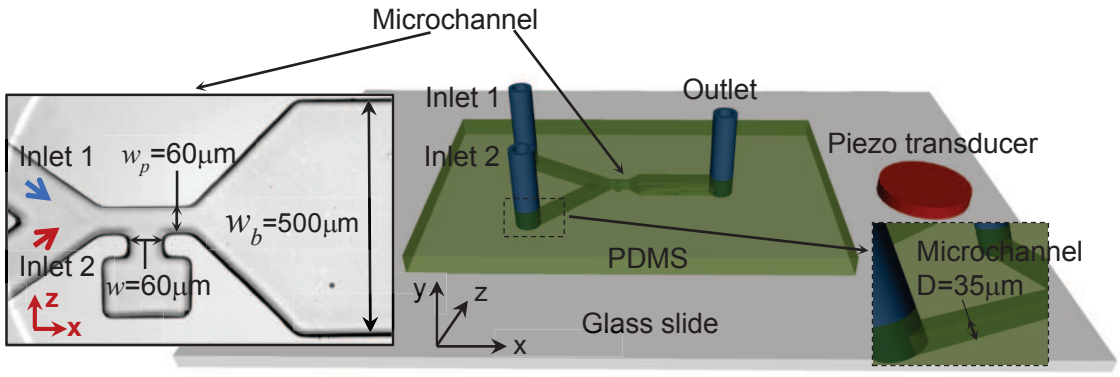

Figure 1. Schematic of the microdevice for particle separation. w_p is the width of pinched flow segment; w_b is the width of broadened segment; w is the width of bubble generation segment; D is the depth of microchannel.

master. After curing, the PDMS replica was peeled off from the master, cut and punched, and then bonded with a flat glass slide after corona surface treatment. Using this method, microchannels with a rectangular cross sectional shape were fabricated. A piezoelectric transducer (part number: SMD15T09S411, thickness 0.9 mm, diameter 15 mm, Steiner & Martins, Inc) was glued to the glass slide to control the amplitude of the bubble vibration.

2.2. Materials. A binary mixture of polystyrene particles, (diameters $d_s = 2\,\mu$m and $d_l = 10\,\mu$m, Magsphere Inc) were used as model particles. These particles were suspended in 22% (w/w) aqueous glycerol solution whose density was almost the same with the particle samples. The matched density of the solutions reduced the effect of particle sedimentation. The original solutions of 2 μm and 10 μm particles (2.5% w/w) were diluted with 22% glycerol solution to 2000 and 200 times respectively. The final particle concentrations were 2.84×10^6 mL^{-1} and 2.27×10^5 mL^{-1} respectively. For experiments with both conventional and bubble enhanced PFF microdevices, 22% glycerol solution was injected to inlet 1 as buffer solution, and 22% glycerol solution with 2 μm and 10 μm particles was injected into inlet 2 as particle solution. Surfactant Tween 20 was added to all solutions at a concentration of 0.5% w/w to prevent particle adhesion to channel walls and particle agglomeration.

2.3. Experimental Set-up. The microfluidic device was placed on an inverted microscope stage (IX73, Olympus). Microfluidic devices were illuminated by a fiber optic light for transmission bright-field imaging. The flow rates to the inlets were controlled separately by two syringe pumps (NE-300, New Era and KDS 200, KDS Scientific). To maintain good stability of the flow, small syringes (1 ml) were used to minimize the effect of the motor's step motion. At a flow rate of 0.2 μL/min, the velocity obtained by tracking individual particles showed that the coefficient of variation of the velocity was about 5% or smaller. Sinusoidal signals of different frequency and amplitude were generated by a function generator (DG4062, Rigol) and were amplified 10 times by an amplifier (7500, Krohn-Hite) to drive the piezoelectric transducer. The driving voltages to the transducer were measured in terms of peak-to-peak values. In the following sections, the voltage refers to the output voltage from the amplifier, which was directly connected to the electrodes of the transducer. To record particle trajectories, a high-speed camera (Phantom Miro M310, Vision Research) was used to capture videos.

2.4. Data Analysis. ImageJ was used to extract particle trajectory information [39]. The data of the particle size and position were analyzed and post-processed with Matlab. Separation resolution was calculated from the standard deviation and peak separation distance to provide a quantitative analysis and consistent criteria for comparison among different experiment conditions. As will be seen in the results and discussion later, the number of smaller particle was always large enough (more than 20). The relatively fewer number (at least 4 or 5) of large particles was due to the sedimentation. This is because perfect density matching of the particle and solution was difficult. We have conducted additional experiment to evaluate the effect of number of large particles on their position distribution. The results showed that the analysis based on 4 or 5 large particles is accurate enough to determine both the peak position and standard deviation.

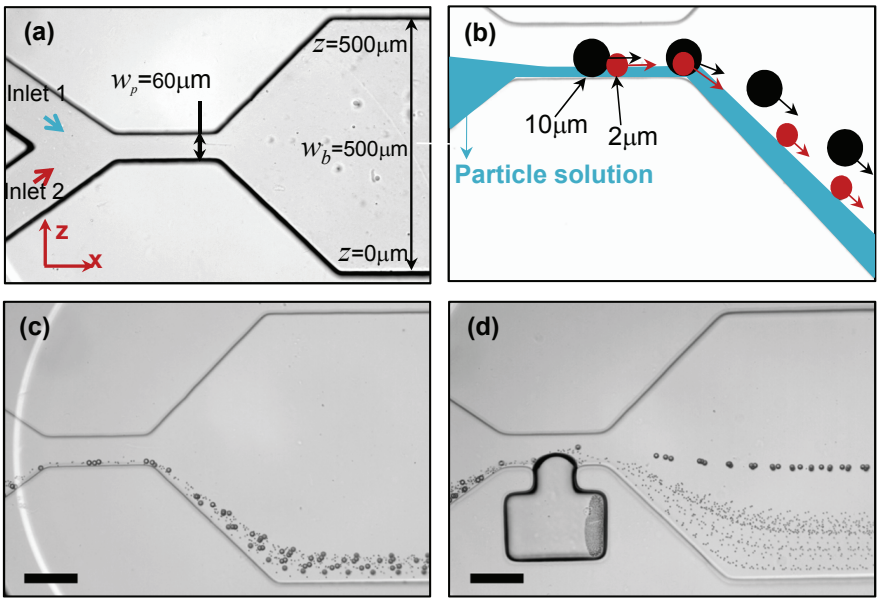

Figure 2. Pinched flow fractionation devices. (a) a conventional PFF; (b) schematic illustration of the working principle of conventional PFF. The comparison of particle trajectories in a conventional PFF (c) and a bubble enhanced PFF device. (d) The flow rates are $Q_1 = 3.0\ \mu$L/min and $Q_2 = 0.2\ \mu$L/min. Scale bars are 100 μm.

3. WORKING PRINCIPLE

In a conventional PFF microdevice, as shown in Fig. 2(a)(b), the solution containing particles need to be aligned onto the sidewall in the pinched segment for the separation mechanism to work. Let Q_1, and Q_2 be the flow rates of the buffer and particle solutions respectively, w_p and w_b be the widths of the pinched and broadened segment respectively, and assume a linear uniform velocity profile within the pinched segment [25], the widths of the buffer and particle solutions inside the pinched segment can be approximated as $w_1 = \dfrac{Q_1}{Q_1+Q_2}w_p$, $w_2 = \dfrac{Q_2}{Q_1+Q_2}w_p$ respectively. If a binary mixture of particles (with diameter d_l and d_s) is considered, the first critical condition to align the larger particles is $w_2 = \dfrac{Q_2}{Q_1+Q_2}w_p \le d_l$, which leads to

$$\frac{Q_1}{Q_2} \ge \frac{w_p - d_l}{d_l}. \tag{1}$$

Similarly, the alignment of smaller particles requires

$$\frac{Q_1}{Q_2} \geq \frac{w_p - d_s}{d_s}. \tag{2}$$

Meeting the second critical flow rate ratio, the separation distance within the pinched segment between the two particles is $(d_l - d_s)/2$, which will not increase further. After exiting into the broadened segment, the initial position difference within the pinched region is linearly amplified to a larger separation distance, $\frac{(d_l - d_s)}{2}\frac{w_b}{w_p}$, which is theoretically the best separation distance that can be achieved [25].

From the working principle of conventional PFF, we can see that the pinched segment should have similar size as (often only two or three times of) the particles to be separated [25, 40, 41]. Otherwise, a large flow ratio is required. This requirement however poses several challenges: (1) microfabrication capability and (2) potential clogging issues due to the small pinched segment. In addition, the maximal separation distance is fixed and limited. Considering a typical broadened/pinched segment ratio $\frac{w_b}{w_p} = 10$, and a binary particle mixture of $d_l = 10\,\mu$m and $d_s = 2\,\mu$m, the best separation distance is about $40\,\mu$m, which is only a small fraction (less than 10%) of the broadened channel. Thus, downstream collection of the particles can be challenging. In actual applications, the particles exhibit dispersion due to channel surface roughness [42]. Consequently, the actual separation distances are even smaller than the theoretical prediction.

Our acoustic bubble enhanced method can address those limitations of the conventional PFF. When actuated by acoustic pressure, i.e. induced by a piezoelectric transducer, the vibrating microbubble sets up steady streaming flows. Although steady streaming flow velocity decays fast [43], the local strong flow can effectively improve the particle separation distance. The comparison between a conventional PFF and a bubble enhanced PFF is shown in Fig. 2(c)(d), under the same flow rate ratio $Q_1/Q_2 = 15$. As can be seen, 2 μm and 10 μm particles were not separated with the conventional PFF channel. This is anticipated:

because $Q_1/Q_2 = 15$ does not meet the required flow ratio, 29, based on the separation criterion set in equation 2. On the other hand, with the bubble enhanced PFF microdevice, the particles were clearly separated with a distance about 80 μm in Fig. 2(d), which is 2 times of the best theoretical seperation distance (40 μm) with the conventional PFF. The comparison confirmed the critical role of acoustic bubble streaming flows in improving the separation performance.

It is the velocity field that improves the separation. Previous studies have shown that the streaming flows are frequency dependent: in the low frequency regime, the flows are predominantly “fountain" type flows, while in the high frequency regime, the flows are “anti-fountain" type [44]. For a 60 μm diameter microbubble, 41.7 kHz is in the low driving frequency regime [45]. The superposition of the flow field in the microchannel with non-vibrating bubble, and acoustic streaming flow field are schematically shown in Fig. 3(a). The combination of the “fountain" type flow and the pressure driven flow resulted in a unique flow structure to affect the particle trajectories and enhance the separation between particles of different sizes.

We measured the velocity field with particle image velocimetry (PIV) technique to quantitatively understand the characteristics of velocity field inside the pinched segment. Fig. 3(b) shows the velocity vector distribution in the bubble enhanced PFF when the bubble was excited at 41.7 kHz and 150 V; and Fig. 3(c) shows the velocity distribution in the conventional PFF channel. Flow rates from inlet 1 and 2 were 3.0 μL/min and 0.2 μL/min respectively. The velocity distribution of the conventional PFF has a parabolic profile and is symmetrical about the centerline. In contrast, the acoustic bubble enhanced PFF shows a very different velocity profile: the lower half has a larger velocity. In fact, the velocity increases even more when it is closer to the bubble. However, because of the bubble interface oscillation, the PIV measurement was not able to measure the velocity near the bubble interface with sufficient accuracy.

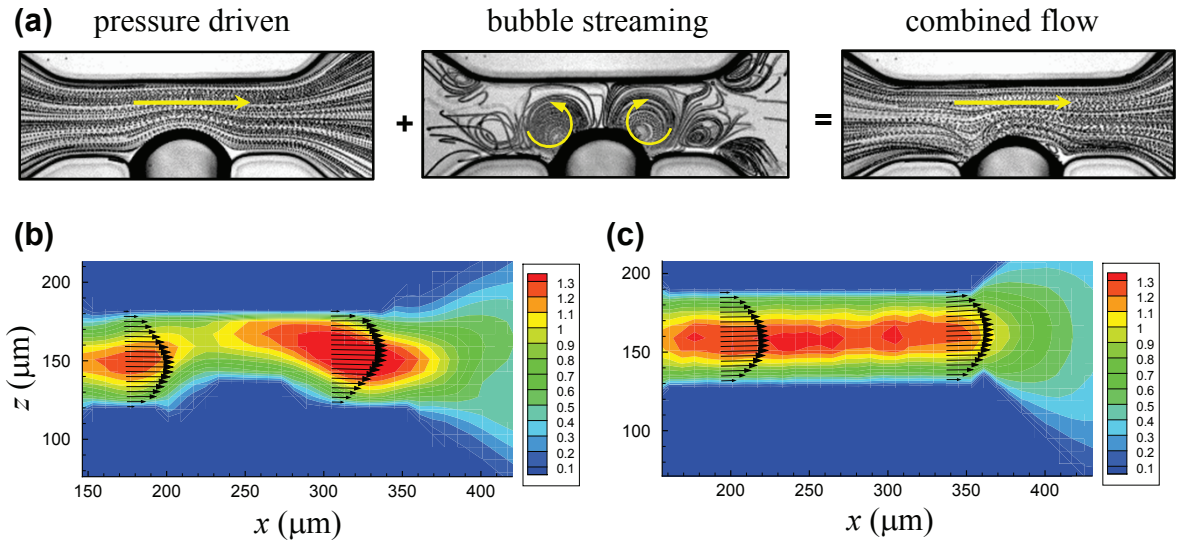

Figure 3. (a) the combined flow field of pressure driven flow and acoustic microbubble streaming flow; (b) the velocity profile inside the pinched segment of the bubble enhanced microdevice with frequency 41.7 kHz and voltage 150 V; (c) the velocity profile inside the pinched segment of the conventional PFF microdevice. Flow rate from inlet 1 and 2 are 3.0 μL/min and 0.2 μL/min respectively. The contour represents the velocity magnitude normalized by the average velocity entering the pinched segment. The experimental results in (b) and (c) were basd on micro particle image velocimetry (μPIV) measurement.

The change of velocity is due to the microbubble streaming flows. As the flow approaches from the upstream towards the microbubble inside the pinched channel, the “fountain" type acoustic flow caused by vibrating bubble increases the velocity magnitude. Therefore, the average velocity near lower wall surface is larger than that of upper wall surface. Because of the fixed volume flow rate, the width of particle solution reduces. The large particles are aligned onto the bubble surface and pushed onto a streamline that is *further* away from its original streamline because of the combined flow field. The small difference inside the pinched segment is significantly enlarged in the broadened segment, so that the acoustic bubble flow field improves the separation performance. Moreover, by adjusting the driving voltage, the relative strength of the bubble streaming can be tuned easily to control both the separation distance and positions of the particles.

It is worth to note the importance of driving frequency and how it was selected. Prior works [44, 45] have found that the vibration mode of the bubble depends on the dimension of the bubble and driving frequency. The vibration mode in turn affects the steady streaming flow orientation. In the technique reported here, a strong “fountain" type streaming flow is necessary because it will accelerate the flow near the bubble surface to facilitate particle separation. In practice, the frequency can be experimentally tuned by observing the flow or estimated by theoretical analysis [44, 45]. For a 60 μm diameter bubble, 41.7 kHz lies in the upper limit of the frequency range to establish a “fountain" flow while providing a stronger streaming flow.

4. RESULTS AND DISCUSSION

The introduction of a vibrating bubble to the conventional PFF has a positive influence on particle separation due to the unique feature of the combined flow field as discussed in section 3. Several factors can affect the separation performance of the acoustic bubble enhanced PFF. First, the ratio of flow rates of the two inlets is a key factor, since this ratio determines the width of the particle-containing solution in the pinched segment, and relates to the degree of alignment of particles to the sidewall. Second, the total flow rate affects the separation performance, because it is related to the relative strength between the streaming flow and pressure driven flow. Third, the driving voltage affects directly the amplitude of the bubble vibration, and thus the intensity of the acoustic streaming flow. We conducted systematic experimental work to examine the influence of these factors on the separation performance.

4.1. Effect of Flow Rate Ratio. We first examined the influence of flow rate ratio of inlet 1 to inlet 2, Q_1/Q_2, which relates to the focusing of the solution and the aligning of particles on the sidewall. To maintain the same acoustic streaming flow strength, the

vibrating frequency of bubble was kept at 41.7 kHz and the driving voltage was 150 V. The flow rate ratio Q_1/Q_2 was set at 5, 15 and 25 respectively, while the total flow rate was kept constant at 5.2 μL/min.

Fig. 4 shows the particle separation when the flow rate ratio of the buffer solution to the particle solution were varied. As the flow rate ratio increased from 5 to 25, the peak position and distribution width of 10 μm particles were almost constant while the peak position of 2 μm moved towards the side wall and the distribution width became smaller. The trend means that the separation performance gets better when the flow rate ratio increases from 5 to 25. This can be explained as follows: 10 μm particles always align along the wall in the pinched segment according to equation 1, for the range of flow ratio from 5 to 25. Because the total flow rate is fixed, the positions and distribution width of 10 μm particles in the broadened segment remain almost the same.

Varying flow rate ratio mainly affects the position and distribution of smaller particles. As the flow rate ratio increases from 5 to 25, the width of particle solution decreases and the smaller particles are able to get closer to the wall in the pinched segment. Therefore, a larger fraction of 2 μm particles are aligned in the pinched segment. The increasing alignment leads to both a narrower spatial distribution of 2 μm particles and positions closer to the wall in the broadened segment. However, not all of the 2 μm particles were aligned along the wall in the pinched segment even when the flow rate ratio was 25, according to equation 2. Therefore, the slight spread of 2 μm particle in pinched segment affects their final positions in the broadened segment. The smaller particles show a wider spatial distribution than 10 μm particles. In addition, the roughness of the channel wall also contributes to relatively large dispersion of smaller particles [42].

As noted by other researchers, the separation distance between the peak positions alone is not sufficient to characterize the separation performance [42]. To better quantify the separation performance, the parameter separation resolution was determined following

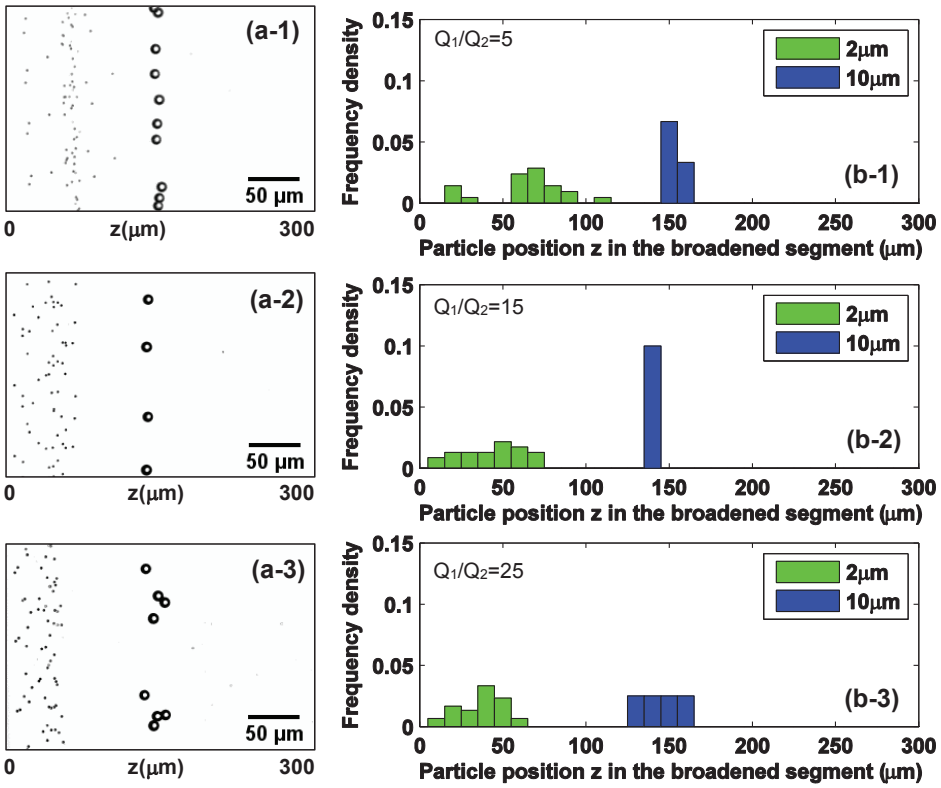

Figure 4. Effect of flow rate ratio on particle separation. (a-1) to (a-3) are the superimposed images showing the particle trajectories. (b-1) to (b-3) are the histograms showing the particle position. The flow rate ratios are $Q_1/Q_2 = 5$ in (a-1) and (b-1), $Q_1/Q_2 = 15$ in (a-2) and (b-2), and $Q_1/Q_2 = 25$ in (a-3) and (b-3). The other experiment conditions are the same for all three: $f = 41.7$ kHz and $V = 150$ V, total flow rate $Q_t = Q_1 + Q_2 = 5.2$ μL/min.

previous studies [42],

$$R_s = \frac{z_2 - z_1}{2(d_1 + d_2)}, \tag{3}$$

where z_1 and z_2 are the peak positions of 2 μm (smaller) and 10 μm (larger) particles respectively, and d_1 and d_2 are their respective standard deviations. When the flow rate ratio are 5, 15 and 25, the separation resolution are 1.66, 2.36 and 3.05 respectively. When the flow rate ratio was 25, the separation resolution had the largest value of 3.05, suggesting the best separation performance. w_2/d_s can be interpreted as a dimensionless number comparing the width of the pinched particle solution to the size of small particles. When

the flow rate ratio are 5, 15 and 25, w_2/d_s are 5, 1.88 and 1.15 respectively. The improved separation resolution with decreasing w_2/d_s supports our earlier discussion that a narrower particle solutions will lead to better separation.

4.2. Effect of Total Flow Rate. In this part, we studied how the total flow rate affects the separation performance. Two sets of experiments were conducted. In the first set, the ratio of the flow rate Q_1/Q_2 was kept constant at 15, and the total flow rate $Q_t = Q_1 + Q_2$ was controlled at 3.2 μL/min (Fig. 5 (a-1)) and 6.4 μL/min (Fig. 5 (a-2)) respectively. In the second set, the ratio of the flow rate Q_1/Q_2 was 25, and the total flow rate were controlled at 5.2 μL/min in Fig. 5 (b-1) and 10.4 μL/min in Fig. 5(b-2) respectively. In all these experiments, the piezoelectric transducer was actuated at frequency 41.7 kHz and driving voltage 150 V. By comparing (a-1) with (a-2), and (b-1) with (b-2), we observed that the particle positions in the broadened segment shifted towards the channel sidewall as the total flow rate increased. At the same time, the increased total flow rates caused decreased peak separation distances.

When the flow rate ratio was 15, the separation resolution for 3.2 μL/min was 2.87 and for 6.4 μL/min was 2.02, meaning that the separation performance of 3.2 μL/min is better than 6.4 μL/min. The same trend was also observed for the experiments with flow rate ratio $Q_1/Q_2 = 25$. In this case, the separation resolution for 5.2 μL/min is 2.62 and for 10.4 μL/min is 1.72, which means that the separation performance of 5.2 μL/min is better than 10.4 μL/min. Therefore, the increasing total flow rates led to worse separation performance.

The results suggest that at a fixed flow rate ratio, the bubble enhanced PFF is more effective when the total flow rate is smaller. The reason can be explained as follows: when the total flow rate is smaller, the microbubble streaming flow is stronger relative to the pressure driven flow. The combined flow field accelerates the flows more effectively. As we have discussed earlier, the velocity profile caused by the acceleration is critical in pushing particles to a streamline further into the buffer solution. As the total flow rate increases,

the relative strength of the bubble streaming becomes smaller. In an extreme case, when pressure driven flow velocity is so much larger than the streaming flow, the effect of the bubble streaming flow will be negligible.

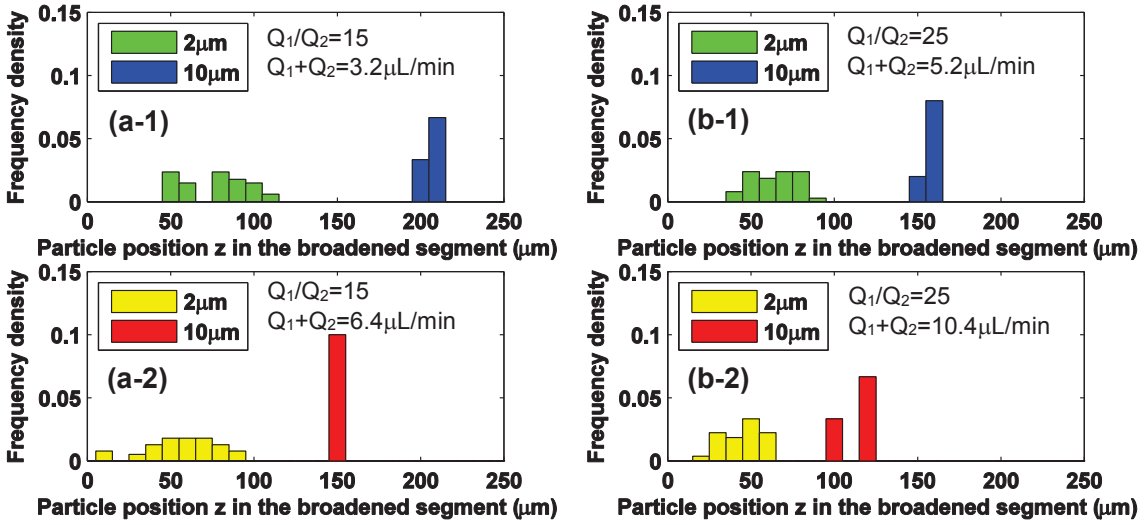

Figure 5. Effect of total flow rate on particle separation. (a-1) and (a-2) are the histograms of particle separation with total flow rate of 3.2 μL/min and 6.4 μL/min respectively. The flow rate ratio of (a-1) and (a-2) was kept constant at 15. (b-1) and (b-2) are the histograms showing the particle position with total flow rate of 5.2 μL/min and 10.4 μL/min respectively. The flow rate ratio of (b-1) and (b-2) was kept constant at 25.

4.3. Effect of Voltage. In the last part, the effect of the working voltage on the separation performance was discussed. The driving voltage was set at 0 V, 100 V, 150 V and 200 V, while the ratio of the flow rate was $Q_1/Q_2 = 30$ and the driving frequency was 41.7 kHz. The particle position distribution results are shown in Fig. 6. It was observed that peak separation distance of 2 μm and 10 μm particles increased and particles moved further from the wall as the working voltage increased from 0 V to 200 V. The increasing working voltage leads to the increased acoustic streaming flow velocity because streaming velocity $u_s \propto V^2$ [35, 43], thus imposing a relatively stronger influence on the imposed pressure driven flow. The effect is similar to the case where the total flow rate is reduced.

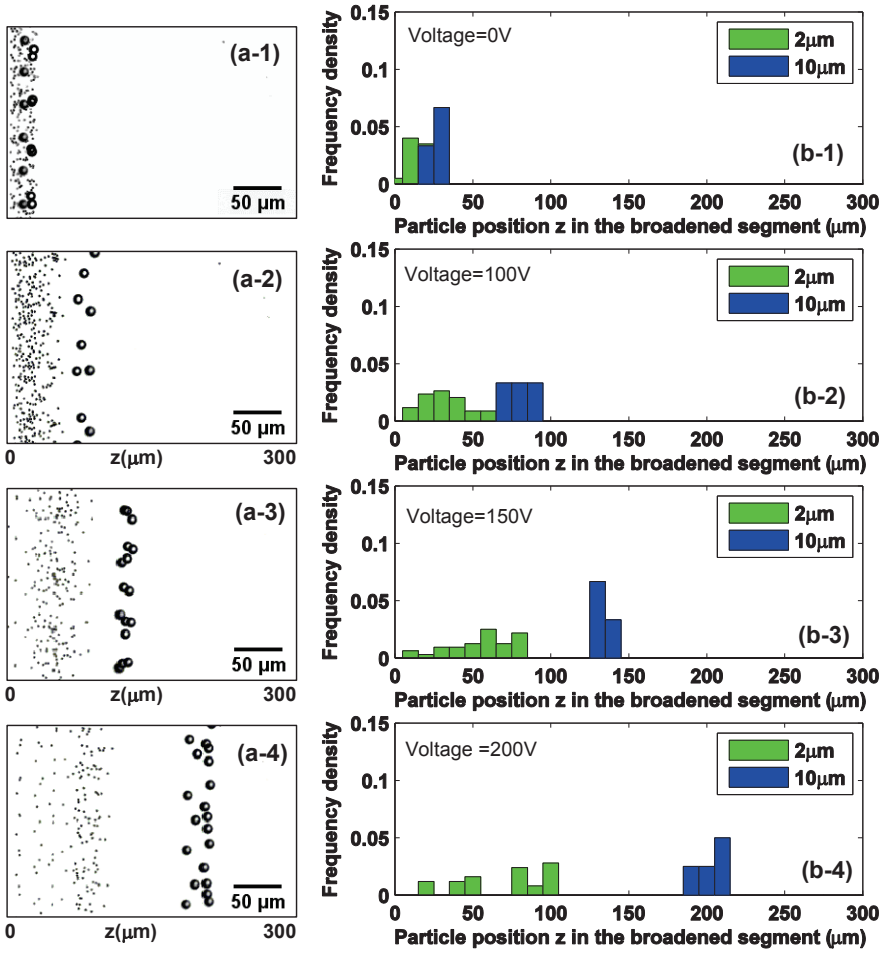

Figure 6. Effect of driving voltage on particle separation. (a-1) to (a-4) are the superimposed images showing the particle trajectories. (b-1) to (b-4) are the histograms showing the particle position. The driving voltage of was set at 0 V in (a-1) and (b-1), 100 V in (a-2) and (b-2), 150 V in (a-3) and (b-3), and 200 V in (a-4) and (b-4). The ratio of the flow rate from inlets 1 and 2 was 30, and the driving frequency was 41.7 kHz.

The separation resolution for 0 V was 0.28, the separation resolution for 100 V was 1.18, the separation resolution for 150 V was 1.62 and the separation resolution for 200 V was 1.77. It is clear that the 200 V driving voltage has the largest separation resolution, meaning the best separation performance. It is worth noting that by tuning the driving voltage, both the positions of the large and small particles can be tuned. For example, the

peak position of 10 μm particles were shifted from $z = 75\,\mu$m to $z = 200\,\mu$m when the driving voltage was varied from 100 V to 200 V. The tunable positioning is an useful feature for applications where particles need to be switched to different outlets.

4.4. Benefits and Limitations. There are a variety of particle separation techniques available for microfluidic applications, and each of them has its own merits and shortcomings [13]. The technique reported in this work can be considered a combination of (conventional) PFF and external acoustic actuation. Due to the tunable feature of the bubble streaming flows, our technique is able to operate in two modes. When the bubble is not actuated (bubble-off mode), it works like a conventional PFF device and the general working principle of PFF applies. When the bubble is actuated (bubble-on mode), the streaming flows can enhance the particle separation, even inside a relatively large pinched channel. The enhancement thus relaxes the restraint on the microfabrication process. For our technique to work effectively, the streaming flow has be to strong enough compared to the pressure driven flow. This is one factor that may pose a limit on the throughput. In conventional PFF, the particle separation only depends on the flow rate ratio, therefore the throughput of PFF can be higher, as long as the microfluidic device can withstand the imposed pressure. However, when the bubble streaming flow is weaker, our technique will work similarly to a conventional PFF. In this regard, the beneficial features of our technique may be absent, but the device will retain the characteristics of a conventional PFF.

Acoustophoresis is another effective method to sort particles utilizing acoustic radiation forces [46]. Throughput of acoustophoretic separation can be higher when the particles have very different sizes and densities [46, 47]. However, acoustophoretic actuation requires pressure wavelengths comparable to the size of particles and/or the channel dimensions. For typical microfluidic dimensions, the acoustic frequency is in the range of 1 MHz to 100 MHz, which may require external cooling to minimize the possible heating when dealing with biological samples [48]. Additionally, silicon or glass microfluidic devices are necessary to set up the standing waves inside the channels [48]. In our technique, the man-

ufacture is simpler, as a piezoelectric transducer can be simply glued to the bottom of the glass substrate. Because of the lower frequency (less than 100 kHz) used, heat generation is thus small and negligible. Based on the above discussion, our proposed technique offers several attractive features – tunability, enhanced separation, low heat generation and simple implementation, while the low throughput can be considered a limitation.

5. CONCLUSIONS

We proposed and demonstrated a novel acoustic bubble enhanced flow fractionation technique to overcome the limitations of conventional PFF devices. The combination of acoustic streaming flow from the bubble and the pressure driven flow inside the pinched segment provides beneficial features – local acceleration and non-uniform velocity profile. The combined flow field results in improved and robust separation between microparticles. Systematic experiments were conducted to study the effect of flow rate ratio, total flow rate and driving voltage on the separation performance. We found: first, a large flow rate ratio of the buffer to particle-containing solution improves the separation performance, because of the better alignment of particles to the sidewall. Second, decreasing total flow rate leads to better separation performance due to the stronger effect of microbubble streaming flows. Third, as the driving voltage increases, the separation resolution between particles increases, attributed to a larger peak separation distance caused by the increased bubble acoustic streaming flow. The method demonstrated in this work not only addresses some of the limitations of conventional PFF, but also benefits applications where flexible tuning of particle positions or separation is required due to the ease of changing driving voltage.

REFERENCES

[1] David N Breslauer, Philip J Lee, and Luke P Lee. Microfluidics-based systems biology. *Mol. Biosyst.*, 2:97–112, 2006.

[2] Douglas B. Weibel and George M. Whitesides. Applications of microfluidics in chemical biology. *Curr. Opin. Chem. Biol.*, 10:584–591, 2006.

[3] Ali Asgar S Bhagat, Hansen Bow, Han Wei Hou, Swee Jin Tan, Jongyoon Han, and Chwee Teck Lim. Microfluidics for cell separation. *Med. Biol. Eng. Comput.*, 48:999–1014, 2010.

[4] Ashleigh B. Theberge, Fabienne Courtois, Yolanda Schaerli, Martin Fischlechner, Chris Abell, Florian Hollfelder, and Wilhelm T S Huck. Microdroplets in microfluidics: An evolving platform for discoveries in chemistry and biology. *Angewandte Chemie - International Edition*, 49:5846–5868, 2010.

[5] Eric K Sackmann, Anna L Fulton, and David J Beebe. The present and future role of microfluidics in biomedical research. *Nature*, 507:181–9, 2014.

[6] André A. Adams, Paul I. Okagbare, Juan Feng, Matuesz L. Hupert, Don Patterson, Jost Götten, Robin L. McCarley, Dimitris Nikitopoulos, Michael C. Murphy, and Steven A. Soper. Highly efficient circulating tumor cell isolation from whole blood and label-free enumeration using polymer-based microfluidics with an integrated conductivity sensor. *J. Am. Chem. Soc.*, 130:8633–8641, 2008.

[7] Masaya Murata, Yukihiro Okamoto, Yeon Su Park, Noritada Kaji, Manabu Tokeshi, and Yoshinobu Baba. Cell separation by the combination of microfluidics and optical trapping force on a microchip. *Anal. Bioanal. Chem.*, 394:277–283, 2009.

[8] Soojung Claire Hur, Nicole K Henderson-MacLennan, Edward R B McCabe, and Dino Di Carlo. Deformability-based cell classification and enrichment using inertial microfluidics. *Lab. Chip*, 11:912–920, 2011.

[9] Yuchao Chen, Peng Li, Po-Hsun Huang, Yuliang Xie, John D Mai, Lin Wang, Nam-Trung Nguyen, and Tony Jun Huang. Rare cell isolation and analysis in microfluidics. *Lab. Chip*, 14:626–45, 2014.

[10] P. Sajeesh and Ashis Kumar Sen. Particle separation and sorting in microfluidic devices: A review. *Microfluid. Nanofluid.*, 17:1–52, 2014.

[11] Daniel R. Gossett, Westbrook M. Weaver, Albert J. MacH, Soojung Claire Hur, Henry Tat Kwong Tse, Wonhee Lee, Hamed Amini, and Dino Di Carlo. Label-free cell separation and sorting in microfluidic systems. *Anal. Bioanal. Chem.*, 397:3249–3267, 2010.

[12] Hideaki Tsutsui and Chih Ming Ho. Cell separation by non-inertial force fields in microfluidic systems. *Mech. Res. Commun.*, 36:92–103, 2009.

[13] Nicole Pamme. Continuous flow separations in microfluidic devices. *Lab. Chip*, 7:1644–1659, 2007.

[14] Peter R C Gascoyne and Jody Vykoukal. Particle separation by dielectrophoresis. *Electrophoresis*, 23:1973–1983, 2002.

[15] Benjamin G. Hawkins, A. Ezekiel Smith, Yusef A. Syed, and Brian J. Kirby. Continuous-flow particle separation by 3D insulative dielectrophoresis using coherently shaped, dc-biased, ac electric fields. *Anal. Chem.*, 79:7291–7300, 2007.

[16] Zhigang Wu, Ai Qun Liu, and Klas Hjort. Microfluidic continuous particle/cell separation via electroosmotic-flow-tuned hydrodynamic spreading. *J. Micromech. Microeng.*, 17:1992–1999, 2007.

[17] David G Grier. A revolution in optical manipulation. *Nature*, 424:810–816, 2003.

[18] E Eriksson, J Scrimgeour, A Granéli, K Ramser, R Wellander, J Enger, D Hanstorp, and M Goksör. Optical manipulation and microfluidics for studies of single cell dynamics. *Journal of Optics A: Pure and Applied Optics*, 9:S113–S121, 2007.

[19] Nicole Pamme. Magnetism and microfluidics. *Lab. Chip*, 6:24–38, 2006.

[20] Jian Zeng, Yanxiang Deng, Pallavi Vedantam, Tzuen Rong Tzeng, and Xiangchun Xuan. Magnetic separation of particles and cells in ferrofluid flow through a straight microchannel using two offset magnets. *J. Magn. Magn. Mater.*, 346:118–123, 2013.

[21] Lotien Richard Huang, Edward C Cox, Robert H Austin, and James C Sturm. Continuous particle separation through deterministic lateral displacement. *Science (New York, N.Y.)*, 304:987–990, 2004.

[22] A. Karimi, S. Yazdi, and A. M. Ardekani. Hydrodynamic mechanisms of cell and particle trapping in microfluidics. *Biomicrofluidics*, 7, 2013.

[23] Dino Di Carlo. Inertial microfluidics. *Lab. Chip*, 9:3038–3046, 2009.

[24] A. A S Bhagat, Sathyakumar S. Kuntaegowdanahalli, and Ian Papautsky. Inertial microfluidics for continuous particle filtration and extraction. *Microfluid. Nanofluid.*, 7:217–226, 2009.

[25] Masumi Yamada, Megumi Nakashima, and Minoru Seki. Pinched flow fractionation: Continuous size separation of particles utilizing a laminar flow profile in a pinched microchannel. *Anal. Chem.*, 76:5465–5471, 2004.

[26] Junya Takagi, Masumi Yamada, Masahiro Yasuda, and Minoru Seki. Continuous particle separation in a microchannel having asymmetrically arranged multiple branches. *Lab. Chip*, 5:778–784, 2005.

[27] Asger Laurberg Vig and Anders Kristensen. Separation enhancement in pinched flow fractionation. *Appl. Phys. Lett.*, 93, 2008.

[28] Kyung Heon Lee, Sang Bok Kim, Kang Soo Lee, and Hyung Jin Sung. Enhancement by optical force of separation in pinched flow fractionation. *Lab. Chip*, 11:354–357, 2011.

[29] Ali Asgar S Bhagat, Han Wei Hou, Leon D Li, Chwee Teck Lim, and Jongyoon Han. Pinched flow coupled shear-modulated inertial microfluidics for high-throughput rare blood cell separation. *Lab. Chip*, 11:1870–1878, 2011.

[30] Hyun Woo Nho and Tae Hyun Yoon. Enhanced separation of colloidal particles in an AsPFF device with a tilted sidewall and vertical focusing channels (t-AsPFF-v). *Lab. Chip*, 13:773–6, 2013.

[31] Maulik V. Patel, Imaly A. Nanayakkara, Melinda G. Simon, and Abraham P. Lee. Cavity-induced microstreaming for simultaneous on-chip pumping and size-based separation of cells and particles. *Lab Chip*, 14:3860–3872, 2014.

[32] Daniel Ahmed, Xiaole Mao, Jinjie Shi, Bala Krishna Juluri, and Tony Jun Huang. A millisecond micromixer via single-bubble-based acoustic streaming. *Lab. Chip*, 9:2738–2741, 2009.

[33] Cheng Wang, Shreyas V. Jalikop, and Sascha Hilgenfeldt. Efficient manipulation of microparticles in bubble streaming flows. *Biomicrofluidics*, 6, 2012.

[34] Hoang V. Phan, Muhsincan Sesen, Tuncay Alan, and Adrian Neild. Single line particle focusing using a vibrating bubble. *Appl. Phys. Lett.*, 105(19):–, 2014.

[35] C. Wang, S.V. Jalikop, and S. Hilgenfeldt. Size-sensitive sorting of microparticles through control of flow geometry. *Appl. Phys. Lett.*, 99(3), 2011.

[36] Y. Xu, A. Hashmi, G. Yu, X. Lu, H. . Kwon, X. Chen, and J. Xu. Microbubble array for on-chip worm processing. *Appl. Phys. Lett.*, 102(2), 2013.

[37] Priscilla Rogers and Adrian Neild. Selective particle trapping using an oscillating microbubble, 2011.

[38] J.C. McDonald, D.C. Duffy, J.R. Anderson, D.T. Chiu, H. Wu, O.J.A. Schueller, and G.M. Whitesides. Fabrication of microfluidic systems in poly(dimethylsiloxane). *Electrophoresis*, 21(1):27–40, 2000.

[39] M.D. Abramoff, P.J. MagalhÃčes, and S.J. Ram. Image processing with imagej. *Biophotonics International*, 11(7):36–41, 2004.

[40] Takahiro Kawamata, Masumi Yamada, Masahiro Yasuda, and Minoru Seki. Continuous and precise particle separation by electroosmotic flow control in microfluidic devices. *Electrophoresis*, 29:1423–1430, 2008.

[41] Asger Vig Larsen, Lena Poulsen, Henrik Birgens, Martin Dufva, and Anders Kristensen. Pinched flow fractionation devices for detection of single nucleotide polymorphisms. *Lab. Chip*, 8:818–821, 2008.

[42] Abhishek Jain and Jonathan D. Posner. Particle dispersion and separation resolution of pinched flow fractionation. *Anal. Chem.*, 80:1641–1648, 2008.

[43] P. Marmottant and S. Hilgenfeldt. Controlled vesicle deformation and lysis by single oscillating bubbles. *Nature*, 423(6936):153–156, 2003.

[44] C. Wang, B. Rallabandi, and S. Hilgenfeldt. Frequency dependence and frequency control of microbubble streaming flows. *Phys. Fluids*, 25(2), 2013.

[45] B. Rallabandi, C. Wang, and S. Hilgenfeldt. Two-dimensional streaming flows driven by sessile semicylindrical microbubbles. *J. Fluid Mech.*, 739:57–71, 2014.

[46] Filip Petersson, Andreas Nilsson, Cecilia Holm, Henrik Jonsson, and Thomas Laurell. Continuous separation of lipid particles from erythrocytes by means of laminar flow and acoustic standing wave forces. *Lab Chip*, 5:20–22, 2005.

[47] Allen H J Yang and H Tom Soh. Acoustophoretic Sorting of Viable Mammalian Cells in a Micro fl uidic Device. *Anal. Chem.*, 84:10756–10762, 2012.

[48] Thomas Laurell, Filip Petersson, and Andreas Nilsson. Chip integrated strategies for acoustic separation and manipulation of cells and particles. *Chem. Soc. Rev.*, 36:492–506, 2007.

II. MICROFLUIDIC SEPARATION OF MAGNETIC PARTICLES WITH SOFT MAGNETIC MICROSTRUCTURES

Ran Zhou, Cheng Wang

Department of Mechanical & Aerospace Engineering

Missouri University of Science and Technology

Rolla, Missouri 65409

Tel: (573) 341-4636, Fax: (573) 341-4607

Email: wancheng@mst.edu

ABSTRACT

This paper demonstrates simple and cost-effective microfluidic devices for enhanced separation of magnetic particles by using soft magnetic microstructures. By injecting a mixture of iron powder and Polydimethylsiloxane (PDMS) into a prefabricated channel, an iron-PDMS microstructure was fabricated next to a microfluidic channel. Placed between two external permanent magnets, the magnetized iron-PDMS microstructure induces localized and strong forces on the magnetic particles in the direction perpendicular to the fluid flow. Due to the small distance between the microstructure and the fluid channel, the localized large magnetic field gradients results a vertical force on the magnetic particles, leading to enhanced separation of the particles. Numerical simulations were developed to compute the particle trajectories, and agreed well with experimental data. Systematic experiments and numerical simulation were conducted to study the effect of relevant factors on the transport of superparamagnetic particles, including the shape of iron-PDMS microstructure, mass ratio of iron-PDMS composite, width of the microfluidic channel, and total flow rate.

1. INTRODUCTION

Magnetism and magnetic particles or beads have long been used for bioseparation applications in biomedical sciences and clinical medicines [1, 2]. For example, immunomagnetic separation (IMS) is a standard laboratory technique for isolating cells, proteins, and nucleic acids. In this technique, magnetic particles conjugated with antibodies bind to antigens of the targeted cells' surface, and thus allow the cells to be isolated, purified and collected with a mangetic force field. Quadrupole magnetic flow sorter (QMS) has been used for isolation of cancer cells from patients with head and neck cancer [3, 4] and to separate islet cells for diabetes diagnosis research [5]. Lund-Olesen et al. studied the hybridization of target DNA in solution with probe DNA on magnetic beads immobilized on the channel sidewalls in a magnetic bead separator [6].

Over the last decade, magnetism has been integrated with microfluidics to harness the advantages of miniaturization, automation and integration, and the term "magnetofluidics" has been coined [7, 8, 9, 10, 11, 12]. Microfluidic-based magnetophoretic techniques have been demonstrated in continuous separation of erythrocytes and leukocytes from whole blood [13] and *E. coli* bacteria from living cells[14]. The use of magnetofluidics for bioseparation has received growing interest due to a number of unique advantages: low cost, insensitivity to temperature or pH, and remote actuation without direct contact. In some applications, magnetofluidics are favored over other methods, such as acoustic, electric, and optical forces, which often involve complex designs or strongly depend on the properties of the flow medium or the interaction between the fluid and fluidic channels [9, 10, 11].

The simplest and most prominent class of microsystems for magnetic particle separation relies on the combination of microstructures made of soft magnetic materials and an externally applied magnetic field. This combination offers a number of benefits. First, the magnetic strength can be easily adjusted or removed by controlling the strength of the external magnets. Second, due to their small size, the magnetized microstructures can provide strong magnetic field gradients and thus large forces, leading to efficient capture of magnetic

particles. This is similar to the traditional high gradient magnetic separators (HGMSs) [15] used for large scale magnetic separation, which comprise a separation column filled with a steel wool matrix in a large external magnetic field [16, 17].

Several methods have been reported in the literature on integrating microstructures with microfluidics to increase the local magnetic gradients [18, 19, 20, 21, 22, 23, 24]. Micrometer scale metal structures, such as pillars and strips, have been fabricated or patterned inside microfluidic channels [14, 19, 25]. Once magnetized by a magnetic field from external permanent magnets, these microstructures of soft materials generated strong magnetic field gradients and efficiently trapped or deflected superparamagnetic beads moving past them in a flowing stream of sample fluid. Lin et al. injected a continuous flow of nickel microparticle suspensions into an auxiliary channel next to the main fluidic channel [15]. The nickel microparticles were able to bend and concentrate the external magnetic field gradient. This magnetic field gradient induced magnetic forces on the particles in the main channel. Derec et al. built microfluidic channels on a copper PCB broad, and applied electric current through etched copper circuits to induce local magnetic field [26]. Faivre et al. studied the patterning of iron-PDMS composites inside microfluidic channels which could locally generate high gradients of magnetic field when exposed to external magnetic fields [27] .

In this paper, we present a simple and low-cost technique to fabricate microfluidic devices that integrate microstructures to increase the magnetic forces. The method is based on a microsolidics technique [28, 29]. The mangetic microstructures are made by injecting and curing a mixture of iron powder and PDMS in a structural microchannel next to the fluidic channel. We investigated various factors that influence the sorting performance, including the shape of iron-PDMS microstructure, mass ratio of iron powder, microfluidic channel width and total flow rate. We also developed a numerical method that can predict the particle separation and show good agreement with experimental measurements.

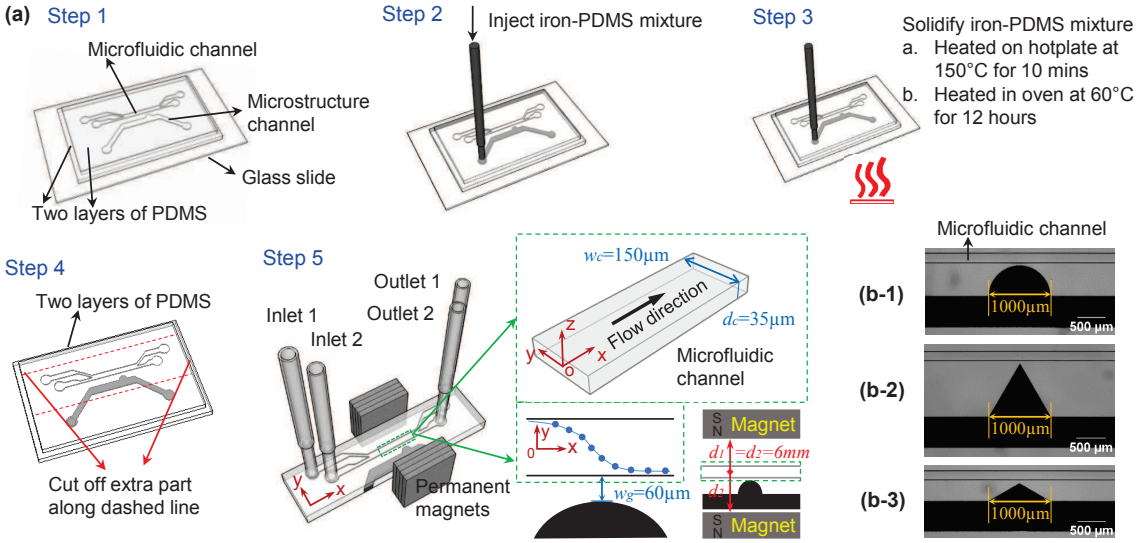

Figure 1. Fabrication process of the microfluidic device. (a) is the schematic illustration of the basic fabrication steps (not to scale). The microfluidic channel has a width w_c=150 μm and a depth d_c=35 μm; the gap distance between the microstructure and the microfluidic channel is w_g=60 μm. (b-1)–(b-3) are the micro-photographies of the three different shapes for the microstructure: half circle, 60° isosceles triangle and 120° isosceles triangle.

Compared to the existing methods, our method has several advantages. First, different iron mass ratio can be used to adjust the magnetic permeability and thus the magnetic forces. Second, the fluidic and structural channels are fabricated from a simple one-step soft-lithography process. It is flexible to design different shapes and sizes of the microstructure, and place them within micrometer accuracy to the fluidic channel. Moreover, our method is particularly attractive for applications concerning biological objects (e.g., living cells), because the microstructures are situated outside the fluidic channels, and will not cause contamination to the cells.

2. CONCEPT AND EXPERIMENT

Fig. 1 (a) shows an overview of the microdevice that consists of a fluidic channel and microstructures. The fluidic channel has two inlets and two outlets. External permanent magnets magnetize the soft magnetic structures to provide local magnetic field gradients,

which in turn result in the deflection of magnetic particles. A magnetic particle exposed to a magnetic field experiences a magnetic force, $\mathbf{F}_m$. The other important force acting on the particles is the hydrodynamic drag force $\mathbf{F}_d$ due to the surrounding fluid. The two forces, $\mathbf{F}_m$ and $\mathbf{F}_d$, thus determine the movement of the magnetic particle.

The major steps of the fabrication process are summarized in Fig. 1(a). Two channels, fluidic and structural, are first made in Polydimethylsiloxane (PDMS) with soft-lithography technique [30]. A mixture of iron powder and PDMS in the liquid form is then injected into the structural channel and allowed to solidify. Fig. 1(b-1), (b-2) and (b-3) show the three different microstructure shapes: half circle, 60° isosceles triangle and 120° isosceles triangle studied in this paper. These three structures are denoted as half circle, 60° triangle and 120° triangle hereinafter. The microstructures all have the same base length or diameter of 1000 μm. The nearest distance between the microstructures and the fluidic channel is $w_g = 60\,\mu$m.

Shape selection In the current study, we emphasize on the flexibility of the proposed technique. We chose three representative shapes, half circle, 60° isosceles triangle and 120° isosceles triangle, to show the influence of the shape, as shown in Fig. 1(b). From prior works [14], it is known that soft magnetic microstructures of *half circle* and *triangle* shapes can generate strong magnetic fields to trap magnetic particles, so we select these two shapes. Additionally, the magnetic force acting on particles is proportional to the magnetic field gradients mentioned in Eq. (1), so we explored if a sharper angle can generate a larger magnetic field gradient thus a stronger magnetic force to attract particles. For these reasons, 60° and 120° triangles were chosen. Actually, there is a range of possible shapes to generate localized magnetic forces, e.g., square, rectangle, symmetric or asymmetric triangles. To find the 'best' shape for particle separation will require a systematic investigation and optimization.

Gap distance selection While the gap distance is one of the factors affecting magnetic separation, the gap distance was kept fixed at 60 microns in this study. This is because the effect of the gap distance w_g has been relatively well understood from previous study in the literature [14], and the results suggest that a closer distance of the magnetic microstructure from the microfluidic channel can generate larger magnetic forces. In this study, w_g = 60 μm was the closest distance we could achieve with a low-cost manufacturing technique, which we described in detail in a published work [31]. With conventional methods of producing master molds, e.g. SU-8 or DRIE, the distance can be easily reduced to ten microns [30].

In this study, we fabricated several microdevices to study the factors influencing the sorting performance. Two mass ratios of iron powder to PDMS were used in this study, at 1:1 to 2:1 respectively. The microfluidic channel width was designed to be w_c = 150 μm and 250 μm to study the effect of fluidic channel width.

2.1. Microfluidic Device Fabrication. The microfluidic device was fabricated in PDMS using a soft lithography techniques [30]. Master molds were manufactured in a dry film photoresist (MM540, 35 μm thick, DuPont) by lithographic patterning [32]. A layer of dry film resist was first laminated onto a copper plate using a thermal laminator. After ultra-violet (UV) exposure through a transparency photo mask (10,000 dpi, CAD/Art Services Inc), the exposed dry film was developed, rinsed and dried to obtain the master mold. PDMS base and initiator were throughly mixed, degassed, and then cast on the master. After curing, the PDMS replica was peeled off from the master, cut and punched, and then bonded with another thin PDMS layer after corona surface treatment. Using this method, microfluidic and microstructure channels with rectangular cross sectional shape were fabricated.

The PDMS device was placed onto a flat glass slide which served as a supporting substrate as displayed in step 1 of Fig. 1(a). Next, carbonyl iron powders (C3518, Sigma-Aldrich) were thoroughly mixed with a pre-mixed liquid PDMS. The mixture of the iron

powders and PDMS was degassed, and subsequently injected into the microstructure channel with a syringe pump shown in step 2. Immediately after filling the iron-PDMS mixture, the microdevice was heated on a hotplate at 150°C for 10 minutes to cure the mixture, as in step 3 of Fig. 1(a). The fast curing process is critical to prevent the agglomeration and sedimentation of the iron powders, which have a density of 7.8 g/mL. The fast curing ensures a homogeneous distribution of the iron powders into the composite matrix. The microfluidic device was heated in an oven at 60 °C for another 12 hours to ensure complete curing and strong bonding. In step 4, excessive parts were cut off after curing of the iron-PDMS mixture

The device was placed in the center of two pieces of parallel permanent magnets [14, 33], as shown in step 5 of Fig. 1(a). The separation distance of the permanent magnets was 12 mm. The placement at the center ensured a uniform external magnetic field in the microfluidic channel. Note that a uniform magnetic field has zero field gradients, and thus will not cause a force on the magnetic particles. The non-zero magnetic field gradients are due to the magnetized iron-PDMS microstructures only, allowing us to study the effects of the soft magnetic microstructures on the sorting performance.

2.2. Materials. Micron-sized magnetic particles (MPS5UM, Magsphere) were used as model particles. The magnetic particles have a mean diameter of 5 μm, and are synthesized by embedding superparamagnetic iron oxide crystals into a polystyrene matrix. The particles have a density of 2.5 g/mL. The magnetic particles were suspended in 45.6% (w/w) aqueous glycerol solution whose viscosity is about 5 mPa·s. The larger viscosity reduced the particle sedimentation. The original solution of 5 μm superparamagnetic particles (2.5% w/w) were diluted 500 times in the aqueous glycerol solution. The final particle concentration was 3.26×10^5/mL. The glycerol solution with magnetic particles was injected into inlet 1 as the particle solution, and 45.6% glycerol solution was injected to inlet 2 as the buffer solution. Surfactant Tween 20 was added to both solutions at a concentration of 0.5% w/w to prevent particle adhesion to channel walls and particle agglomeration.

2.3. Experimental Set-up. The microdevice was placed on an inverted microscope stage (IX73, Olympus). Four pieces of $1'' \times 1'' \times \frac{1}{8}''$ thick permanent magnets (BX0X02, KJ Magnetics, Inc.) were placed symmetrically on each side of the microdevice, in Fig 1(a). The microfluidic devices were illuminated by a fiber optic light for transmission bright-field imaging. The flow rates to the inlets were controlled separately by two syringe pumps (NE-300, New Era and KDS 200, KDS Scientific). To maintain good stability of the flow, small syringes (1 mL) were used to minimize the effect of the motor's step motion. To record particle trajectories, a high-speed camera (Phantom Miro M310, Vision Research) was used to capture videos. In experimental data analysis, ImageJ [34] was used to extract the particle trajectory, from which the translational velocity v_p and the vertical position z_p can be calculated.

3. THEORY AND SIMULATION

3.1. Force Analysis of Magnetic Particles.

Magnetic force Exposed to a magnetic field, a magnetic particle experiences a magnetic force, $\mathbf{F}_m$, which is expressed as [35]

$$\mathbf{F}_m = \mu_0 \int_V (\mathbf{M} \cdot \nabla)\mathbf{H} dV, \tag{1}$$

where $\mu_0 = 4\pi \cdot 10^{-7}\ H \cdot m^{-1}$, is the vacuum permeability; $\mathbf{H}$ is the magnetic field intensity; $\mathbf{M}$ is the field-dependent particle magnetization; V is the volume. In a static magnetic field, $\mathbf{H}$ and $\mathbf{M}$ are co-linear, $\mathbf{M} = M(H)\frac{\mathbf{H}}{H} = M(H)\mathbf{e_H}$, where H and M are the magnitudes of $\mathbf{H}$ and $\mathbf{M}$ respectively, and $\mathbf{e_H} \equiv \mathbf{H}/H$ is a unit vector indicating the direction of the applied magnetic field.

Assuming a small variation of the integrand over magnetic particles, equation (1) can be written as [36]

$$\mathbf{F}_m \simeq V_p M_p \mathbf{G}, \tag{2}$$

where V_p is the volume of the magnetic particle and $\mathbf{G}$ is the magnetic field gradient in the direction of $\mathbf{H}$, given by

$$\mathbf{G} = \mu_0(\mathbf{e}_\mathbf{H} \cdot \nabla)\mathbf{H}. \tag{3}$$

Thus, the magnetic force on a magnetic particle is the product of the particle magnetic moment, $V_p M_p$, and $\mathbf{G}$, which is referred to as the effective magnetic field gradient [36].

The external magnetic field at the center of the parallel magnets was approximately 0.23 T and its corresponding magnetization of pure Fe_3O_4 material is $M = 1.9 \times 10^5 A/m$ according to the magnetization curve [37].

Note that the magnetic particle used in this study is composed of a Fe_3O_4 core and an external polymer matrix. If the entire particle volume V_p is used to compute the force, an equivalent M_p accounting for the non-magnetic polymer volume must be used accordingly. The equivalent magnetization of the superparamagnetic particles is therefore $M_p = M\frac{V_m}{V_p}$, where $\frac{V_m}{V_p}$ stands for the volume ratio of the Fe_3O_4 core to the entire particle volume. Based on the data sheet provided by the manufacturer, we calculated the value of $M_p \approx 11000$ A/m. In addition, our numerical simulations also confirmed the accuracy of M_p.

Stokes drag force In low Reynolds number microfluidic systems, the dominating force acting on particles from the fluid is the hydrodynamic drag force $\mathbf{F}_d$ defined by Stokes' law [38],

$$\mathbf{F}_d = 3\pi\eta D(\mathbf{v}_f - \mathbf{v}_p) f_D \tag{4}$$

where η is the fluid viscosity, $\mathbf{v}_p$ is the particle velocity, and $\mathbf{v}_f$ is the velocity of suspending fluid, and f_D is the hydrodynamic drag force coefficient. The coefficient, f_D, accounts for the increased fluid resistance when the particle moves near the microfluidic channel surface

[39, 40, 41]. It has a form of

$$f_D = \left[1 - 0.6526(\frac{D}{D+2z'}) + 0.1475(\frac{D}{D+2z'})^3 \right. \\ \left. -0.131(\frac{D}{D+2z'})^4 - 0.0644(\frac{D}{D+2z'})^5\right]^{-1}, \tag{5}$$

where $z\prime$ is the distance between the bottom of the particle and the channel surface.

Velocity profile in rectangular microchannels The velocity profile of laminar steady flows in rectangular channels can be expressed as an infinite sum of Fourier series [42]. To improve the computational speed, we used an algebraic approximation of the following form for channel aspect ratio $\alpha = d_c/w_c \leq 0.5$ [43],

$$v(y,z) = v_{max}[1 - (\frac{2y}{w_c})^m][1 - (\frac{2z}{d_c})^n]. \tag{6}$$

Natarajan and Lakshmanan [43] solved the $N-S$ momentum equation by a finite element method, and matched the velocity profile to the empirical equation to arrive at two flow parameters m and n as

$$m = 1.7 + 0.5\alpha^{-1.4} \tag{7}$$

$$n = \begin{cases} 2 & \text{for } \alpha <= \frac{1}{3} \\ 2 + 0.3(\alpha - \frac{1}{3}) & \text{for } \alpha >= \frac{1}{3} \end{cases} \tag{8}$$

The values of m and n by Natarajan and Lakshmanan yield profiles that are in good agreement with the experimental results of Holmes and Vermeulen [43].

The channel dimensions in this study are: the depth of microchannel d_c=35 μm , and the width of microfluidic channel w_c = 150 μm or 250 μm. The aspect ratio α thus satisfies the condition required by the approximate equations. Therefore, according to the

coordinate in Fig. 1(a), the velocity profile in rectangular microchannel is

$$v(y,z) = v_{ave}(\frac{m+1}{m})(\frac{n+1}{n})[1-(\frac{2y}{w_c})^m][1-(\frac{2z}{d_c})^n] \tag{9}$$

where v_{ave} is the average velocity in the x direction.

3.2. Numerical Simulation. We developed a method to simulate the trajectory of the magnetic particles. First, finite element software package FEMM [44] was used to simulate the magnetic field in the microfluidic channel. A custom-written Matlab program was employed to determine the particle position with respect to time by Newton's second law. Magnetic force distribution on the particle as a function of space can also be calculated to understand the effects of various factors on the particle trajectory and separation performance. The initial particle positions in the simulations have the same z coordinate as the experiment. In the experiment measurement, particles near the centerline of microfluidic channel were selected; and all sample particles were almost on the same z plane to ensure consistent and meaningful comparisons. Previous studies have suggested that the gravity can have important roles in determining the particle motions when the particles are heavier than the surrounding liquid [45, 46]. However, in our study, the effect of gravity can be safely neglected because the particle velocity in the z direction is negligible compared to the velocities in the x and y direction. The estimation of the velocity scales suggests that the velocity in the z direction is at least 100 times smaller than those in the x and y direction. It is thus reasonably accurate to assume the particle will stay in the same z plane during the process flowing through the fluid channel. As a result, 2-D simulations can be used as long as the particle location in z direction is known. In the comparison between the simulations and experiments, the z location was first obtained from experiment measurement, and subsequently used in the 2-D simulations.

Magnetic field The geometry of the same size with experiment was constructed in FEMM. The material of microfluidic channel was set as air. The relative magnetic permeability of the microstructure was set according to the mass ratio of the iron-PDMS composite, and the values were derived from the experimental data as reported in the literature [27, 47, 48]. At a mass ratio of 2:1, $\mu_r = 1.706$, and at a mass ratio of 1:1, $\mu_r = 1.45$. The NdFeB permanent magnets used the experiment have a grade of 42 MGOe, and the correct coercivity H_c was used in FEMM accordingly. The simulation domain was set as at least five times of the microdevice size. The boundary condition of magnets, microfluidic channel and microstructure channel were set as a mixed one to solve the static Maxwell's equations [44]. The magnetic field intensity H_x and H_y were exported by a script written in lua programing language, and saved in a text file. The magnetic field data was later imported to the Matlab program to calculate the magnetic force through Equation (2).

Particle trajectory The particle motion is calculated by Newton's second law [22, 38, 49]. At each time instance, the forces on the particle, $\mathbf{F}_m$ and $\mathbf{F}_d$, and the corresponding particle acceleration are calculated,

$$a_x = \frac{F_{dx} + F_{mx}}{m_p}, \tag{10}$$

$$a_y = \frac{F_{dy} + F_{my}}{m_p}. \tag{11}$$

The instantaneous position of a particle, r_x and r_y, are then computed over time by

$$r_x = x_0 + v_{0x}t + \frac{1}{2}a_x t^2, \tag{12}$$

$$r_y = y_0 + v_{0y}t + \frac{1}{2}a_y t^2, \tag{13}$$

where x_0 and y_0 are the initial location of the particle; $v_{0x} = v_{0y} = 0$ are the initial particle velocity; t is time; F_{dx} and F_{dy} are the x and y components of the hydrodynamic drag force; F_{mx} and F_{my} are the x and y components of the magnetic force; and m_p is the mass of the particle.

4. RESULTS AND DISCUSSION

When the iron-PDMS microstructure is placed between two external permanent magnets, it induces localized and strong forces on the magnetic particles in the direction perpendicular to the pressure-driven fluid flows. The separation of particles thus depends on the magnetic forces. According to Equation (2), the magnetic forces have a strong dependence on the magnetic field and its gradient, which, in turn, are affected by the shape of iron-PDMS microstructure, the mass ratio of iron-PDMS composite, and the width of the microfluidic channel. Additionally, the flow rate in the fluid channel affects the time experienced by the magnetic particle (residence time t_r), and thus the vertical deflection in the y-direction. In the following sections, systematic experiments and numerical simulations were used to examine the influence of these factors on the separation performance.

4.1. Effect of Microstructure Shape. The effect of iron-PDMS microstructure shapes on the particle transport is presented in this section. The three shape styles are half circle, 60° triangle, and 120° triangle, as shown in Fig. 2 (a-1), (b-1) and (c-1). All of microstructures were fabricated with the same base length of 1000 μm and were positioned at $w_g = 60\,\mu$m away from the fluidic channel. Fig. 2 (a-1), (b-1) and (c-1) compare the experimental and simulated particle trajectories due to the three soft magnetic microstructures respectively. It is evident from the comparison that the experimental trajectories were in good agreement with the simulation. The superparamagnetic particles were deflected towards the lower side of microfluidic channel because of the magnetic force induced by the iron-PDMS microstructures.

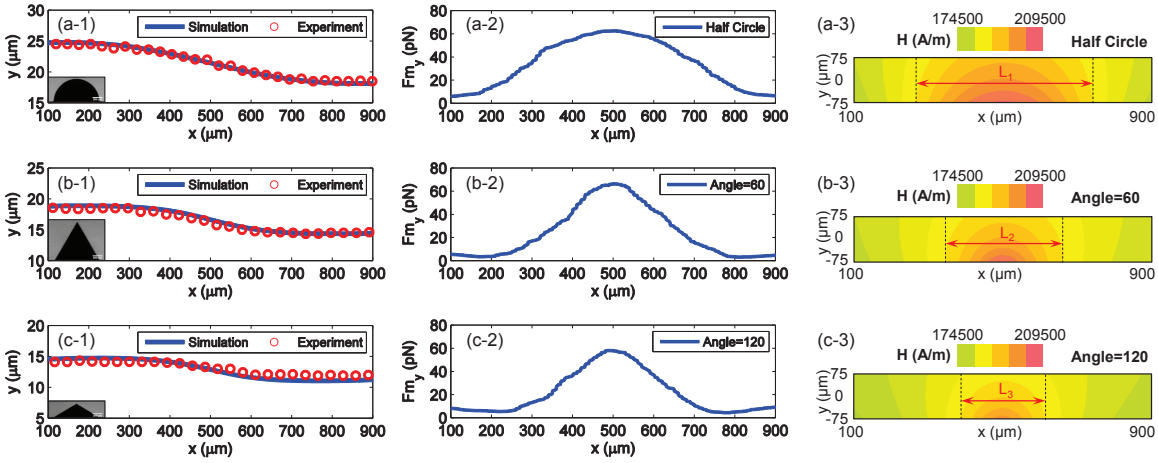

Figure 2. Effect of the microstructure shapes. (a-1), (b-1) and (c-1) compare the experimental (symbols) and simulated particle trajectories (lines) with the half circle, 60° triangle and 120° triangle microstructures; (a-2), (b-2) and (c-2) are the corresponding F_{my} from simulations; (a-3), (b-3) and (c-3) are the corresponding magnetic field intensity in the microfluidic channel. The flow rate is Q_1=Q_2=1.5 μL/min, the width of microfluidic channel is w_c = 150 μm, and the mass ratio of iron-PDMS is 2:1.

Note that the initial positions (y_0) of the particles in were slightly different in Fig. 2 (a-1), (b-1) and (c-1). This difference was due to the practical constraints of the experiments where there were limited number of particles. We used numerical simulations to evaluate the effect of y_0. For initial positions 15 μm $\leq y_0 \leq$ 25 μm, the resulted $\Delta y = y_1 - y_0$ changed by only 5.11%, 5.80% and 6.61% for the half circle, 60° and 120° triangles, respectively. In all experimental analysis, we ensured the condition 15 μm $\leq y_0 \leq$ 25 μm. The comparisons for different experiment conditions are thus considered consistent and meaningful.

Among the three shapes investigated, the half circle microstructure resulted in the largest deflection. This can be understood by the vertical magnetic force F_{my} calculated from the numerical simulations, as shown in Fig. 2 (a-2), (b-2) and (c-2). While the maximum F_{my} was about the same at 70 pN, the half circle iron-PDMS microstructure had a wider acting range in the channel to deflect the particle towards the lower wall side faster. To visualize the influence range, the distributions of magnetic field strength $|H|$ are plotted in Fig. 2 (a-3), (b-3) and (c-3). For the same variation range of $|H|$, the half circle structure

had a wider influence range (L_1), which is larger than those due to the 60° (L_2) and 120° (L_3) triangles.

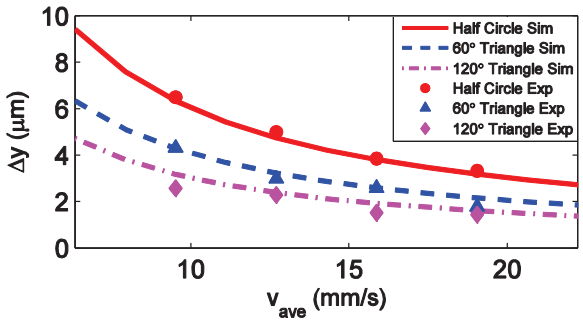

Figure 3. Effect of average linear flow velocity. $\Delta y = y_1 - y_0$ at different average linear flow velocity v_{ave} under three different microstructures. y_1 and y_0 are the positions of particles at outlet and inlet of the microfluidic channel respectively. For all experiments and simulations, the initial position is $y_0 \approx 20$ μm, the iron mass ratio is iron:PDMS (w/w)=2, and the width of microfluidic channel is w_c =150 μm. Lines and symbols represent simulation and experimental data, respectively.

When varying the average linear flow velocity, the deflection distance $\Delta y = y_1 - y_0$ decreases with increasing flow velocity for all microstructures, as shown in Fig. 3. The vertical deflection distance is the result of the competition of the vertical magnetic force and the viscous drag force. With an increasing flow velocity and a larger drag force, the residence time, t_r, of the particle within the influence range of F_{my} becomes shorter. Despite the same magnetic force (the same vertical velocity), Δy becomes smaller because of the shorter residence time t_r. For the all flow rates examined, the half circle had the best performance on particle deflection in the y-direction, since F_{my} effect range was wider, which had been discussed before; 60° triangle worked better than 120° triangle for the same reason.

4.2. Effect of Iron Mass Ratio of Composite. In addition to the shapes, the mass ratio of the iron powder can effect the separation performance, because it influences the magnetic permeability of the composite and the induced magnetic field. In this study, the mass ratio of between the iron and PDMS were varied from 1:1 to 2:1. In Fig.

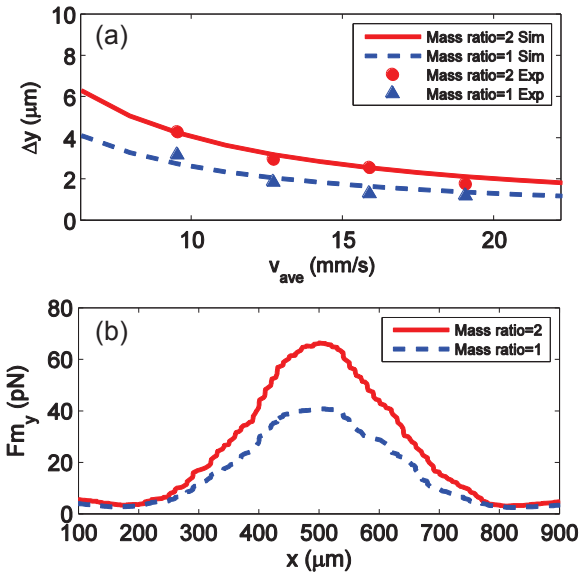

Figure 4. Effect of the iron mass ratio of the iron-PDMS composite. (a) $\Delta y = y_1 - y_0$ at different average linear flow velocity v_{ave} with the 60° triangle microstructure; y_1 and y_0 are the positions of particles at outlet and inlet of the microfluidic channel respectively; lines and symbols represent simulation and experimental data, respectively. (b) the corresponding magnetic force F_{my} from the simulations when v_{ave}= 9.52 mm/s. The width of microfluidic channel is w_c = 150 μm in all experiments and simulations.

4, the microstructure was the 60° triangle in order to study the effect of the mass ratio of iron powders. Fig. 4(a) shows that microstructure of iron:PDMS (w/w)=2 deflected the particles by a larger displacement in the y direction for all the average linear flow velocity v_{ave} than the microstructures made of iron:PDMS (w/w)=1. This is because the composite of iron:PDMS (w/w)=2 had a larger magnetic permeability μ_r = 1.706, while the microstructures of iron:PDMS (w/w)=1 had a smaller permeability, μ_r = 1.45 [27]. Therefore, a larger mass ratio of iron can produce stronger magnetic field gradients and larger magnetic forces to separate magnetic particles. Fig. 4(b) illustrates the magnetic force in the y direction acting on the 5 μm particles when v_{ave}= 9.52 mm/s. As can be seen in Fig. 4(b), the microstructure made of iron-PDMS (w/w)=2 had both a larger force and a wider acting range on the magnetic particle, leading to larger deflection of the particle towards the lower wall side.

Despite a small change from $\mu_r = 1.45$ to $\mu_r = 1.706$, the resultant forces almost doubled, as shown in Fig. 4(b). A mass ratio of 3 or larger would have a even better sorting performance on the magnetic particles. However, the iron-PDMS mixture with mass ratio of 3 was too viscous to be injected into the microstructure channels used in this study. If a larger mass ratio and a large force are needed, the microstructures can be designed to have wider cross sectional areas to allow the injection of the more viscous iron-PDMS mixture.

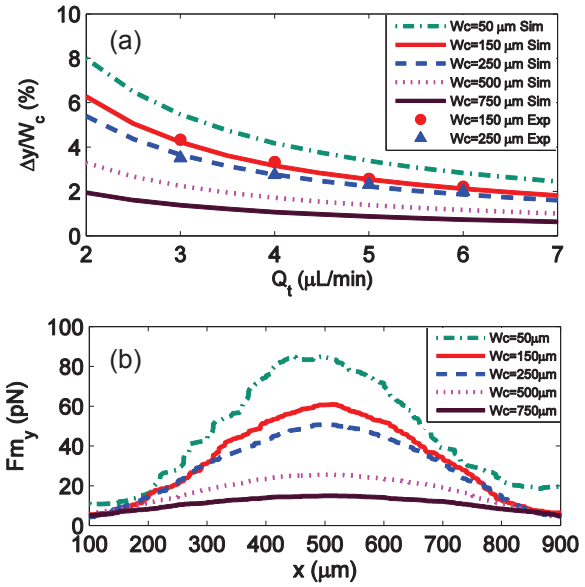

Figure 5. Effect of the width of the microfluidic channel. (a) $\Delta y = y_1 - y_0$ at different flow rates. y_1 and y_0 are the positions of particles at outlet and inlet of the microfluidic channel respectively. Lines and symbols represent simulation and experimental data, respectively. (b) the corresponding F_{my} from the simulations. The flow rate is Q_1=Q_2=1.5 μL/min. The particles all have approximately the same initial relative positions, $\frac{y_0}{(W_c/2)} = \frac{4}{15}$. The microstructure is half circle, and has a iron mass ratio iron:PDMS (w/w)=2.

4.3. Effect of Microfluidic Channel Width. The width of microfluidic channel, w_c, influences the particle separation as well. When w_c changes, the distance between the particle to the microstructure will be different, and thus the magnetic forces will be different. For a meaningful assessment of the effect of w_c, the flow rate Q_t was kept the

same. In addition, the initial positions of the particles, y_0 were chosen to have the same relative position with respect to the channel width, that is the same $\frac{y_0}{w_c}$ for all cases. In accordance, $\frac{\Delta y}{w_c}$ will be the measurement of the separation performance.

Unlike the previous two factors (shape and mass ratio of iron-PDMS) that only affect the magnetic force, the channel width, w_c affects both the drag force and the magnetic force. When w_c decreases, the pressure-driven velocity and drag force increase, and thus the particle residence time t_r will decrease. In the meantime, the particles are situated relatively closer to the iron-PDMS microstructure, thus the magnetic force will increase. These two effects have opposite influences on the particle deflection. To understand the combined effect of w_c, extensive simulations (w_c from 50 to 750 μm) were conducted. It can be found in Fig. 5(a) that under the condition of w_c=500 μm and 750 μm the deflection was so small, resulting in little separation considering the relatively large width of the fluidic channel. Although the deflection of w_c=50 μm was large enough, it was beyond the ability of the current fabrication technique. Nevertheless, these cases were calculated to show the trend of $\frac{\Delta y}{w_c}$ vs Q_t for each width. As a result, we chose w_c=150 μm and 250 μm to compare the experimental measurements with simulations, as shown in Fig. 5(a).

The experiments and simulations showed that the value of $\frac{\Delta y}{w_c}$ became larger when the microfluidic channel became narrower. This trend means that the effect of increasing F_{my} is more dominant over the effect of decreasing residence time. The magnetic force F_{my} showed a dramatic change when w_c was varied, in Fig. 5(b). As the channel width decreases, the rate of increase of F_{my} is faster than the linear rate of decrease of the residence time t_r, which is inversely proportional to the channel width.

4.4. Separation with Multiple Microstructures. In the above sections, it has been proved that single microstructure can result in the y-direction displacement of particles. To further enhance the separation, multiple microstructures were designed to test the practical use of our proposed devices. The half circular structure were chosen because of its superior performance, as shown in Fig. 6(a). The microfluidic channels had a width 150 μm,

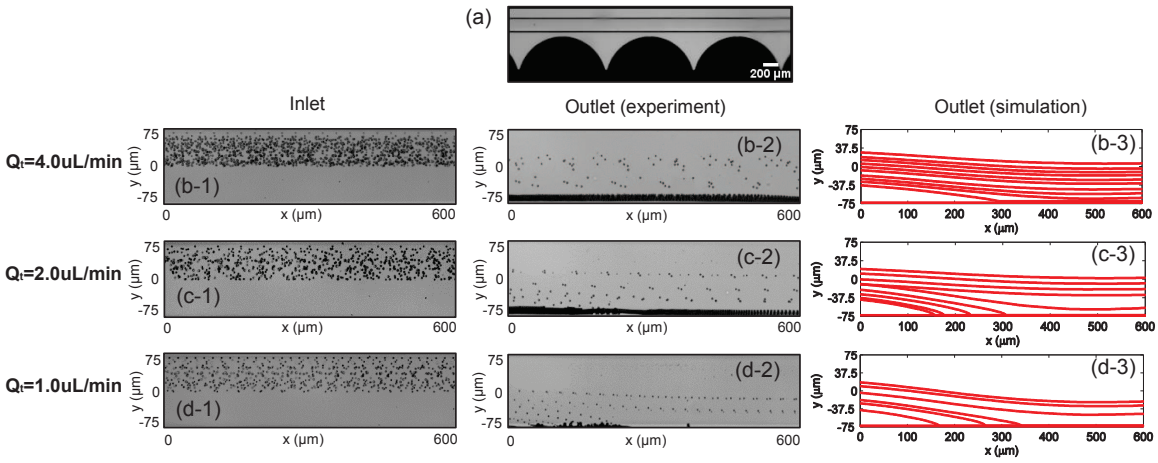

Figure 6. Separation of magnetic particles with multiple iron-PDMS microstructures. (a) image of connected half circle iron-PDMS microstructure. (b-1), (c-1) and (d-1) are the superposed images at the inlet of the microfluidic channels at different flow rates. (b-2) to (d-2), and (b-3) to (d-3) are the corresponding images at the outlets.

and were placed next to multiple (total 11) connected half circle microstructures made of iron:PDMS (w/w)=2. Solutions with magnetic particles entered into the top half of the fluid channel, as shown in Fig. 6 (b-1), (c-1) and (d-1). The magnetic particles were pulled towards the lower half, as shown in the superposed images captured at the channel outlets, in Fig. 6 (b-2), (c-2) and (d-2).

In practical applications, the magnetic particles occupy the entire upper half of the channel at the inlet. To achieve a complete separation, the particles near the top channel wall must be deflected by a distance of the half channel width. As can be seen in Fig. 6, complete separation was achieved at a total flow of 1.0 μL/min. The simulated particle trajectories agreed well with the experimental data.

In Fig. 6 (b-2) (c-2) (d-2), it seems that a higher flow rate would be likely to collect more particles than a slow flow rate. This seems counter-intuitive but can be explained as follows. At lower flow rate, some of the magnetic particles can be deflected to the channel wall before reaching to the outlet. When magnetic particles were attracted to the bottom surface, the friction between particles and channel wall would be large and the particles

moved slowly to the outlet. When the flow rate was small as Fig. 6 (d-2), most particles was absorbed to the bottom surface and stopped at the wall before they arrived at the outlet due to the weak pressure driven flow. When the flow rate was large as Fig. 6 (b-2), most particles were attracted to the wall just before the outlet. Further, because the pressure driven flow was strong enough to overcome the friction, more particle appeared at the channel outlet; additionally, the superposed images in Fig. 6 (b-2) (c-2) (d-2) were obtained with image stacks of the same time duration. That also means more particles moved through the channel when the flow rate was larger. It is true that the aggregated particles may have effect on the distribution of magnetic field distribution, if they are large enough compared to the microstructures. However, in our study, the particle solution was dilute, therefore the aggregated particles were small compared the microstructures which were several hundred microns.

The viscosity of the solution used in this study was 5 mPa·s, about 4–5 times more viscous than common aqueous biological solutions. Therefore, the throughput would be a few times higher when the device is used with less viscous solutions. Moreover, the throughput can be further improved with multiple parallel channels. Our proposed technique will be particularly useful for high-throughput particle/cell separation with short durations(e.g., minutes to hours), and during these operation time frames no iron particles can permeate into main microchannel.

5. CONCLUSIONS

We proposed and demonstrated a simple and low-cost method for fabricating microfluidic devices for enhanced separation of magnetic particles. The microfluidic devices integrated soft magnetic microstructures next to microfluidic channels, with a distance of tens of micrometers. The induced magnetic fields and gradients resulted in strong forces that can deflect magnetic particles perpendicular to the pressure-driven flow. By simulating the

magnetic fields and computing the corresponding magnetic forces, a numerical simulation method was developed to predict the particle trajectory, and showed good agreement with the experimental data.

Systematic experiments and simulations were conducted to study the effect of several relevant factors on the separation of superparamagnetic particles, including the microstructure shape, the mass ratio of the iron-PDMS microstructure, and the microfluidic channel width. Important findings include: first, half circular iron-PDMS microstructure causes larger deflections of the particles than isosceles triangle shaped structures; second, a larger mass ratio of the iron-PDMS composite results in larger magnetic forces; third, narrow microfluidic channels separate magnetic particles more efficiently than wider channels when operating at the same flow rate.

Our approach presents an efficient and simple method to separate magnetic particles in microfluidics. Compared to the existing techniques, the current method will reduce the chance of contamination to cells because the microstructures are located outside the fluid channel. In addition, the distance between the microfluidic channel and the microstructure channel can be adjusted to control the magnetic forces. As such, the proposed microfluidic devices are promising, and have potential in areas such as high throughput separation of biological cells tagged with micro/nano-magnetic particles.

REFERENCES

[1] Safarik Ivo and Safarikova Mirka. Use of magnetic techniques for the isolation of cells. *Journal of Chromatography B: Biomedical Sciences and Applications*, 722(1-2):35–53, 1999.

[2] Ivo Safarik and Mirka Safarikova. Magnetic techniques for the isolation and purification of proteins and peptides. *BioMagnetic Research and Technology*, 2:7, 2004.

[3] L. Yang, J.C. Lang, P. Balasubramanian, K.R. Jatana, r D. Schulle, A. Agrawal, M. Zborowski, and J.J. Chalmers. Optimization of an enrichment process for circulating tumor cells from the blood of head and neck cancer patients through depletion of normal cells. *Biotechnology and Bioengineering*, 102(2):521–534, 2009.

[4] P. Balasubramanian, J.C. Lang, K.R. Jatana, B. Miller, E. Ozer, M. Old, D.E. Schuller, A. Agrawal, T.N. Teknos, Jr. T.A. Summers, M.B. Lustberg, M. Zborowski, and J.J. Chalmers. Multiparameter analysis, including emt markers, on negatively enriched blood samples from patients with squamous cell carcinoma of the head and neck. *PLoS ONE*, 7(7), 2012.

[5] R.M. Shenkman, J.J. Chalmers, B.J. Hering, N. Kirchhof, and K.K. Papas. Quadrupole magnetic sorting of porcine islets of langerhans. *Tissue Engineering - Part C: Methods*, 15(2):147–156, 2009.

[6] T. Lund-Olesen, M. Dufva, and M.F. Hansen. Capture of dna in microfluidic channel using magnetic beads: Increasing capture efficiency with integrated microfluidic mixer. *Journal of Magnetism and Magnetic Materials*, 311(1 SPEC. ISS.):396–400, 2007.

[7] E. Verpoorte. Beads and chips: New recipes for analysis. *Lab on a Chip*, 3(4):60N–68N, 2003.

[8] M.A.M. Gijs. Magnetic bead handling on-chip: New opportunities for analytical applications. *Microfluidics and Nanofluidics*, 1(1):22–40, 2004.

[9] Nicole Pamme. Magnetism and microfluidics. *Lab. Chip*, 6:24–38, 2006.

[10] Martin AM Gijs, Frederic Lacharme, and Ulrike Lehmann. Microfluidic applications of magnetic particles for biological analysis and catalysis. *Chemical Reviews*, 110(3):1518–1563, 2009.

[11] N.-T. Nguyen. Micro-magnetofluidics: Interactions between magnetism and fluid flow on the microscale. *Microfluidics and Nanofluidics*, 12(1-4):1–16, 2012.

[12] Majid Hejazian, Weihua Li, and Nam-Trung Nguyen. Lab on a chip for continuous-flow magnetic cell separation. *Lab on a Chip*, 15(4):959–970, 2015.

[13] Ki-Ho Han and A. Bruno Frazier. Continuous magnetophoretic separation of blood cells in microdevice format. *Journal of Applied Physics*, 96(10):5797–5802, 2004.

[14] Nan Xia, TomP. Hunt, BrianT. Mayers, Eben Alsberg, GeorgeM. Whitesides, RobertM. Westervelt, and DonaldE. Ingber. Combined microfluidic-micromagnetic separation of living cells in continuous flow. *Biomedical Microdevices*, 8(4):299–308, 2006.

[15] Yuh 'Adam' Lin, Tak-Sing Wong, Urvashi Bhardwaj, Jia-Ming Chen, Edward McCabe, and Chih-Ming Ho. Formation of high electromagnetic gradients through a particle-based microfluidic approach. *Journal of Micromechanics and Microengineering*, 17(7):1299, 2007.

[16] J. Svoboda. A realistic description of the process of high-gradient magnetic separation. *Minerals Engineering*, 14(11):1493–1503, 2001.

[17] J.H.P. Watson. Magnetic filtration. *Journal of Applied Physics*, 44(9):4209–4213, 1973.

[18] J. Do, J.-W. Choi, and C.H. Ahn. Low-cost magnetic interdigitated array on a plastic wafer. *IEEE Transactions on Magnetics*, 40(4 II):3009–3011, 2004.

[19] T. Deng, M. Prentiss, and G.M. Whitesides. Fabrication of magnetic microfiltration systems using soft lithography. *Applied Physics Letters*, 80(3):461–463, 2002.

[20] A. Rida and M.A.M. Gijs. Manipulation of self-assembled structures of magnetic beads for microfluidic mixing and assaying. *Analytical Chemistry*, 76(21):6239–6246, 2004.

[21] T. Lund-Olesen, H. Bruus, and M.F. Hansen. Quantitative characterization of magnetic separators: Comparison of systems with and without integrated microfluidic mixers. *Biomedical Microdevices*, 9(2):195–205, 2007.

[22] E.P. Furlani and K.C. Ng. Analytical model of magnetic nanoparticle transport and capture in the microvasculature. *Physical Review E - Statistical, Nonlinear, and Soft Matter Physics*, 73(6), 2006.

[23] K. Smistrup, B.G. Kjeldsen, J.L. Reimers, M. Dufva, J. Petersen, and M.F. Hansen. On-chip magnetic bead microarray using hydrodynamic focusing in a passive magnetic separator. *Lab on a Chip - Miniaturisation for Chemistry and Biology*, 5(11):1315–1319, 2005.

[24] E.P. Furlani and Y. Sahoo. Analytical model for the magnetic field and force in a magnetophoretic microsystem. *Journal of Physics D: Applied Physics*, 39(9):1724–1732, 2006.

[25] David W Inglis, Robert Riehn, RH Austin, and JC Sturm. Continuous microfluidic immunomagnetic cell separation. *Applied Physics Letters*, 85(21):5093–5095, 2004.

[26] Caroline Derec, Claire Wilhelm, Jacques Servais, and Jean-Claude Bacri. Local control of magnetic objects in microfluidic channels. *Microfluidics and Nanofluidics*, 8(1):123–130, 2010.

[27] Magalie Faivre, Renaud Gelszinnis, Jérôme Degouttes, Nicolas Terrier, Charlotte Rivière, Rosaria Ferrigno, and Anne-Laure Deman. Magnetophoretic manipulation in microsystem using carbonyl iron-polydimethylsiloxane microstructures. *Biomicrofluidics*, 8(5):054103, 2014.

[28] Adam C. Siegel, Sergey S. Shevkoplyas, Douglas B. Weibel, Derek A. Bruzewicz, Andres W. Martinez, and George M. Whitesides. Cofabrication of electromagnets and microfluidic systems in poly(dimethylsiloxane). *Angewandte Chemie - International Edition*, 45(41):6877–6882, 2006.

[29] Say Hwa Tan, Benoît Semin, and Jean-Christophe Baret. Microfluidic flow-focusing in ac electric fields. *Lab on a chip*, 14(6):1099–106, 2014.

[30] J.C. McDonald, D.C. Duffy, J.R. Anderson, D.T. Chiu, H. Wu, O.J.A. Schueller, and G.M. Whitesides. Fabrication of microfluidic systems in poly(dimethylsiloxane). *Electrophoresis*, 21(1):27–40, 2000.

[31] Ran; P. Brames David; Wang Cheng Zhang, Ziyan; Zhou. A low-cost fabrication system for manufacturing soft-lithography microfluidic master molds. *Micro and Nanosystems*, 7(1):4–12, 2015.

[32] R. Zhou and C. Wang. Acoustic bubble enhanced pinched flow fractionation for microparticle separation. *Journal of Micromechanics and Microengineering*, 25(8), 2015.

[33] R. Gelszinnis, M. Faivre, J. Degouttes, N. Terrier, R. Ferrigno, and A.-L. Deman. Magnetophoretic manipulation in microsystem using i-pdms microstructurs. In *17th International Conference on Miniaturized Systems for Chemistry and Life Sciences*, volume 1, pages 146–148, 2013.

[34] M.D. Abramoff, P.J. MagalhÃčes, and S.J. Ram. Image processing with imagej. *Biophotonics International*, 11(7):36–41, 2004.

[35] A. Engel and R. Friedrichs. On the electromagnetic force on a polarizable body. *American Journal of Physics*, 70(4):428–432, 2002.

[36] Kristian Smistrup, Minqiang Bu, Anders Wolff, Henrik Bruus, and Mikkel Fougt Hansen. Theoretical analysis of a new, efficient microfluidic magnetic bead separator based on magnetic structures on multiple length scales. *Microfluidics and Nanofluidics*, 4:565–573, 2008.

[37] Van Cuong Nguyen and Quoc Hue Pho. Preparation of chitosan coated magnetic hydroxyapatite nanoparticles and application for adsorption of reactive blue 19 and ni2+ ions. *The Scientific World Journal*, 2014(273082), 2014.

[38] T. Zhu, F. Marrero, and L. Mao. Continuous separation of non-magnetic particles through negative magnetophoresis inside ferrofluids. In *2010 IEEE 5th International Conference on Nano/Micro Engineered and Molecular Systems*, pages 1006–1011, 2010.

[39] Peter Ganatos, Sheldon Weinbaum, and Robert Pfeffer. A strong interaction theory for the creeping motion of a sphere between plane parallel boundaries. part 1. perpendicular motion. *Journal of Fluid Mechanics*, 99:739–753, 1980.

[40] Michelle E. Staben, Alexander Z. Zinchenko, and Robert H. Davis. Motion of a particle between two parallel plane walls in low-reynolds-number poiseuille flow. *Physics of Fluids*, 15(6):1711–1733, 2003.

[41] Gokul P. Krishnan and David T. Leighton. Inertial lift on a moving sphere in contact with a plane wall in a shear flow. *Physics of Fluids*, 7(11):2538–2545, 1995.

[42] Frank M White. *Viscous fluid flow*. New York : McGraw-Hill, 2nd ed edition, 1991.

[43] Thomas F. Irvine R. K. Shah, A. L. London and James P. Hartnett. *Laminar Flow Forced Convection in Ducts*. Academic Press, 1978.

[44] David Meeker. Finite element method magnetics. *FEMM*, 4:32, 2010.

[45] Ehsan Samiei, Hojatollah Rezaei Nejad, and Mina Hoorfar. A dielectrophoretic-gravity driven particle focusing technique for digital microfluidic systems. *Applied Physics Letters*, 106(20), 2015.

[46] Hojatollah Rezaei Nejad, Ehsan Samiei, Ali Ahmadi, and Mina Hoorfar. Gravity-driven hydrodynamic particle separation in digital microfluidic systems. *RSC Adv.*, 5:35966–35975, 2015.

[47] D.E. El-Nashar, S.H. Mansour, and E. Girgis. Nickel and iron nano-particles in natural rubber composites. *Journal of Materials Science*, 41(16):5359–5364, 2006.

[48] Jiaxing Li, Mengying Zhang, Limu Wang, Weihua Li, Ping Sheng, and Weijia Wen. Design and fabrication of microfluidic mixer from carbonyl iron-pdms composite membrane. *Microfluidics and Nanofluidics*, 10(4):919–925, 2011.

[49] J. Zhu, L. Liang, and X. Xuan. On-chip manipulation of nonmagnetic particles in paramagnetic solutions using embedded permanent magnets. *Microfluidics and Nanofluidics*, 12(1-4):65–73, 2012.

III. MULTIPHASE FERROFLUID FLOWS FOR MICRO-PARTICLE FOCUSING AND SEPARATION

Ran Zhou, Cheng Wang

Department of Mechanical & Aerospace Engineering

Missouri University of Science and Technology

Rolla, Missouri 65409

Tel: (573) 341-4636, Fax: (573) 341-4607

Email: wancheng@mst.edu

ABSTRACT

Ferrofluids have demonstrated great potential for a variety of manipulations of diamagnetic (or non-magnetic) micro-particles/cells in microfluidics, including sorting, focusing, and enriching. By utilizing size dependent magnetophoresis velocity, most of the existing techniques employ single phase ferrofluids to push particles towards channel walls. In this work, we demonstrate a novel strategy for focusing and separating diamagnetic micro-particles by using the laminar fluid interface of two co-flowing fluids – a ferrofluid and a non-magnetic fluid. Next to the microfluidic channel, microscale magnets are fabricated to generate strong localized magnetic field gradients and forces. Due to the magnetic force, diamagnetic particles suspended in the ferrofluid phase migrate across the ferrofluid stream at size-dependent velocities. Because of the low Reynolds number and high Péclet number associated with the flow, the fluid interface is sharp and stable. When the micro-particles migrate to the interface, they are accumulated near the interface, resulting in effective focusing and separation of particles. We investigated several factors that affect the focusing and separation efficiency, including susceptibility of the ferrofluid, distance between the

microfludic channel and microscale magnet, and width of the microfluidic channel. This concept can be extended to multiple fluid interfaces. As an example, complete separation of micro-particles was demonstrated by using a three-stream multiphase flow configuration.

1. INTRODUCTION

Microfluidics enables a diverse range of manipulations (e.g., focusing, separating, trapping, and enriching) of micrometer-sized objects, and has played an increasingly important role for applications that involve single cell biology [1] and the detection and diagnosis of diseases [2]. In microfluidic devices, methods that are commonly used to manipulate cells or particles include the utilization of hydrodynamic effects [3, 4, 5, 6] and externally applied field gradients that induce forces on cells/particles, such as electrical fields [7, 8, 9], optical fields [10, 11, 12, 13, 14], magnetic fields [15, 16, 17, 18], and acoustic fields [5, 19, 20]. Techniques that are based on hydrodynamic effects are known as passive methods, and often rely on appropriate channel designs to direct particles of different sizes into separate flow streamlines. The dimensions of the channels have implications for the applicable separation sizes. Among the various active methods that use external force fields, the magnetic field has advantages for applications concerning living matters, such as biological cells, because magnetic fields do not generate heat. Magnetic field is in contrast to electrical and optical fields, which often lead to temperature rises in the system and, thus, may potentially cause damage to cells due to the resulting high energy [21].

Trapping and separation techniques that are based on magnetic forces have become popular during the last few years [16, 22]. The two general methods for utilizing magnetic fields are: positive and negative magnetophoresis. In positive magnetophoresis, magnetic particles migrate towards regions of higher magnetic field gradient. Commonly, magnetic particles are deflected from the direction of laminar flow by a perpendicular magnetic field. The deflection velocity depends on the magnetic susceptibility, particle size, and flow rate. Thus, magnetic particles of different sizes can be separated from each other and from

non-magnetic materials [23]. This mechanism has been used to trap cells by labeling the target bioparticles with functionalized magnetic beads [16, 24, 25]. However, it is both time consuming and expensive to label and remove the magnetic particles from the target cells prior to further analysis. In negative magnetophoresis, diamagnetic particles that are suspended in magnetic solutions are repelled away from regions of higher magnetic field gradients (e.g., magnet sources) due to magnetic buoyancy force [26]. Further, most synthetic and biological particles are diamagnetic; therefore, label-free manipulation can be attained with negative magnetophoresis for practical applications.

Ferrofluids are stable colloidal suspensions of surfactant-coated magnetic nanoparticles in aqueous or organic solutions [27]. Due to their large magnetic susceptibility, ferrofluids have been extensively used as magnetic solutions in negative magnetophoresis-based cell separation techniques. For example, to address the perceived limitation of magnetic labeling of a target cell population, Kose et al. [28] developed a novel microfluidic platform that uses bio-compatible ferrofluids for the controlled manipulation and rapid separation of both microparticles and living cells. This low-cost platform exploits the differences in particle sizes and shapes to achieve rapid and efficient separation. Yellen's [29] and Kose's [28] groups have developed stabilizing surfactants and synthesized bio-compatible ferrofluids [30].

Focusing particles into a tight stream is an essential step in many applications, such as microfluidic cell cytometry, and particle sorting [31]. Magnetic focusing in ferrofluid is non-invasive and well suited for handling bio-particles [16, 22, 32]. Liang et al. [30, 33] proposed a method for focusing diamagnetic particles carried by a ferrofluid flow through a T-shaped microchannel using a single permanent magnet. Wilibanks et al. [34] and Zeng et al. [35, 36] presented methods for concentrating diamagnetic particles in ferrofluid flows by means of two repulsive or attractive magnets that were positioned symmetrically or asymmetrically on either side of a particle flowing channel. In these studies, millimeter or centimeter-sized permanent magnets (PMs) helped to realize focusing. However, because

these magnets were much larger than the microfluidic channel, it was difficult to align and place them precisely. A slight misalignment of the permanent magnets could lead to a relatively larger change within the fluidic channel. Further, strong and bulky magnets had to be used to provide large magnetic fields that could generate large magnetic forces. This requirement greatly increased the difficulty in integrating magnetic particle manipulation in portable and standalone lab-on-a-chip platforms. Moreover, most of the previous studies have focused the particles or cells to the wall of the microchannel [21, 37]. Due to the increasing friction near the wall, the velocity of the particles significantly reduced and thus hindered the throughput.

To overcome the limitations using existing techniques, we propose a simple and novel strategy to achieve focusing and separating of diamagnetic microparticles with laminar fluid interfaces and micro-fabricated magnets. In this technique, a ferrofluid and a non-magnetic fluid co-flowing in a microfluidic channel form a stable fluid interface. Under the magnetic fields from the neighboring microscale magnet, diamagnetic particles that are suspended in the ferrofluid phase migrate towards and accumulate at the fluid interface, leading to particle focusing. This mechanism can be further exploited to separate particles of different sizes.

In our technique, both the fluid interface and microscale magnets can be precisely controlled for micrometer accuracy, and thereby achieve precise focusing. Additionally, microscale magnets provide localized high magnetic field gradients, resulting in larger magnetic forces for high-throughput operations. Moreover, focusing particles to the interface can keep particles far away from the channel wall and thus avoid the friction of the wall. The location of the interface can be additionally controlled by adjusting the flow ratios to achieve both precise focusing and separation of diamagnetic particles. In this work, we investigated experimentally the effects of several factors, including ferrofluid concentration, gap distance between the microfluidic channel and the microscale magnet, and the microfluidic channel width on the focusing performance of particles.

2. CONCEPT AND EXPERIMENT

2.1. Overview of Device and Working Principle. Fig. 1(a) presents a brief fabrication process of our microdevice. A schematic of the microdevice consisting of a microfluidic channel and a microstructure channel is displayed in step 1. The microstructure channel was fabricated parallel to the microfluidic channel with a distance of 60 – 100 microns. A mixture of neodymium (NdFeB) powders and PDMS was injected into the microstructure channel in step 2. Immediately after filling the NdFeB-PDMS mixture, the microdevice was heated to cure the mixture, as in step 3. Then the microstructure channel, with the cured NdFeB-PDMS mixture, was magnetized by an impulse magnetizer to form a permanent 'microscale magnet', which can generate localized high magnetic field gradients.

Fig. 1(b) illustrates the working principle of the proposed technique. Water and water-based ferrofluid, containing 7 μm and 2 μm (in diameter) diamagnetic particles, were injected from inlet 1 and 2 respectively. The flow rates of inlet 1 and inlet 2 were kept the same in all of the following experiments. Due to the non-zero magnetic susceptibility difference between the particles and the ferrofluid, the particles experience a magnetic repulsion force, $\mathbf{F}_m$, and migrate towards the fluid interface. Upon arriving at the interface, the particles will stay at the interface because, in the other phase – the water is also diamagnetic, and thus negligible magnetic force will act on the particles to induce further migration. The other important force acting on the particles is the hydrodynamic drag force, $\mathbf{F}_d$, due to the flow of fluids. These two forces, $\mathbf{F}_m$ and $\mathbf{F}_d$, thereby determine the movement of the diamagnetic particle, as in Fig. 1(b). Due to the size difference, the smaller particles (2 μm) move more slowly in the y direction than the larger (7 μm) particles. At the end of the fluid channel, the larger particles are focused at the interface, while the smaller particles remain widespread throughout the ferrofluid stream.

2.2. Fabrication of Microfluidic Device. A microfluidic device was fabricated in PDMS using a soft lithography technique [38]. Master molds were manufactured in a dry film photoresist (MM540, 35 μm thick, DuPont) by lithographic patterning [39]. In this

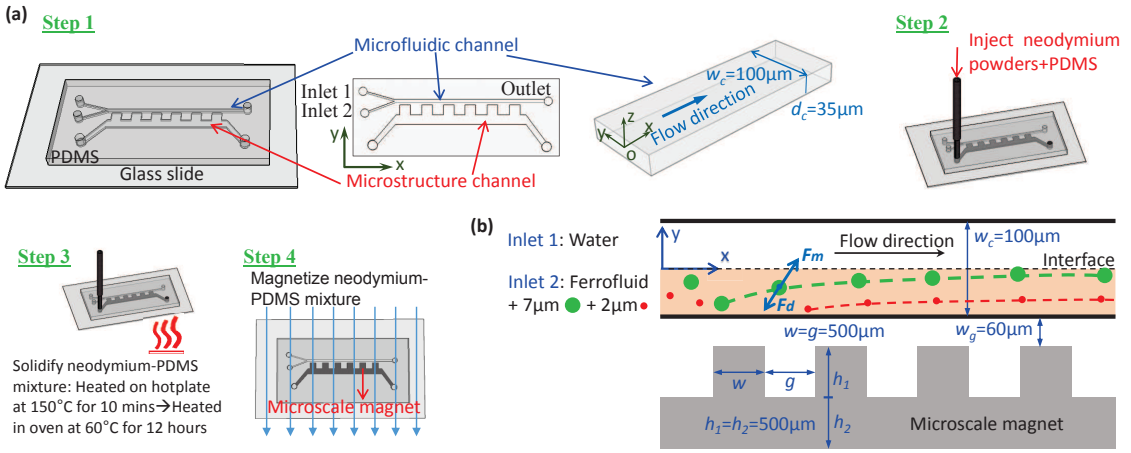

Figure 1. Fabrication process of microdevices, and basic principle of particle movement. (a) illustrates the fabrication steps of the microdevice; (b) is the enlarged drawing of the microfluidic channel and the basic principle of particle movement in a ferrofluid. The microfluidic channel has a width of w_c=100 μm and a depth of d_c=35 μm; the gap distance between the microscale magnet and the microfluidic channel is w_g=60 μm; the size of the microscale magnet is $w = g = h_1$=h_2 = 500 μm.

method, a layer of dry film resist was first laminated onto a copper plate using a thermal laminator. After ultra-violet (UV) exposure through a transparency photo mask (10,000 dpi, CAD/Art Services Inc), the exposed dry film was developed in a sodium carbonate solution, rinsed in water, and dried by compressed air to obtain a master mold. The PDMS base and initiator were throughly mixed, degassed, and then poured onto the master molds. After overnight curing at 60°C, the PDMS replica was peeled from the master, cut and punched, and then bonded with a flat glass slide after corona surface treatment. Using this method, microfluidic and microstructure magnet channels were fabricated with rectangular cross sections.

Next, neodymium (NdFeB) micro-powders (MQFP-B-20076-089, Magnequench International Inc) were thoroughly mixed with a pre-mixed liquid PDMS. The mixture of neodymium powders and PDMS was degassed, and subsequently injected into the microscale magnet channel with a syringe pump. Immediately after being filled with the NdFeB-PDMS mixture, the microdevice was heated on a hotplate at 150°C for 10 minutes

to cure the mixture. The fast curing process was critical to avoid agglomeration and sedimentation of the neodymium powders. The fast curing ensured a homogeneous distribution of the neodymium powders into a composite matrix. The microfluidic device was heated in an oven at 60°C for another 12 hours to ensure complete curing and strong bonding. After the mixture was cured, the resulting solid NdFeB-PDMS microstructure was permanently magnetized by an impulse magnetizer (IM 10, ASC Scientific) and became a microscale permanent magnet, as shown in Fig. 1(a).

2.3. Materials. EMG 408 ferrofluid was obtained from Ferrotec (USA) Corporation with a reported initial magnetic nanoparticle concentration of 1.2 % (v/v) and saturation magnetization (M_s) of 6.6 mT. The initial viscosity and magnetic susceptibility of EMG 408 ferrofluid were μ=2 mPa·s and χ_f=0.5, respectively. In our experiments, the original ferrofluid was diluted to 0.6 % (v/v) and 0.36 % (v/v) with distilled water. Diamagnetic particles of 2 μm and 7 μm in diameter and a density of 1.05 g/mL were used as model particles. The original solutions of 2 μm and 7 μm particles (2.5% w/w) were diluted with 0.6 % (v/v) or 0.36 % (v/v) ferrofluid to 5000 and 200 times, respectively. The final particle concentrations were 1.14×10^6 mL^{-1} and 6.62×10^5 particles mL^{-1}. Surfactant Tween 20 was added to both solutions at a concentration of 0.5% (w/w) to prevent particle adhesion to channel walls and particle agglomeration. The ferrofluid solution with particles was injected into inlet 2 as the particle solution, and distilled water was injected into inlet 1 as the buffer solution.

2.4. Particle Visualization and Analysis. The microfluidic device was placed on an inverted microscope stage (IX73, Olympus) and illuminated by a fiber optic light for transmission of bright-field imaging. The flow rates to the inlets were controlled individually by two syringe pumps (NE-300, New Era and KDS 200, KDS Scientific). To maintain good stability of the flow, small syringes (1 mL) were used to reduce the effect of the motor's step

motion. To record particle trajectories, a high-speed camera (Phantom Miro M310, Vision Research) was used to capture videos. In the experimental data analysis, ImageJ [40] was used to extract the particle trajectories and positions.

3. THEORETIC BACKGROUND AND SIMULATION

3.1. Force and Velocity Analysis of Microparticles.

Magnetic force Diamagnetic particles experience a negative magnetophoretic force, $\mathbf{F}_m$, in a ferrofluid when subjected to a non-uniform magnetic field [21, 35, 41],

$$\mathbf{F}_m = -\mu_0 V_p (\mathbf{M}_f \cdot \nabla)\mathbf{H}, \tag{1}$$

where μ_0 is the magnetic permeability of free space; V_p is the volume of the particle; the magnetization of ferrofluid $\mathbf{M}_f$ is collinear with a static magnetic field $\mathbf{H}$ produced by a microscale magnet. In general, the magnitude of $\mathbf{M}_f$, M_f is determined using the Langevin function, $L(\alpha)$ [30],

$$\frac{M_f}{\phi M_d} = L(\alpha) = coth(\alpha) - \frac{1}{\alpha}, \tag{2}$$

$$\alpha = \frac{\pi \mu_0 M_d H d^3}{6 k_B T}, \tag{3}$$

where $M_d = 4.379 \times 10^5$ A/m is the saturation moment of the magnetic nanoparticles, as calculated from the manufacturer-provided saturation magnetization of ferrofluid; H is the magnetic field magnitude; d is the average diameter of the magnetic nanoparticles; k_B is the Boltzmann constant; and T is the temperature of the ferrofluid.

Particles are repelled away from the microscale magnet owing to the negative sign in Eq.(1), suggesting that $\mathbf{F}_m$ is directed against the magnetic field gradient [33]. In our study, the microscale magnets had larger magnetic gradients and small magnetic field strength ($H \leq 90000$ A/m); thus, the susceptibility of the ferrofluid was approximately constant.

Based on the following basic relationships of $\mathbf{M}_f = \chi_f \mathbf{H}$ and $\mathbf{B} = \mu_0(1 + \chi_f)\mathbf{H}$, Eq. (1) can be simplified as follows [42],

$$\mathbf{F}_m = \frac{\pi D^3}{6\mu_0}\Delta\chi(\mathbf{B}\cdot\nabla)\mathbf{B}, \tag{4}$$

where $\mathbf{B}$ is magnetic flux density; $\Delta\chi = \chi_p - \chi_f$ represents the difference in the magnetic susceptibilities, between the particle (χ_p) and the surrounding fluid (χ_f); D is the diameter of the diamagnetic particle. In our study, the magnetic susceptibilities of ferrofluid χ_f were 0.25 and 0.15 for the ferrofluid with concentrations of 0.6% (v/v) and 0.36% (v/v) respectively. The magnetic susceptibility of polystyrene particles χ_p was much smaller [30], on the order of 10^{-6}; therefore, the diamagnetic particles were repelled away from the regions of higher magnetic field strength because of $\Delta\chi < 0$, which agreed with the negative sign in Eq. (1).

Stokes drag force In low Reynolds number microfluidic systems, the hydrodynamic drag force, $\mathbf{F}_d$, acting on particles in microchannels, rises due to the relative motion between the particles and the surrounding fluid, and can be defined by Stokes' law [21],

$$\mathbf{F}_d = 3\pi\eta D(\mathbf{v}_f - \mathbf{v}_p)f_D, \tag{5}$$

where η is the fluid viscosity; $\mathbf{v}_p$ is the particle velocity; $\mathbf{v}_f$ is the velocity of suspending fluid; f_D is the hydrodynamic drag force coefficient. The coefficient, f_D, accounts for the increased fluid resistance when the particle moves near the microfluidic channel surface [32, 43]. f_D has a form of

$$f_D = \left[1 - \frac{9}{16}\left(\frac{r}{r+d'}\right) + \frac{1}{8}\left(\frac{r}{r+d'}\right)^3 - \frac{45}{256}\left(\frac{r}{r+d'}\right)^4 - \frac{1}{16}\left(\frac{r}{r+d'}\right)^5\right]^{-1}, \tag{6}$$

where d' is the distance between the bottom of the particle and the channel surface; $r = D/2$ is the radius of the particle.

Magnetophoresis velocity The velocity caused by magnetic force – magnetophoresis velocity – is a critical parameter influencing the time used by particles to reach the interface and focusing performance. In low Reynolds number microfluidic flows, the movement of particles can be regarded as a quasi-steady motion for each instantaneous time period because of the small mass of microparticles. Therefore, the balance between the two forces leads to

$$\mathbf{F}_m + \mathbf{F}_d = 0. \tag{7}$$

Based on Eq. (5) and (7), the magnetophoresis velocity, can be derived as, [16, 23]

$$\mathbf{v}_m = \frac{\mathbf{F}_m}{3\pi\eta D f_D}. \tag{8}$$

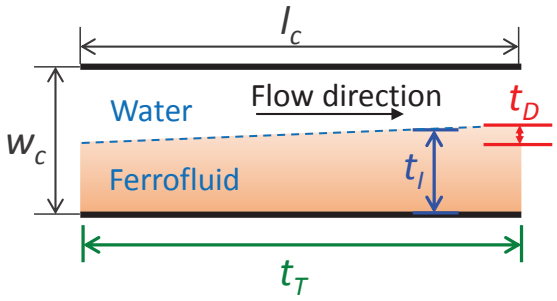

Figure 2. Illustration of the time scales related to particle movement in a two-phase flow system: travel time, t_T; interface time, t_I; diffusion time, t_D. w_c and l_c, are the width and length of the microfluidic channel, respectively.

3.2. Time Scales and Focusing Criteria. To better study the focusing of particles, the relationship between three time scales, namely interface time, travel time, and diffusion time, are introduced in this section. The general concept of these three time scales is illustrated in Fig. 2.

First, interface time is defined as the time used by the particles to reach the interface between the water and ferrofluid. Interface time t_I can thus be expressed as

$$t_I = \frac{w_c/2}{|\overline{v}_{my}|}, \tag{9}$$

where w_c is the width of the microfluidic channel, and is equal to 100 μm or 150μm in this study; $|\overline{v}_{my}|$ is the average magnetophoresis velocity in the y direction. Based on Eq. (4) and (8), t_I can be specifically explained by the following equation,

$$t_I = \frac{9\mu_0\eta f_D w_c}{D^2|\Delta\chi||(\mathbf{B}\cdot\nabla)B_y|}, \tag{10}$$

where $|(\mathbf{B}\cdot\nabla)B_y|$ is the absolute value of the magnetic field in the y direction. This will be further discussed in Eq. (15).

Second, travel time is the time spent by the particles on moving from the inlet of the microfluidic channel to the outlet and can be written as,

$$t_T = \frac{l_c}{|\overline{v}_{fx}|}, \tag{11}$$

where l_c=20000 μm is the length of the microfluidic channel; $|\overline{v}_{fx}| = \frac{Q_t}{d_c w_c}$ is the average fluid velocity in the x direction, where Q_t is the total flow rate, and d_c is the depth of the microfluidic channel and is equal to 35 μm, as shown in Fig. 1(a).

Third, diffusion will take place owing to different kinds of solutions that have different concentrations of magnetic nanoparticles. Diffusion time is defined as the time scale for nanoparticles to diffuse for distance d_x,

$$t_D = \frac{d_x^2}{2D_{diff}}, \tag{12}$$

where D_{diff} is the diffusion coefficient and has a value of 4.34×10^{-11} m^2/s, as determined by the Einstein relation [44]. To maintain a sharp interface, the diffusion distance, width d_x, must be much smaller than $w_c/2$. This criterion is equivalent to a very large Péclet number, i.e., $Pe = \dfrac{w_c \overline{v}_{fx}}{D_{diff}} \gg 1$.

The above analysis shows that the focusing of particles in a microfluidic channel can be achieved when the following two criteria are met: (a) $t_I \leq t_T$ and (b) $Pe \gg 1$. In our study, $Pe = 3.29 \times 10^4$ was obtained for the smallest flow rate, 3 μL/min; thus, the second criterion, to keep a sharp interface, was always met. Accordingly, the relationship between t_I and t_T is mainly discussed in the following analysis to explain and help the reader understand focusing performance.

3.3. Numerical Simulation of Magnetic Field. The magnetic field in the microfluidic channel was simulated with a finite element software package, FEMM [45], to develop a deeper understanding of the magnetic forces. The geometry of the same size was constructed with experiments. The magnetic property of the ferrofluid was determined according to its concentration [30]. The magnetic coercivity of the microscale magnet was determined from experimental data, with H_c being approximately 94000 A/m. The simulation domain was set to be at least five times of the microdevice size. The boundary condition of the simulation domain was set an asymptotic boundary condition to solve the static Maxwell's equations [45]. The magnetic flux densities B_x and B_y, were exported by a script written in Lua programing language, and saved in a text file. The magnetic field data were later imported to the Matlab program to calculate the magnetic field distribution, which was used to understand the effects of various factors on the magnetic forces, and focusing performance. According to Eq. (4), with all other material properties fixed, $\mathbf{F}_m$ is proportional to $(\mathbf{B} \cdot \nabla)\mathbf{B}$, which can be expressed as follows [46, 47],

$$(\mathbf{B} \cdot \nabla)\mathbf{B} = (B_x \frac{\partial B_x}{\partial x} + B_y \frac{\partial B_x}{\partial y})\mathbf{i} + (B_x \frac{\partial B_y}{\partial x} + B_y \frac{\partial B_y}{\partial y})\mathbf{j}. \tag{13}$$

In the microfluidic devices used in our experiments, $(\mathbf{B}\cdot\nabla)B_x$ changed little because our design is symmetric in the x direction, while $(\mathbf{B}\cdot\nabla)B_y$ in the microfluidic channel was non-uniform due to the different distance from the microscale magnet and the varying structures. Accordingly, the value of $(\mathbf{B}\cdot\nabla)B_y$ was critical to the magnetic force in Eq. (8) and the magnetophoresis velocity in Eq. (4), and thus can influence the movement of particles. In the following part, the absolute value of $(\mathbf{B}\cdot\nabla)B_y$, i.e.,

$$|(\mathbf{B}\cdot\nabla)B_y| = \sqrt{(B_x\frac{\partial B_y}{\partial x} + B_y\frac{\partial B_y}{\partial y})^2}, \tag{14}$$

will be used to explain the focusing and separation of diamagnetic microparticles.

4. RESULTS AND DISCUSSION

Based on the focusing criterion of $t_I \leq t_T$, the focusing performance depends on the susceptibility of the ferrofluid and the magnetic field (and its gradients) due to the microscale magnets. These, in turn, are affected by several factors, including the concentration of ferrofluid, the gap distance between the microfluidic channel and the microscale magnet, and the width of the microfluidic channel. In this study, systematic experiments were conducted to examine the influence of these factors on focusing performance. The results are presented in the following sections. With a thorough understanding of the characteristics of particle focusing, a complete separation of particles of different sizes was attained with multiple fluid interfaces.

4.1. Effect of Ferrofluid Concentration on Focusing Performance. Since the ferrofluid property is critical for the interface time t_I according to Eq. (10), the effect of ferrofluid concentration on focusing performance was investigated experimentally. As can be seen from Figs. 3 (a-1) and (a-2), with 0.6%(v/v) ferrofluid at $Q_t = 3\,\mu$L/min, almost all 7 μm particles were pushed onto the interface between the water and ferrofluid, while with the 0.36%(v/v) ferrofluid, the 7 μm particles spread ranged from y=-20 μm to y=0

μm. This suggested that a high concentration of ferrofluid was beneficial for the focusing performance of particles.

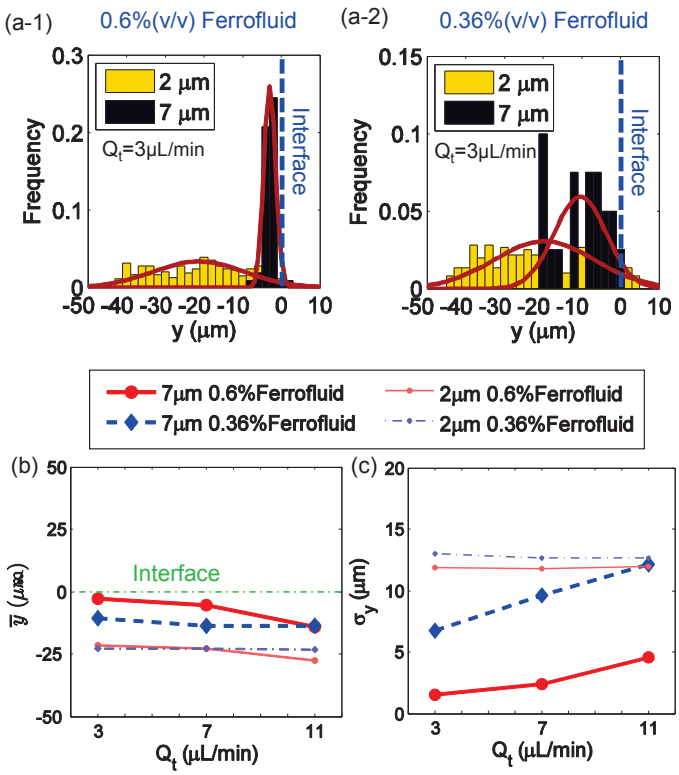

Figure 3. Effect of ferrofluid concentration on particle focusing. (a-1) and (a-2) are the Gaussian distribution of the particle's y location at the outlet when the concentration of ferrofluid is 0.6% (v/v) and 0.36% (v/v), respectively; total flow rate Q_t is 3.0 μL/min for (a-1) and (a-2). (c) and (d) are the mean y location of $\overline{y}$ and its standard deviation σ_y for particles distribution at the outlet under different Q_t. For each group, the flow rates of inlet 1 and inlet 2 are the same, Q_1=Q_2; the width of the microfluidic channel is w_c=100 μm; the gap distance is w_g=60μm.

From the expression of t_I in Eq. (10), the time used by particles to reach the interface is inversely proportional to the susceptibility difference, $|\Delta\chi|$, between the particles and the surrounding fluid. As mentioned before, the magnetic susceptibility χ_f of 0.6% and 0.36% ferrofluid is 0.25 and 0.15, respectively, so t_I of 0.6% ferrofluid is smaller than that of 0.36% ferrofluid, indicating that it would be more likely to meet the focusing criterion of $t_I \leq t_T$ for higher concentration of ferrofluid, in which diamagnetic particles can be pushed towards

the fluid interface more efficiently. In the meantime, almost no deflection was observed for the 2 μm particles in either 0.6% or 0.36% ferrofluid, as shown in Figs. 3 (a-1) and (a-2). It is noted that t_I was also a function of the size of particles, which was $t_I \propto 1/D^2$. For smaller (2 μm) particles, the time needed to reach the interface was much longer than that required for the 7 μm particles, which meant that it was more difficult for the 2 μm particles to meet the focusing criterion for each concentration. To study the overall effect of ferrofluid concentration on the focusing performance under different total flow rates Q_t, the mean y location, $\overline{y}$ and the standard deviation σ_y of 7 μm and 2 μm particles are shown in Figs. 3 (b) and (c). Fig. 3(b) illustrates that, for 7 μm particles, the mean y location $\overline{y}$ in 0.6% ferrofluid was closer to the interface than that in 0.36% ferrofluid. Fig. 3(c) shows that the corresponding standard deviation σ_y of 7 μm particles in 0.6% ferrofluid was smaller, meaning that there was a more concentrated distribution. When varying the flow rate Q_t, the mean y location $\overline{y}$ of both 0.6% and 0.36% ferrofluid became farther from the interface and the standard deviation σ_y was larger, implying a worse focusing performance. The reason was that the vertical deflection distance was the result of the competition between the vertical magnetic force and the viscous drag force. With an increasing flow rate, the hydrodynamic force effect became stronger, and t_T decreased. At a higher flow rate, not all of the particles were able to reach the interface before exiting the outlet. Thus, the focusing criterion $t_I \leq t_T$ set the upper flow rate limit to achieve effective focusing. As shown in Figs. 3 (b) and (c), the mean y location of 2 μm particles,at the outlet was about 25 μm from the interface, and nearly the same at the inlet. The corresponding standard deviation was large for both ferrofluid concentrations, which agrees with the results shown in Figs. 3 (a-1) and (a-2).

4.2. Effect of Gap Distance on Focusing Performance. The geometric designs of microdevices have important implications on focusing performance, according to previous studies [48]. It has been shown by other researchers [48] that the gap distance between the microscale magnet and the microfluidic channel can affect the magnetic field distribution,

so we examined the effect of the gap distance on focusing performance. In Fig. 6 (a-1), it can be observed that particles were pushed towards the interface when the gap distance w_g = 60 μm. When w_g was 100 μm, the spread range was much wider, and no obvious focusing happened, as shown in Fig. 6 (a-2).

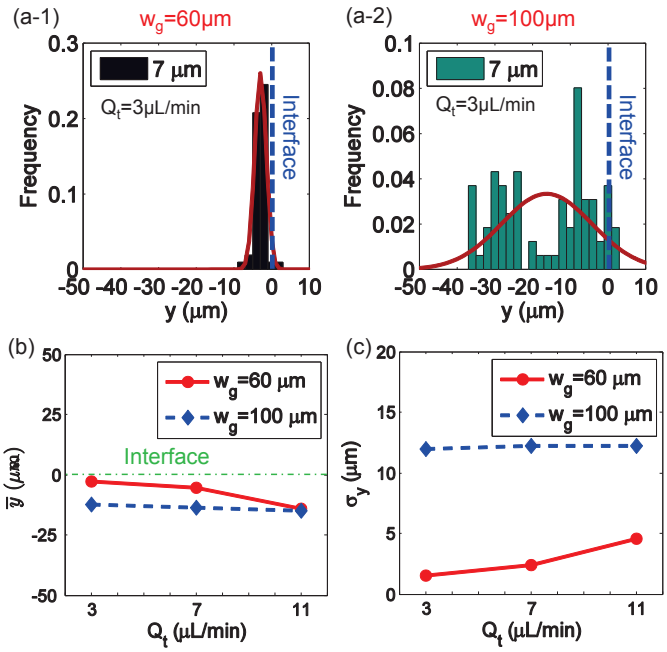

Figure 4. Effect of the gap distance on particle focusing. (a-1) and (a-2) are the Gaussian distribution of particles y location at the outlet when the gap distance w_g is 60 μm and 100 μm, respectively; total flow rate Q_t is 3.0 μL/min for (a-1) and (a-2). (b) and (c) are the mean y location $\overline{y}$ and its standard deviation σ_y of particles distribution at the outlet under different Q_t. For each group, the flow rates of inlet 1 and inlet 2 are the same, Q_1=Q_2; the width of microfluidic channel is w_c=100 μm; ferrofluid concentration is 0.6% (v/v).

In Figs. 6(b) and (c), $\overline{y}$ and σ_y of 7 μm particles are presented for different total flow rates, with two different gap distances. The smaller gap distance demonstrated better focusing for all flow rates tested. The mean location, $\overline{y}$ was closer to the fluid interface with smaller gap distance. The standard deviation σ_y of w_g= 60 μm was smaller than 5 μm for each flow rate; while that of w_g= 100 μm was larger than 10 μm. In Figs. 6 (b) and (c), it is clear that, for the group of w_g= 60 μm, the increase of total flow rate Q_t had a negative effect on focusing performance, including a longer distance from the interface and

a larger standard deviation of particle distribution. This observation can be attributed to the decreasing t_I. With a gap distance of 100 μm, neither $\overline{y}$ nor σ_y had an obvious change as the total flow rate varied. The results suggest that the microscale magnet was too far away from the microfluidic channel, and the resulting magnetic force was too weak to cause significant particle defection in the y direction.

To understand the reason for a different focusing performance for each gap distance, the average value of $|(\mathbf{B}\cdot\nabla)B_y|_{avg}$ across the fluid channel at different x locations was calculated, as shown in Fig 5. Generally, $|(\mathbf{B}\cdot\nabla)B_y|_{avg}$ of w_g=60 μm was larger than that of w_g=100 μm at each x location, so the magnetic force was larger and had a shorter t_I according to Eq. (10). Accordingly, when w_g was 60 μm, there was a greater possibility of meeting the focusing criterion of $t_I \leq t_T$ which would result in a better focusing performance of the particles.

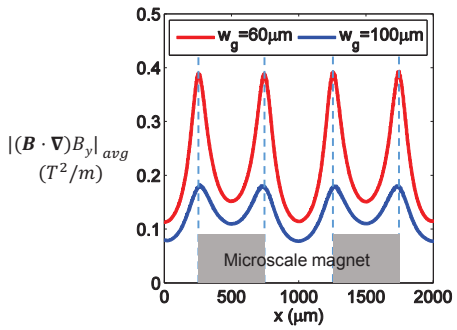

Figure 5. The average value of $|(\mathbf{B}\cdot\nabla)B_y|$ at different x locations when w_g=60 μm and w_g=100 μm. The width of the microfluidic channel is w_c=100 μm.

4.3. Effect of Microfluidic Channel Width on Focusing Performance. The width of the microfluidic channel is another geometric factor that can affect the focusing performance of particles in the ferrofluid flows. Figs. 5 (a-1) and (a-2) compare the focusing of particles in two microfluidic channels with w_c=100 μm and w_c=150 μm channel under the same flow rate Q_t. The microfluidic channel of w_c=100 μm had a better focusing performance than the w_c=150 μm channel, including both the smaller distance from the

interface, as displayed in Fig. 5 (b), and the smaller standard derivation presented in Fig. 5 (c) for each total flow rate. Also, a similar trend of $\overline{y}$ and σ_y under different Q_t can be seen in Fig. 5 (b) and (c), respectively.

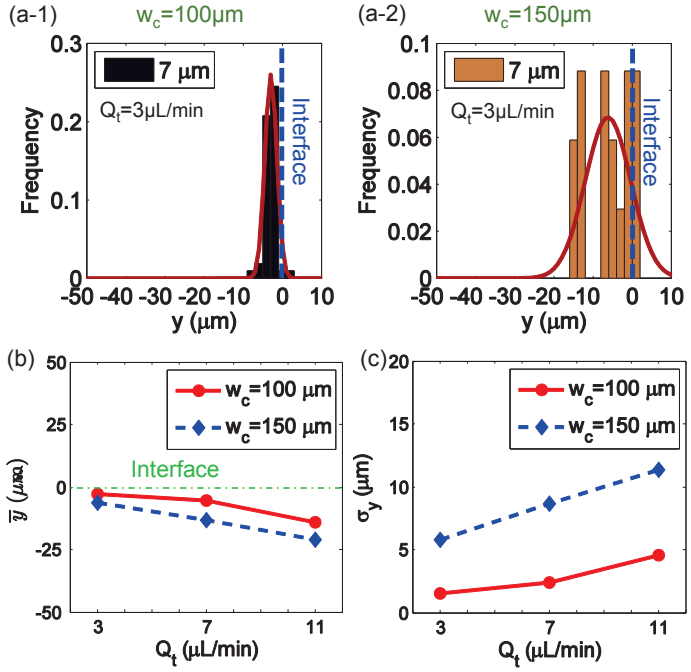

Figure 6. Effect of the microfluidic channel width on particle focusing. (a-1) and (a-2) are the Gaussian distribution of particles y location at the outlet when the channel width w_c is 100μm and 150μm, respectively; total flow rate Q_t is 3.0μL/min for (a-1) and (a-2). (b) and (c) are the mean y location $\overline{y}$ and its standard deviation σ_y of particles distribution at the outlet under different Q_t. For each group, the flow rates of inlet 1 and inlet 2 are the same, Q_1=Q_2; the gap distance is w_g=60 μm; ferrofluid concentration is 0.6% (v/v).

The ratio of $\frac{t_T}{t_I}$ was analyzed to understand the reason that was responsible for the better focusing performance of a narrower microfluidic channel. The expression of $\frac{t_T}{t_I}$ can be expressed as the following equation,

$$\frac{t_T}{t_I} = \frac{1}{9}\frac{l_c d_c}{\mu_0 \eta f_D}\frac{D^2|\Delta\chi|}{Q_t}|(\mathbf{B}\cdot\nabla)B_y|. \tag{15}$$

In the above equation, $\frac{t_T}{t_I}$ is proportional to the value of $|(\mathbf{B}\cdot\nabla)B_y|$, when the fluid properties and total flow rate are fixed. Its values at different x locations within a structural period were chosen for magnetic field analysis to better understand the deflection of particles in channels with different widths. As can be seen in Fig. 7, $|(\mathbf{B}\cdot\nabla)B_y|$ value of w_c=100 μm was larger than that of w_c=150 μm at each x location. Therefore, the ratio of $\frac{t_T}{t_I}$ was larger for a narrower channel, indicating that it was easier to meet the focusing criterion of $t_I \leq t_T$. A narrower channel was more beneficial for focusing particles to the interface between the water and ferrofluid and increasing the throughput.

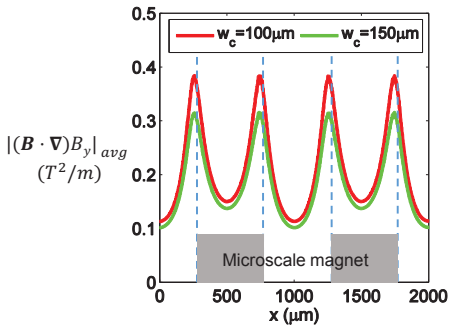

Figure 7. The average value of $|(\mathbf{B}\cdot\nabla)B_y|$ at different x locations with the different channel width w_c. The gap distance w_g was kept at 60 μm, and the ferrofluid concentration was 0.6% (v/v).

4.4. Multiphase Ferrofluid Flows for Micro-particle Separation. Based on the analysis presented above, large particles can be effectively focused onto the interface by choosing the correct parameters to meet the two criteria. Although the focusing of smaller particles seemed poor for all experimental conditions tested, this fact could be effectively exploited to separate particles of different sizes by using multiple interface configurations. Here, a three inlet device was used to demonstrate the separation of different sized particles, as shown in Fig. 8(a). Water, 0.6% (v/v) ferroluid, and 0.6% (v/v) ferrofluid containing 2 μm and 7 μm particles, were introduced into inlets 1, 2, and 3 at flow rates Q_1, Q_2, and

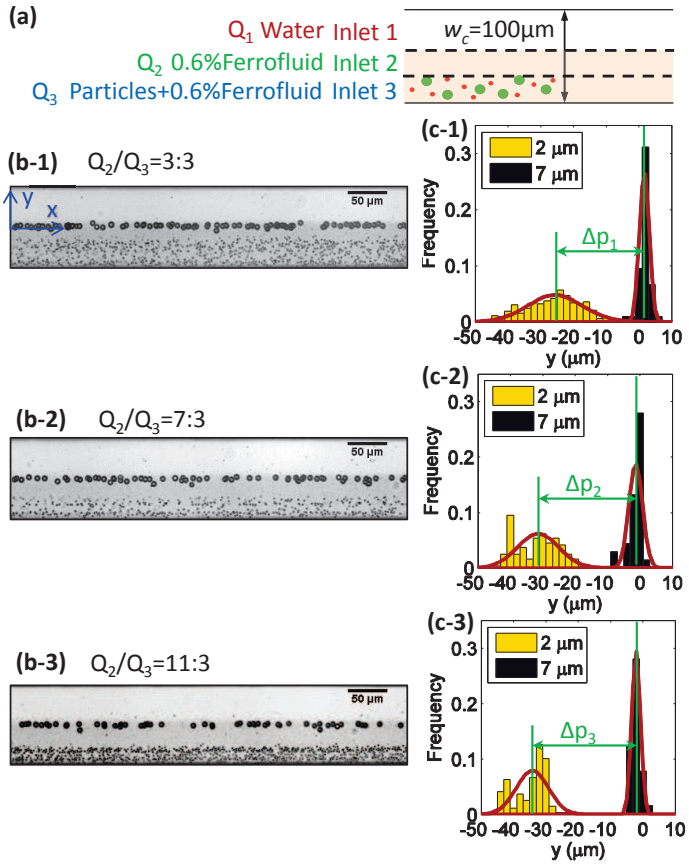

Figure 8. Separation of microparticles of different sizes. (a) Configuration for inlet solutions of the microfluidic channel; (b-1) to (b-3) are the stack images at the outlet of three different flow rate ratios; (c-1) to (c-3) are the Gussian distribution of 7 μm and 2 μm particles corresponding to (b-1) to (b-3), respectively; Δp is the peak distance between 7 μm and 2 μm particles. For each group, the width of the microfluidic channel was w_c = 100 μm; the concentration of ferrofluid was 0.6% (v/v); Q_1 was set at 3.5 μL/min, and $Q_2 + Q_3$ was kept at 4.0 μL/min.

Q_3, respectively. By the end of the fluidic channel, the larger particles were focused to the water-ferrofluid interface, while the smaller particles remained near their original entry positions. Therefore, complete separation could be achieved, as in Figs. 8 (b-1) to (b-3).

To study the effect of flow rate ratio on separation performance, Q_1 was set at 3.5 μL/min and the total flow rate of Q_2 and Q_3 was kept at 4.0 μL/min. It was clear that, when the flow rate ratio of Q_2/Q_3 increased, the distance between the 2 μm and 7 μm particles became larger. The Gussian distributions of the y locations of the particles at the outlet

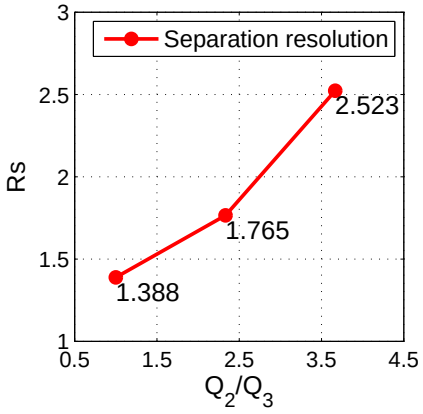

Figure 9. Separation resolution corresponding to Figs. 8 (b-1), (b-2), and (b-3), respectively.

are plotted in Figs. 8 (c-1) to (c-3). The peak distance of the three flow rate ratios had the relationship of $\Delta p_3 > \Delta p_2 > \Delta p_1$, which suggested better separation performance with a larger flow rate ratio of Q_2/Q_3. As noted by other researchers, the separation distance between the peak positions alone is not sufficient to characterize the separation performance [49]. To better quantify the separation performance, the parameter of separation resolution, R_s, was determined in accordance with previous studies [49],

$$R_s = \frac{p_l - p_s}{2(d_l + d_s)}, \tag{16}$$

where p_l and p_s are the peak positions of 7 μm (larger) and 2 μm (smaller) particles respectively, and d_l and d_s are their respective standard deviations.

Fig. 9 shows the separation resolution under the flow rate ratio of Q_2/Q_3, at 3:3, 7:3, and 11:3, respectively. When the flow rate ratio of Q_2/Q_3 was 11:3, the separation resolution had the largest value of 2.523, suggesting the best separation performance. This result can be explained as follows. First, a larger flow rate ratio made the initial y location of both 7 μm and 2 μm particles small enough. Second, the large particles moved fast enough to reach the interface with the effect of magnetic force. Third, the 2 μm particles had almost no vertical deflection, which was identical to the previous experimental observation.

Therefore, when both particles moved to the outlet, the 7 μm particles reached the interface, while the 2 μm particles remained at their original y locations. Thus, this method presents a simple way to separate particles by using multiphase ferrofluid flows.

5. CONCLUSIONS

This study demonstrates a simple and low-cost method for separating particles in ferrofluid by combining the multiphase laminar fluid interface and microscale magnets. The microfluidic devices integrated the NdFeB-PDMS microscale magnet next to the microfluidic channels, with a distance of tens of micrometers. The induced magnetic field gradients resulted in strong forces that could deflect magnetic particles and focus them at the interface between the water and ferrofluid. Systematic experiments were conducted to study the effects of concentrations of ferrofluid, the gap distance and the width of the fluidic channel on the focusing performance of particles. This investigation led to the following conclusions. First, when the concentration of ferrofluid increased, larger deflections of the particles were observed due to the increasing magnetic susceptibility and stronger magnetic forces. Second, a smaller gap distance between the microscale magnet and the microfluidic channel generated higher magnetic field gradients, thereby providing a better focusing performance. Third, a small channel width worked better for particle focusing. The proposed technique is simple and offers several advantages, including a smaller footprint due to the integrated microscale magnets, accurate positioning of the interface and thus precise focusing, as well as faster moving speeds of the focused particles. The principle of focusing particles to a fluid interface can be further extended to multiple fluid interfaces for complete separation of particles of different sizes. Our novel microdevice provides a simple and efficient method for the separation of micro-particles and biological cells, and will benefit practical microfluidic platforms concerning diamagnetic particles/cells.

REFERENCES

[1] J. Nilsson, M. Evander, B. Hammarstrom, and T. Laurell. Review of cell and particle trapping in microfluidic systems. *Analytica Chimica Acta*, 649(2):141 – 157, 2009.

[2] K. Pachmann, O. Camara, A. Kavallaris, S. Krauspe, N. Malarski, M. Gajda, T. Kroll, C. JÃűrke, U. Hammer, A. Altendorf-Hofmann, C. Rabenstein, U. Pachmann, I. Runnebaum, and K. HÃűffken. Monitoring the response of circulating epithelial tumor cells to adjuvant chemotherapy in breast cancer allows detection of patients at risk of early relapse. *Journal of Clinical Oncology*, 26(8):1208–1215, 2008.

[3] A. Valero, F. Merino, F. Wolbers, R. Luttge, I. Vermes, H. Andersson, and A. Van Den Berg. Apoptotic cell death dynamics of hl60 cells studied using a microfluidic cell trap device. *Lab on a Chip - Miniaturisation for Chemistry and Biology*, 5(1):49–55, 2005.

[4] Siyang Zheng, Henry Lin, Jing-Quan Liu, Marija Balic, Ram Datar, Richard J. Cote, and Yu-Chong Tai. Membrane microfilter device for selective capture, electrolysis and genomic analysis of human circulating tumor cells. *Journal of Chromatography A*, 1162(2):154 – 161, 2007.

[5] M. K. Tan, J. R. Friend, and L. Y. Yeo. Microparticle collection and concentration via a miniature surface acoustic wave device. *Lab Chip*, 7:618–625, 2007.

[6] W.-H. Tan and S. Takeuchi. Dynamic microarray system with gentle retrieval mechanism for cell-encapsulating hydrogel beads. *Lab on a Chip - Miniaturisation for Chemistry and Biology*, 8(2):259–266, 2008.

[7] H.A. Pohl. The motion and precipitation of suspensoids in divergent electric fields. *Journal of Applied Physics*, 22(7):869–871, 1951.

[8] T. Mueller, A. Gerardino, T. Schnelle, S.G. Shirley, F. Bordoni, G. De Gasperis, R. Leoni, and G. Fuhr. Trapping of micrometre and sub-micrometre particles by high-frequency electric fields and hydrodynamic forces. *Journal of Physics D: Applied Physics*, 29(2):340–349, 1996.

[9] K.V.I.S. Kaler and T.B. Jones. Dielectrophoretic spectra of single cells determined by feedback-controlled levitation. *Biophysical Journal*, 57(2 I):173–182, 1990.

[10] J.E. Molloy and M.J. Padgett. Lights, action: Optical tweezers. *Contemporary Physics*, 43(4):241–258, 2002.

[11] J.R. Moffitt, Y.R. Chemla, S.B. Smith, and C. Bustamante. Recent advances in optical tweezers. *Annual Review of Biochemistry*, 77:205–228, 2008.

[12] A. Ashkin. Acceleration and trapping of particles by radiation pressure. *Physical Review Letters*, 24(4):156–159, 1970.

[13] J.R. Kovac and J. Voldman. Intuitive, image-based cell sorting using optofluidic cell sorting. *Analytical Chemistry*, 79(24):9321–9330, 2007.

[14] A.N. Grigorenko, N.W. Roberts, M.R. Dickinson, and Y. Zhang. Nanometric optical tweezers based on nanostructured substrates. *Nature Photonics*, 2(6):365–370, 2008.

[15] M.A.M. Gijs. Magnetic bead handling on-chip: New opportunities for analytical applications. *Microfluidics and Nanofluidics*, 1(1):22–40, 2004.

[16] Nicole Pamme. Magnetism and microfluidics. *Lab. Chip*, 6:24–38, 2006.

[17] T. Lund-Olesen, H. Bruus, and M.F. Hansen. Quantitative characterization of magnetic separators: Comparison of systems with and without integrated microfluidic mixers. *Biomedical Microdevices*, 9(2):195–205, 2007.

[18] A. Winkleman, K.L. Gudiksen, D. Ryan, G.M. Whitesides, D. Greenfield, and M. Prentiss. A magnetic trap for living cells suspended in a paramagnetic buffer. *Applied Physics Letters*, 85(12):2411–2413, 2004.

[19] L.Y. Yeo and J.R. Friend. Ultrafast microfluidics using surface acoustic waves. *Biomicrofluidics*, 3(1):012002, 2009.

[20] J. Friend and L.Y. Yeo. Microscale acoustofluidics: Microfluidics driven via acoustics and ultrasonics. *Rev. Mod. Phys.*, 83(2):647–704, 2011.

[21] T. Zhu, F. Marrero, and L. Mao. Continuous separation of non-magnetic particles through negative magnetophoresis inside ferrofluids. In *2010 IEEE 5th International Conference on Nano/Micro Engineered and Molecular Systems*, pages 1006–1011, 2010.

[22] N.-T. Nguyen. Micro-magnetofluidics: Interactions between magnetism and fluid flow on the microscale. *Microfluidics and Nanofluidics*, 12(1-4):1–16, 2012.

[23] Nicole Pamme and Andreas Manz. On-chip free-flow magnetophoresis: Continuous flow separation of magnetic particles and agglomerates. *Analytical Chemistry*, 76(24):7250–7256, 2004.

[24] Jonathan D. Adams, Patrick Thevoz, Henrik Bruus, and H. Tom Soh. Integrated acoustic and magnetic separation in microfluidic channels. *Applied Physics Letters*, 95(25), 2009.

[25] Brian D. Plouffe, Laura H. Lewis, and Shashi K. Murthy. Computational design optimization for microfluidic magnetophoresis. *Biomicrofluidics*, 5(1), 2011.

[26] R. E. ROSENSWEIG. Fluidmagnetic buoyancy. *AIAA Journal*, 4(10):1751–1758, 1966.

[27] R E Rosensweig. Magnetic fluids. *Annual Review of Fluid Mechanics*, 19:437–461, 1987.

[28] Ayse R. Kose, Birgit Fischer, Leidong Mao, and Hur Koser. Label-free cellular manipulation and sorting via biocompatible ferrofluids. *Proceedings of the National Academy of Sciences*, 106(51):21478–21483, 2009.

[29] Melissa D. Krebs, Randall M. Erb, Benjamin B. Yellen, Bappaditya Samanta, Avinash Bajaj, Vincent M. Rotello, and Eben Alsberg. Formation of ordered cellular structures in suspension via label-free negative magnetophoresis. *Nano Letters*, 9(5):1812–1817, 2009.

[30] L. Liang, J. Zhu, and X. Xuan. Three-dimensional diamagnetic particle deflection in ferrofluid microchannel flows. *Biomicrofluidics*, 5(3), 2011.

[31] T. Kulrattanarak, R.G.M van der Sman, C.G.P.H. SchroÃńn, and R.M. Boom. Classification and evaluation of microfluidic devices for continuous suspension fractionation. *Advances in Colloid and Interface Science*, 142(1âĂŞ2):53 – 66, 2008.

[32] Martin A. M. Gijs, FrÃľdÃľric Lacharme, and Ulrike Lehmann. Microfluidic applications of magnetic particles for biological analysis and catalysis. *Chemical Reviews*, 110(3):1518–1563, 2010.

[33] Litao Liang and Xiangchun Xuan. Diamagnetic particle focusing using ferromicrofluidics with a single magnet. *Microfluidics and Nanofluidics*, 13(4):637–643, 2012.

[34] James J. Wilbanks, Garrett Kiessling, Jian Zeng, Cheng Zhang, Tzuen-Rong Tzeng, and Xiangchun Xuan. Exploiting magnetic asymmetry to concentrate diamagnetic particles in ferrofluid microflows. *Journal of Applied Physics*, 115(4), 2014.

[35] Jian Zeng, Chen Chen, Pallavi Vedantam, Vincent Brown, Tzuen-Rong J Tzeng, and Xiangchun Xuan. Three-dimensional magnetic focusing of particles and cells in ferrofluid flow through a straight microchannel. *Journal of Micromechanics and Microengineering*, 22(10):105018, 2012.

[36] Jian Zeng, Chen Chen, Pallavi Vedantam, Tzuen-Rong Tzeng, and Xiangchun Xuan. Magnetic concentration of particles and cells in ferrofluid flow through a straight microchannel using attracting magnets. *Microfluidics and Nanofluidics*, 15(1):49–55, 2012.

[37] Litao Liang, Cheng Zhang, and Xiangchun Xuan. Enhanced separation of magnetic and diamagnetic particles in a dilute ferrofluid. *Applied Physics Letters*, 102(23), 2013.

[38] J.C. McDonald, D.C. Duffy, J.R. Anderson, D.T. Chiu, H. Wu, O.J.A. Schueller, and G.M. Whitesides. Fabrication of microfluidic systems in poly(dimethylsiloxane). *Electrophoresis*, 21(1):27–40, 2000.

[39] R. Zhou and C. Wang. Acoustic bubble enhanced pinched flow fractionation for microparticle separation. *Journal of Micromechanics and Microengineering*, 25(8), 2015.

[40] M.D. Abramoff, P.J. MagalhÃčes, and S.J. Ram. Image processing with imagej. *Biophotonics International*, 11(7):36–41, 2004.

[41] RandallM. Erb and BenjaminB. Yellen. Magnetic manipulation of colloidal particles. In J. Ping Liu, Eric Fullerton, Oliver Gutfleisch, and D.J. Sellmyer, editors, *Nanoscale Magnetic Materials and Applications*, pages 563–590. Springer US, 2009.

[42] Magalie Faivre, Renaud Gelszinnis, Jérôme Degouttes, Nicolas Terrier, Charlotte Rivière, Rosaria Ferrigno, and Anne-Laure Deman. Magnetophoretic manipulation in microsystem using carbonyl iron-polydimethylsiloxane microstructures. *Biomicrofluidics*, 8(5):054103, 2014.

[43] Xiaotao Han, Yang Feng, Quanliang Cao, and Liang Li. Three-dimensional analysis and enhancement of continuous magnetic separation of particles in microfluidics. *Microfluidics and Nanofluidics*, 18(5-6):1209–1220, 2015.

[44] Christina Cruickshank Miller. The stokes-einstein law for diffusion in solution. *Proceedings of the Royal Society of London. Series A, Containing Papers of a Mathematical and Physical Character*, 106(740):724–749, 1924.

[45] David Meeker. Finite element method magnetics. *FEMM*, 4:32, 2010.

[46] Xu Yu, Cong-Ying Wen, Zhi-Ling Zhang, and Dai-Wen Pang. Control of magnetic field distribution by using nickel powder@pdms pillars in microchannels. *RSC Adv.*, 4:17660–17666, 2014.

[47] Yolanda H. Tennico, Daniela Hutanu, Myra T. Koesdjojo, Cheryl Moody Bartel, and Vincent T. Remcho. On-chip aptamer-based sandwich assay for thrombin detection employing magnetic beads and quantum dots. *Analytical Chemistry*, 82(13):5591–5597, 2010.

[48] Nan Xia, TomP. Hunt, BrianT. Mayers, Eben Alsberg, GeorgeM. Whitesides, RobertM. Westervelt, and DonaldE. Ingber. Combined microfluidic-micromagnetic separation of living cells in continuous flow. *Biomedical Microdevices*, 8(4):299–308, 2006.

[49] Abhishek Jain and Jonathan D. Posner. Particle dispersion and separation resolution of pinched flow fractionation. *Anal. Chem.*, 80:1641–1648, 2008.

IV. FABRICATION AND INTEGRATION OF MICROSCALE PERMANENT MAGNETS FOR PARTICLE SEPARATION IN MICROFLUIDICS

Ran Zhou, Qingbo Yang, Feng Bai, James Werner, Honglan Shi, Yinfa Ma, Cheng Wang

Department of Mechanical & Aerospace Engineering

Department of Chemistry

Missouri University of Science and Technology

Rolla, Missouri 65409

Tel: (573) 341-4636, Fax: (573) 341-4607

Email: wancheng@mst.edu

ABSTRACT

Microfluidic magnetophoresis is an effective technique to separate magnetically labelled bio-conjugates in lab-on-a-chip applications. However, it is challenging and expensive to fabricate and integrate microscale permanent magnets into microfluidic devices with conventional methods that use thin-film deposition and lithography. Here, we propose and demonstrate a simple and low-cost technique to fabricate microscale permanent magnetic microstructures and integrate them into microfluidic devices. In this method, microstructure channels were fabricated next to a microfluidic channel, and were injected with a liquid mixture of neodymium (NdFeB) powders and Polydimethylsiloxane (PDMS). After the mixture was cured, the resulted solid NdFeB-PDMS microstructure was permanently magnetized to form microscale magnets. The microscale magnets generate strong magnetic forces capable of separating magnetic particles in microfluidic channels. Systematic experiments and numerical simulations were conducted to study the geometric effects of the microscale magnets. It was found that rectangular microscale magnets generate larger $(\mathbf{H} \cdot \nabla)\mathbf{H}$ which is proportional to magnetic force, and have a wider range of influence

than the semicircle or triangle magnets. For multiple connected rectangular microscale magnet, additional geometric parameters, including separation distance, hight and width of the individual elements further influence the particle separation, and were characterized experimentally. With an optimal size combination, complete separation of yeast cells and magnetic micro-particles of similar sizes (4 μm) was demonstrated with the multi-rectangular magnet microfluidic device. Numerical simulations were developed to predict particle trajectories in the fluidic channel, and agree well with the experimental data. Our approach demonstrates an efficient and simple method to separate magnetic particles by integrating standalone microscale permanent magnets into microfluidic devices.

1. INTRODUCTION

Many fields of biology and chemistry, such as high-resolution and single-cell studies, have benefited from the recent progress of lab-on-a-chip and microfluidic technology, because single cells can be retained at defined locations and subject to well controlled microenvironments for interrogation over extended period of time [1, 2, 3, 4]. Much research in recent years has focused on using hydrodynamic effects or externally applied field gradients, such as electrical, optical, acoustic and magnetic fields, to induce forces on cells to realize trapping, separation and focusing of cells [5]. However, the methods of utilizing hydrodynamic effects or electric, optical, acoustic fields often involve complex designs or strongly depend on the properties of the flow medium or the interaction between the fluid and fluidic channels [6, 7, 8, 9], so magnetofluidics has been favored over these methods in biological applications. Magnetic forces are unique in that they allow actions at a distance, providing the ability to control objects without contact [10]. For example, magnetic particles suspended in diamagnetic solutions are attracted by magnetic forces towards a magnet where the magnetic field is the highest [11]. Recently, labeling target

bioparticles with functionalized magnetic beads has been a major focus to selectively trap and continuously sort cells out of a heterogeneous mixture [7, 12, 13] due to the benefits of low cost, insensitivity to temperature or pH, and remote actuation without direct contact.

During the past decades, magnetic particles have become standard tools for the isolation of defined cell subsets in modern cell biology, immunology and clinical medicine [14, 15]. For example, immunomagnetic separation (IMS) is a standard laboratory technique for isolating cells, proteins, and nucleic acids. This technique uses superparamagnetic polystyrene microspheres that are coated with a specific ligand. When added to a heterogeneous target suspension, the microspheres bind to the desired target. Using a powerful magnet, the microsphere-target complex is then removed from the suspension [16]. Another design called quadrupole magnetic flow sorter (QMS), is a cell sorter with operation based on application of a high-gradient quadrupole magnetic field [17]. The magnetic force acting on magnetically labeled cells in this quadrupole field has a centrifugal character that allows a continuous cell-separation process. QMS has been used for isolation of cancer cells from patients with head and neck cancer [18, 19] and to separate islet cells for diabetes diagnosis research [20]. And also, Lund-Olesen et al. studied the hybridization of target DNA in solution with probe DNA on magnetic beads immobilized on the channel sidewalls in a magnetic bead separator [21].

Magnet-activated cell sorting (MACS) [22] is one of the simplest and most effective ways for magnetic particle separation. A fluidic device utilizes high-gradient magnetic cell separation columns to control the trajectory of magnetically labeled cells in a magnetic field that is generated by a strong external magnet. However, the labeling particles are usually so small that can only generate weak magnetic forces, so a very strong magnetic field is needed. Changing the shape and position of magnet surrounding the microfluidic channel can generate a strong magnetic field to realize separation[23]. Although the purity of the separated sample is high, the recovery rate is as low as 37% [24]. This is because it is difficult to control the magnetic beads at a certain location for recovery without specific

magnetic gradients. A major current method is to use Microelectromechanical Systems (MEMS) technology to generate a magnetic field gradient through the use of micro-coils and magnetic pillars [25]. Although these platforms can easily manipulate the magnetic beads in batches, they do not provide a continuous separation, and the fabrication processes are expensive and complex.

It is highly desirable to have microfluidic devices with simple fabrication procedures while achieving the purposes of magnetic separation of particles/cells. In this paper, we propose a miniaturized and integrated microfluidic device that can pull magnetic particles from one laminar flow path to another by applying magnetic force, and thus selectively remove them from flowing fluids. To accomplish this, high-gradient microscale magnet was fabricated and integrated at one side of a microfluidic channel by a simple single-layer and single-mask microsolidics fabrication technique. The microscale magnet was fabricated by injecting and curing a mixture of neodymium (NdFeB) powder in a structural channels, and subsequent permanent magnetization. This study further investigates the effect of the microscale magnet shape, and geometry designs of multi-rectangular magnet on the separation performance. A numerical method is also presented for predicting the particle separation and shows good agreement with experimental measurements. To demonstrate the application of the magnetofluidics system, we separated a mixture of yeast strain *Saccharomyces cerevisiae* – a commonly used unicellular eukaryotic model, and magnetic micro-particles of similar diameters.

2. CONCEPT AND THEORY

2.1. Concept of Microdevices with Microscale Magnet. Fig. 1 (a) displays the picture of the microdevice that consists of a fluidic channel and microscale magnet. As can be seen in Fig. 1 (b), the microfluidic channel has three fluidic inlets and the dashed lines stand for the interfaces between the three different inlet flows. All experiments in our study were conducted at the condition of Q_1=Q_2=Q_3 to make sure each flow stand for

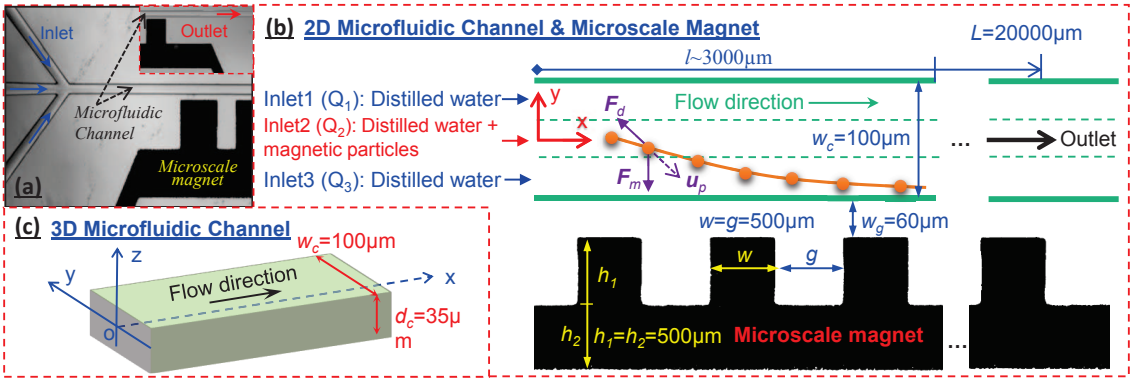

Figure 1. Overview of the separation microdevice with microscale magnet. (a) is a photograph of the fabricated microdevice. (b) is the 2D schematic of a part (l~3000μm) of the microfluidic channel and the microscale magnet, and (b) presents the deflection and forces acting on the magnetic particle. The microfluidic channel has a width of w_c=100μm and the smallest gap distance between the microscale magnet and the microfluidic channel is w_g=60μm. The typical size of the microscale magnet is w=g=h_1=h_2=500μm. w is the width of the microscale magnet; g is the gap distance between two microscale magnet; h_1 and h_2 are the heights of the microscale magnet and that of the connecting microbar, respectively; the whole length of the microfluidic channel and the microscale magnet are both L=20000μm. (c) is the 3D schematic of the microfluidic channel. The depth of the microfluidic channel is d_c=35μm; the depth of the microstructure channel (microscale magnet) is also equal to 35μm.

the same width of the microfluidic channel at inlet, so that it is easier to investigate the deflection of particles at the outlet. The role of the buffer flows is to focus the particles at the center of inlet and not too far from the microscale magnet in order for them to be pulled to the lower wall at the outlet. The closest distance from the microscale magnet to the microfluidic channel is 60 μm, ensuring that the local magnetic field gradients are strong enough to cause the deflection of magnetic particles. While the gap distance is one of the factors affecting magnetic separation, the gap distance was kept fixed at 60 microns in this study. This is because the effect of the gap distance w_g has been relatively well understood from previous studies in the literature [26], and the results suggest that a closer distance of the magnetic microstructure from the microfluidic channel can generate larger magnetic forces. In this study, w_g = 60 μm was the closest distance we could achieve with a low-cost manufacturing technique [27]. As shown in Fig. 1 (b), a magnetic particle

exposed to a magnetic field experiences a magnetic force, $\mathbf{F}_m$ [10]. The hydrodynamic drag force $\mathbf{F}_d$ due to the surrounding fluid is another important force acting on the particles. The gravity can be neglected due to the small velocity in the z direction, and will be discussed in section 2.2.3. Therefore, the magnetic force $\mathbf{F}_m$ and hydrodynamic drag force $\mathbf{F}_d$, are the main forces to determine the movement of the magnetic particle. Fig. 1 (c) presents the 3D schematic of the microfluidic channel. The depths of the microfluidic channel and the microstructure channel (microscale magnet) are both d_c = 35 μm

In this study, we mainly discuss the effect of the geometry of the microscale magnet on the movement of magnetic particles and separation performance. First, three representative shapes, *rectangular*, *semicircle* and *triangle* were chosen to study how the shape of a single microstructure influence the trajectories of magnetic particles, as shown in Fig. 3. In prior works in the literature [26, 28], *soft* microscale magnetic structures of *rectangular*, *semicircle* and *triangle* shapes have been used to generate magnetic fields to pull magnetic particles to the lower wall of the microfluidic channel. However, microscale permanent magnets might behave differently, and the effect of the shape needs further investigation. As will be seen in section 5.1, rectangular shape leads to large field gradients, different from the findings in earlier studies with soft magnetic structures [26, 28]. Second, multiple connected rectangular microscale magnet were designed to have different geometric combination of width w, height h and gap distance g, to study these geometric effects on separation performance in microfluidic channels of length L = 20000 μm. Finally, yeast cells ($D \approx 4$ μm) and 4-μm-diameter magnetic particles were completely separated by using the microscale magnet of the most optimized geometric combination.

2.2. Force Analysis of Magnetic Particles.

2.2.1. Magnetic force. In the presence of a magnetic field gradient, the magnetic particles experience a magnetic force, which can be modeled using a dipole moment approach by replacing the magnetized particle by an “equivalent" point dipole [29, 30]. The

magnetic force on the particle suspended in nonmagnetic fluids is given by,

$$\mathbf{F}_m = \mu_0(\mathbf{m}_p \cdot \nabla)\mathbf{H}, \tag{1}$$

where $\mu_0 = 4\pi \times 10^{-7}$ H/m is magnetic permeability of free space; $\mathbf{m}_p$ is the dipole moment of the particle; $\mathbf{H}$ is the applied magnetic field intensity at the center of the particle, where the equivalent point dipole is located. The dipole approximation has been used for decades to compute the force on micro magnetic particles. The validation of this approximation has recently been confirmed via particle trajectory measurements in a microfluidic system [31]. The dipole moment of the particle is

$$\mathbf{m}_p = \mathbf{M}_p V_p, \tag{2}$$

where $\mathbf{M}_p$ is the field-dependent particle magnetization; V_p is the volume of the particle. When the particle is saturated, $\mathbf{M}_p$=$\mathbf{M}_s$. However, both conditions of saturation and below saturation must be accounted for by expressing magnetization as

$$\mathbf{M}_p = f(H)\mathbf{H}, \tag{3}$$

where

$$f(H) = \begin{cases} \dfrac{3\chi_p}{\chi_p + 3}, & H < \dfrac{\chi_p + 3}{3\chi_p} M_s \\ \dfrac{M_s}{H}, & H \geq \dfrac{\chi_p + 3}{3\chi_p} M_s \end{cases}, \tag{4}$$

$H = |\mathbf{H}|$; χ_p is the magnetic volume susceptibility $\chi_p \approx 0.2$ [32] for the magnetic particles used in our study. The applied magnetic field intensity at the center of the particle in the microfluidic channel caused by microscale magnet is $H < 1.25 \times 10^4$ A/m in our study. The magnetization of pure Fe_3O_4 material is $M_s = 4.78 \times 10^5$ A/m [29], so $f(H) = \dfrac{3\chi_p}{\chi_p + 3}$ according to Eq. (4). Therefore, the magnetic force on the dipole, and hence on the particle,

is given by

$$\mathbf{F}_m = \mu_0 V_p \frac{3\chi_p}{\chi_p + 3}(\mathbf{H} \cdot \nabla)\mathbf{H}. \tag{5}$$

2.2.2. Fluidic force. In addition to the magnetic force $\mathbf{F}_m$, there exists a viscous drag force $\mathbf{F}_d$ acting on the particle in the direction opposite to the particle motion [33]. The drag force in low Reynolds number microfluidic systems is predicted using Stokes' law [6],

$$\mathbf{F}_d = 6\pi\eta r(\mathbf{u}_f - \mathbf{u}_p) f_D, \tag{6}$$

where η and $\mathbf{u}_f$ are the dynamic viscosity and velocity of the fluid, respectively; $\mathbf{u}_p$ is the particle velocity; r is the radius of the magnetic particle; f_D is the hydrodynamic drag force coefficient. f_D is the drag coefficient for reflecting the wall effect and is expressed as [8],

$$f_D = \left[1 - \frac{9}{16}\left(\frac{r}{r+z'}\right) + \frac{1}{8}\left(\frac{r}{r+z'}\right)^3 - \frac{45}{256}\left(\frac{r}{r+z'}\right)^4 - \frac{1}{16}\left(\frac{r}{r+z'}\right)^5\right]^{-1}, \tag{7}$$

where z' is the distance between the bottom of the particle and the channel surface; r is the radius of the particle. If the particle is far from the wall, $f_D = 1$ and Eq. (6) reduces to the usual StokesâĂŹ drag formula, which strictly applies to a single isolated particle in an infinite uniform flow field. However, for most applications the flow field is not uniform but rather varies throughout the fluidic system (e.g., laminar flow through a microchannel). Nevertheless, the particle diameter is typically much smaller than the dimensions of the fluidic system, and thus the fluid velocity is relatively constant across the particle. Thus, we use Eq. (6) to estimate the viscous drag force on a particle at a given time by using the particle velocity at that time, and the fluid velocity at the position of the particle at that time.

For the velocity profile of laminar steady flows in rectangular channels, Purday [34] proposed a simple algebraic approximation instead of an infinite sum of Fourier series [35] for channel aspect ratio $\alpha = d_c/w_c \leq 0.5$ to avoid computational complexity, which is given

by

$$u(y,z) = u_m(\frac{m+1}{m})(\frac{n+1}{n})[1-(\frac{2y}{w_c})^m][1-(\frac{2z}{d_c})^n], \tag{8}$$

where u_m is the mean velocity in x direction. In our study, the depth of microchannel d_c=35 μm and the width of microfluidic channel w_c = 100 μm. Therefore, according to the coordinate in Fig. 1, the aspect ratio α satisfies the condition required by the approximate equation (Eq. 8). The value of m and n were solved by a finite element method by Natarajan and Lakshmanan [34], and $m = 1.7 + 0.5\alpha^{-1.4}$ and $2 + 0.3(\alpha - \frac{1}{3})$ for the channel aspect ratio in our study.

2.2.3. Gravitational force. Previous studies have suggested that the gravity can have important roles in determining the particle motions during the separation process when the particles are heavier than the surrounding liquid [36, 37]. Taking into account of buoyancy, the effective gravitational force $\mathbf{F}_g$ can be expressed as

$$\mathbf{F}_g = V_p(\rho_p - \rho_f)\mathbf{g}, \tag{9}$$

where ρ_p and ρ_f are the densities of the particle and fluid respectively; $\mathbf{g}$ is the acceleration due to gravity. In our study, the effect of gravity can be safely neglected because the particle velocity in the z direction due to $\mathbf{F}_g$ is much smaller compared to the velocities in the x and y direction. Specifically, u_{px} is estimated to be the average flow velocity in channel, and u_{py} is the average velocity due to magnetic force. u_{pz} is calculated by balancing the viscous drag to gravitational force.The estimation of the velocity scales suggests that the velocity in the z direction is at least 200 times smaller than those in the x and y direction, so the particle velocity in the z direction caused by gravity is negligible.

3. NUMERICAL SIMULATION

We determined the trajectory of the magnetic particles using numerical simulations to validate the above theoretical analysis. A custom-written Matlab program was employed to compute the particle position based by Newton's second law. The magnetic force was computed based on the magnetic field simulated by a FEM software package COMSOL Multiphysics.

The magnetic field in COMSOL is simulated by solving the Laplace equation of the magnetic potential. The mesh distribution is non-uniform in the whole computational domain, and the mesh is refined near the magnets to obtain accurate results of the gradient and the strength of magnetic field in the microdevice. The quadratic Lagrange finite element in cubic shape is selected, and the total number of mesh is about 900,000. The computation of this model is time consuming and costs over 20 mins to obtain the steady state solution even by choosing the multigrid method to pre-smooth the mesh. If the Navier-Stokes equation is also simulated, the mesh in the microchannel should be refined properly in order to obtain an accurate flow fields. To do this, a huge model including over 1,200,000 meshes has to be generated, which will require a larger amount of memory of the computer. Computationally, it is too expensive to solve a fully coupled model in this geometry due to the limited computing resources available to us. To avoid this problem, the magnetic field was extracted and imported into Matlab to calculate particle trajectories by a custom-written code. This method has been proved to be effective and accurate enough from the comparisons between the experimental and simulated results.

Since the effect of gravity can be safely neglected, it is reasonably accurate to assume the particle will stay in the same z plane during the process of flowing through the fluid channel. As a result, 2-D simulations of particle trajectories can be used as long as the particle's location in the z direction is known. This means that the variable z in Eq. (8)

can be regarded as a constant for each particle. The results of the simulated trajectories presented in Section 5.1 shows a good agreement with the experiment data, and thus are supportive of the theoretical analysis and 2-D simplification.

3.1. Magnetic Field. The geometry and size of the magnets were constructed according to the actual fabricated microdevices. The coercivity H_c of the microscale magnet was 94000 A/m for the NdFeB-PDMS composite used in our study. The value of H_c was experimentally determined from the measurement of large scale cylindrical composites by fitting the measurements with analytical solutions [38]. The simulation domain was set as at least five times of the microdevice size. The magnetic flux density H_x and H_y at various z planes were exported and were later imported to the custom Matlab program to calculate the magnetic force through Eq. (5).

3.2. Particle Trajectory. The initial particle positions in the simulations have the same z coordinate as those in the experiments. In the experimental measurements, particles near the centerline of microfluidic channel were selected, and all sample particles were almost on the same z plane to ensure consistent and meaningful comparisons. As mentioned above, the movement of the microparticles can be regarded as steady motion for each instantaneous time period, so the instantaneous position of a particle, $\mathbf{r}_p$, are then computed over time by numerical integration $\mathbf{r}_p = \mathbf{r}_0 + \int_0^t \mathbf{v}_p dt'$, where $\mathbf{r}_0$ is the initial location of the particle, $\mathbf{v}_p$ is the particle velocity at each time instance, and t is time.

4. MATERIALS AND METHODS

4.1. Microfluidic Device Fabrication. Fig. 2 describes the main fabrication steps of the microfluidic device. The microfluidic device was fabricated in PDMS following by soft lithography technique [39]. The master molds were manufactured in a dry film photoresist (MM540, 35 μm thick, DuPont) by lithographic patterning method [40]. A layer of dry film resist was first laminated onto a copper plate using a thermal laminator. After ultra-violet (UV) exposure through a transparency photo mask (10,000 dpi, CAD/Art

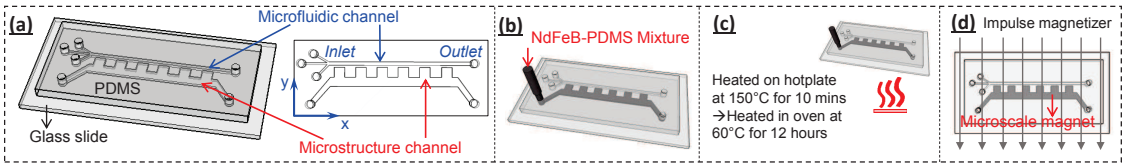

Figure 2. Fabrication steps of the microfluidic device. (a) The PDMS microdevice consists of the microfluidic channel and the microstructure channel. The microfluidic channel has three inlets and one outlet; the microstructure channel has one inlet and one outlet. (b) Injection of NdFeB-PDMS mixture. (c) Curring of NdFeB-PDMS mixture on the hotplate and in the oven. (d) Magnetization of the cured NdFeB-PDMS mixture to form microscale permanent magnet.

Services Inc), the exposed dry film was developed, rinsed and dried to obtain the master mold. PDMS base and initiator were throughly mixed, degassed, and then cast on the master. After curing, the PDMS replica was peeled off from the master, cut and punched, and then bonded with a flat glass slide after corona surface treatment. Using this method, microfluidic and microstructure channels with rectangular cross sectional shape were fabricated as displayed in Fig. 2(a). Next, NdFeB powders (MQFP-B-20076, Molycorp Magnequench) were thoroughly mixed with a pre-mixed liquid PDMS at a ratio of NdFeB/PDMS=2:1 (w/w). The mixture of the NdFeB powders and PDMS was degassed, and subsequently injected into the microstructure channel with a syringe pump shown in Fig. 2(b). Immediately after filling the NdFeB-PDMS mixture, the microdevice was heated on a hotplate at 150°C for 10 minutes to cure the mixture, as in Fig. 2(c). The fast curing process is critical to prevent the agglomeration and sedimentation of the neodymium powders. The microfluidic device was heated in an oven at 60 °C for another 12 hours to ensure complete curing and strong bonding. In Fig. 2(d), after the mixture was cured, the resulted solid NdFeB-PDMS microstructure was permanently magnetized by an impulse magnetizer (IM 10, ASC Scientific).

4.2. Materials. The magnetic particles in this study are commercially available magnetite-doped un-cross-linked polystyrene microspheres (Micromod GmbH, Germany). The mean diameter of the magnetic particles is $D = 7$ μm (coefficient of variation < 5%) and its density is 1.1 g/mL. These particles are coated with surface carboxylic groups (COOH). The original solution of 7 μm magnetic particles (5% w/w) were diluted 1000 times with distilled water, so the final particle concentration was 2.5×10^5/mL. Inlets 1 and 3 were injected with distilled water to work as buffer, and inlet 2 was injected with the distilled water containing magnetic particles to work as the particle flow. To prevent particle from adhering to the microfluidic channel and agglomeration, surfactant Tween 20 was added to all fluids.

4.3. Preparation of Yeast Cells. Culture flasks were pre-seeded with 0.1% (w/w) of a commercial yeast preparation (*Saccharomyces cerevisiae*, Rapid Rise Yeast, Fleischmann's, Oakville, ON, Canada) to provide an initial cell concentration of approximately 1×10^9 cells/mL. The *S. cerevisiae* yeast strain was quickly activated in a high D-glucose medium (10 g/L) at 30 °C for 60 minutes to initiate an exponential growth phase. The optical density (OD) was determined by measuring the absorbance at λ = 600 nm and normalization was conducted for each batch of the yeast cells. Centrifugation was applied once cell numbers come to a standardized level ($OD_{600} = 2.8 \pm 0.1$) and washed twice with a 0.1 M phosphate buffer solution (PBS). Cells were finally re-suspended and aspirated in de-ionized (DI) water to mix with magnetic particles for microfluidic chip injection.

4.4. Experimental Set-up. To record the trajectories of the magnetic particles during the experimental process, the microfluidic devices were mounted on an inverted microscope stage (IX73, Olympus). A high-speed camera (Phantom Miro M310, Vision Research) was used to capture videos. The microfluidic devices were illuminated by a fiber optic light for transmission bright-field imaging. We used three syringe pumps (NE-300, New Era and KDS 200, KDS Scientific) to control the flow rate of each inlet, and three small syringes (1 mL) to minimize the effect of the motor's step motion to maintain good stability

of the flow. ImageJ [41] was used to extract the particle position from the experimental videos, and then the z position of magnetic particles can be determined by our custom written code.

5. RESULTS AND DISCUSSION

The magnetized NdFeB-PDMS microstructure functions as permanent magnets, exerts attractive forces on the magnetic particles, and induces vertical deflection of the particles. The magnetic forces depend on the magnetic field and its gradient based on Eq. (5). The shape of NdFeB-PDMS microscale magnet can influence the magnetic field and its gradient, and was investigated in this study with systematic experiments and numerical simulations. This section first presents how a single microscale magnet of three shape styles – *rectangular*, *semicircle* and *triangle*, affect the trajectories of the magnetic particles. Then, multiple connected rectangular microscale magnet with different size combination are discussed to explore their effect on the vertical deflection of the magnetic particles. Finally, the microfluidic device with multiple connected rectangular microscale magnet of the most optimized size combination was chosen to achieve complete separation of magnetic particles and yeast cells.

5.1. Effect of Microscale Magnet Shape. The effect of a single NdFeB-PDMS microscale magnet with different shapes on the trajectories of magnetic particles is first explored in this section. As shown in Fig. 3 (a-1), (a-2) and (a-3), three representative shapes of *rectangular*, *semicircle* and *triangle* were chosen because the microscale magnet of these three shapes can generate strong magnetic fields and gradients to trap magnetic particles [26, 28]. Each microscale magnet was fabricated with the same base length of w=1000μm and height of h=500μm, and positioned at w_g=60μm away from the microfluidic channel, as mentioned in Fig. 1 (b). The experimental and simulated particle trajectories with these three microscale magnets were compared in Fig. 3 (b-1) – (b-3). From the comparison, the experimental trajectories were in good agreement with the simulations.

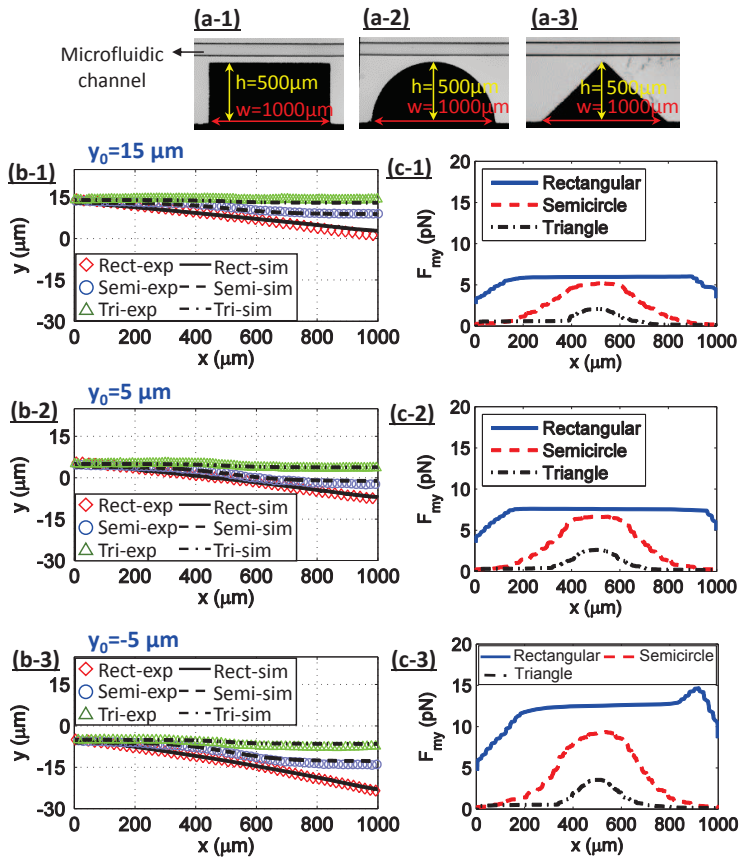

Figure 3. Effect of microscale magnet shape. (a-1)–(a-3) are the micro-photographs of three different microscale magnet: rectangular, semicircle and isosceles-triangle magnets. The width w and height h of each magnet are 1000μm and 500μm, respectively. (b-1)–(b-3) compare the experimental (symbols) and simulated particle trajectories (lines) under the rectangular, semicircle and isosceles triangle magnet with initial y positions y_0=15μm, y_0=5μm and y_0=-5μm respectively; the coordinate is based on Fig. 1 (b). (c-1)–(c-3) are the magnetic forces F_{my} acting on the particle during the transport process corresponding to (b-1)–(b-3).

The inlet flow rate was Q_1=Q_2=Q_3=0.3μL/min, as shown in Fig. 1 (b), so the particles were distributed at random positions in the central part of the microfluidic channel. To make a full investigation of the three microscale magnets, the trajectories of particles at different initial position of y_0= 15 μm (Fig. 3 (b-1)), y_0= 5 μm (Fig. 3 (b-2)) and y_0= -5 μm (Fig. 3 (b-3)) were chosen. Among the three shapes, the rectangular magnet resulted in the largest vertical deflection for each initial position. This difference in deflection can be understood

by the vertical magnetic velocity u_{my},

$$u_{my} = \frac{F_{my}}{6\pi\eta r f_D}, \tag{10}$$

where F_{my} is the magnetic force in the y direction. In Fig. 3 (c-1) – (c-3), the vertical magnetic force F_{my} from simulations are compared. It is evident that F_{my} from the rectangular magnet had a larger magnitude and a wider range of action on the particles. Accordingly, the magnetic particles were deflected towards the lower side of microfluidic channel faster with the rectangular magnet at each initial position y_0.

The contours indicating the magnetic field distribution are presented in Fig. 4 to better explain the effect of the geometrical shape. As can be seen in Fig. 4 (a-1) to (a-3) and (b-1) to (b-3), the magnetic field and its gradients in microfluidic channel caused by the rectangular magnet are larger and have a wider action range than those induced by semicircle or triangle magnet, indicating the reason that the magnetic particles deflect more in the y direction under the effect of rectangular magnet. Fig. 4 (c-1) to (c-3) show the connected-shape microscale magnets, their corresponding $(\mathbf{H}\cdot\nabla)\mathbf{H}_y$ are displayed in Fig. 4 (d-1) to (d-3). Similar to single microstructure, the connected rectangular magnet can generate a larger and wider magnetic field and gradients. The negative $(\mathbf{H}\cdot\nabla)\mathbf{H}_y$ in Fig. 4 (b-1) to (b-3) and Fig. 4 (d-1) to (d-3) illustrates the direction of $\mathbf{F}_{my}$ according to the coordinates in Fig. 1(b) and is consistent with the deflection of particles. To quantitatively understand the reason of the superior performance of rectangular magnet, we define an equivalent magnetic force intensity $\widetilde{H}$ as

$$\widetilde{H} = \int_0^l \overline{|(\mathbf{H}\cdot\nabla)\mathbf{H}_y|}\,\mathrm{d}x, \tag{11}$$

where l=2000μm is the period length of the connected magnet, as shown in Fig. 4 (c-1) to (c-3); $\overline{|(\mathbf{H}\cdot\nabla)\mathbf{H}_y|}$ is the average value of $|(\mathbf{H}\cdot\nabla)\mathbf{H}_y|$ from $y=-50\mu$m to $y=50\mu$m (total width of the microfluidic channel) of the microfluidic channel at each x position from the

beginning to end of a 2000 μm period according to the coordinate in Fig. 1 (b). According to Eq. (5), $F_{my} \propto |(\mathbf{H} \cdot \nabla)\mathbf{H}_y|$, $\widetilde{H}$ can be interpreted as a measure of the average magnetic strength that causes vertical deflection of the particles through Eq. (11). In Fig. 4 (d-1) to (d-3), it is obvious that the equivalent $\widetilde{H} = 2.89 \times 10^8 (A^2/m^2)$ of connected rectangular magnet is also the largest, meaning the largest effect of the magnetic field on the deflection of the magnetic particles.

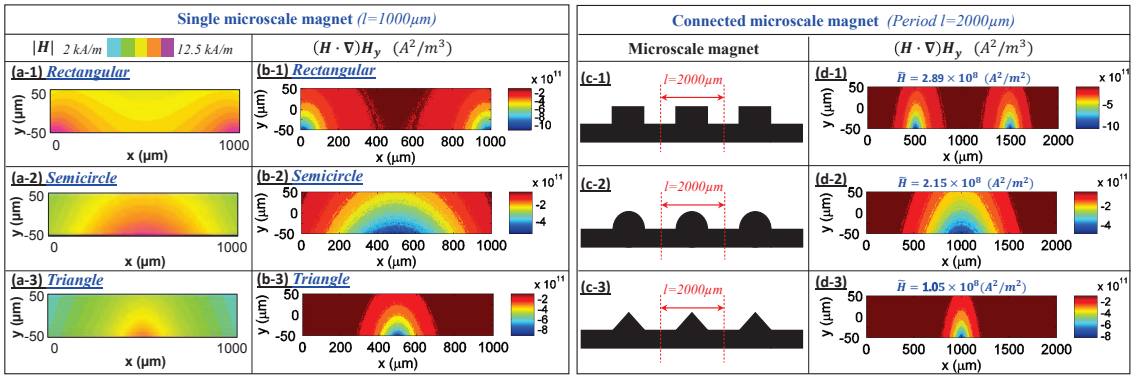

Figure 4. Magnetic field map in microfluidic channel generated by single and connected microscale magnet with different geometrical shapes. (a-1) to (a-3) are the magnitude contour of magnetic field intensity $|\mathbf{H}|$ corresponding to different shaped single microscale magnet in Fig.3 (a-1), (a-2) and (a-3), respectively. (b-1) to (b-3) are $(\mathbf{H} \cdot \nabla)\mathbf{H}_y$ contour corresponding to different shaped single microscale magnet in Fig.3 (a-1), (a-2) and (a-3), respectively. (c-1) to (c-3) are connected rectangular, connected semicircle, connected triangle microscale magnet. Each single microstructure has the same size with the corresponding single magnet in Fig.3 (a-1), (a-2) and (a-3), respectively. (d-1) to (d-3) are $(\mathbf{H} \cdot \nabla)\mathbf{H}_y$ contour corresponding to (c-1) to (c-3), respectively. $\widetilde{H}$ is equivalent magnetic intensity.

5.2. Effect of the Size Combination of Multi-rectangular Microscale Magnet.

It has been shown that rectangular microscale magnet can result in the largest y-direction displacement of particles. To further enhance the deflection, multiple rectangular microscale magnets were designed to test the practical use of our proposed devices. In this case, separation performance depends on several geometric parameters, including the rectangular width w, the gap distance g between each microscale magnet, and the height h of the microscale magnet, as shown in Fig. 1 (b). The combination of w, g and h, influences both the strength

and gradients of the magnetic field. In this section, these parameters, w, g and h of the microscale magnet were evaluated experimentally to determine an optimal combination to separate magnetic particles. To better study each parameter, the other two were kept fixed when one parameter was changed. The length of the multi-rectangular microscale magnet with each size combination was designed to be the same, and L=20000μm.

5.2.1. Effect of rectangular magnet width. The buffer flow and particle flow were injected into the microfluidic channel with the flow rate of Q_1=Q_2=Q_3 =2.0μL/min, as shown in Fig. 5 (a), so the magnetic particles occupy the central part of the channel at the inlet. The pre-focusing ensured all the particles to enter the region of strong and similar magnetic fields and gradients. To study the effect of rectangular magnet width w on deflecting the particles, the height h and gap distance g were kept the same as h=g=500μm. Three different microscale magnet widths of w=500μm, w=1000μm and w=250μm were designed and the corresponding micro-photographs were displayed in Fig. 5 (b-1)–(b-3). The corresponding distribution of the magnetic particles at the channel outlet can be seen in Fig. 5 (c-1)–(c-3). It is clear from Fig. 5 (c-1)–(c-3) that a larger percentage of particles were deflected towards the lower wall of w=500 μm microscale magnet than that of the other two cases. In order to quantitatively analyze the particle distribution, the bimodal Gaussian distribution of the experiment data were summarized in Fig. 5 (d-1)–(d-3). In statistics, a bimodal Gaussian distribution is a continuous probability distribution with two different modes, and best presents the two peaks observed in the experiments. The bimodal Gaussian distribution includes a group of particles that are attracted near the lower wall p_1, and a group of particles that are far away from the lower wall p_2. Comparing the three bimodal Gaussian distributions, the first peak location p_1 of w=500μm magnet is the highest and closest to the lower wall, suggesting that more magnetic particles were attracted to the lower wall of the microfluidic channel. On the other hand, the second peak location

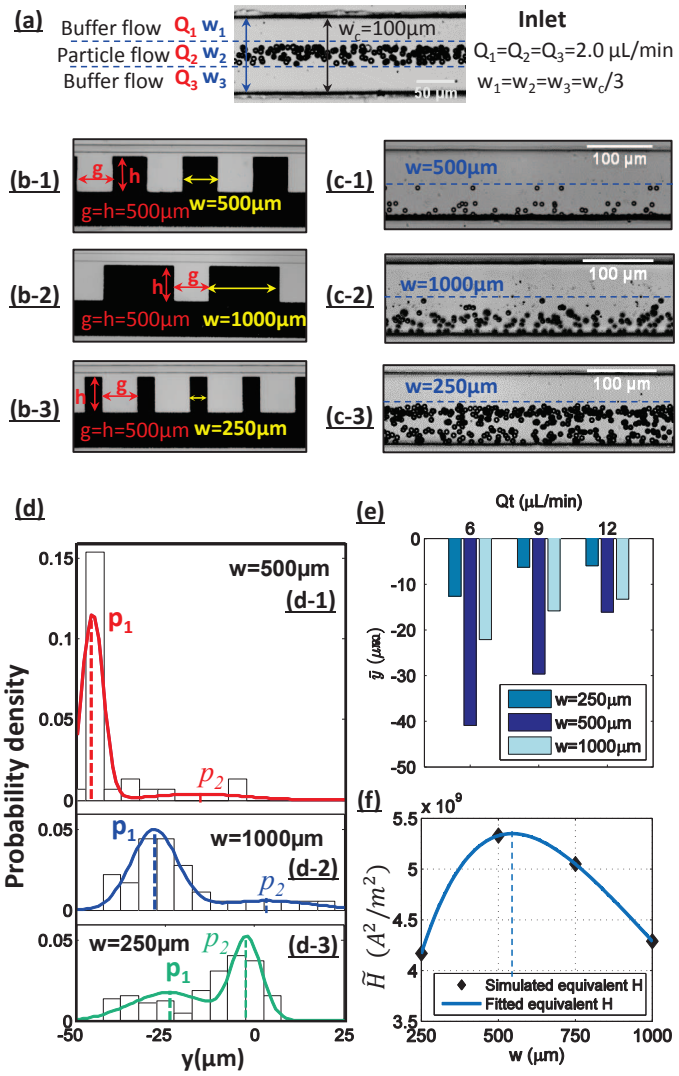

Figure 5. Effect of the width w of multi-rectangular microscale magnet on the vertical deflection of particles. (a) Particle distribution at the inlet of the microfluidic channel. The flow rate is Q_1=Q_2=Q_3=2.0μL/min. The width of particle flow and buffer flow is $w_1 \approx w_2 \approx w_3$ because of the equal flow rates. (b-1)–(b-3) are the micro-photographs of the microscale magnet with different widths: w=500μm, w=1000μm and w=250μm. The height h and gap distance g of each group are kept at h=g=500μm. (c-1)–(c-3) are corresponding distribution of magnetic particles at the outlet; (d-1)–(d-3) are the corresponding best-fit bimodal Gaussian distribution of the particles' y position of the experiment data. (e) is the experimental mean y position $\bar{y}$ of particles at the outlet at different total flow rates Q_t. (f) is the equivalent magnetic field intensity $\widetilde{H}$ in the microfluidic channel when varying the width of the microscale magnet. Symbols are $\widetilde{H}$ calculated from simulations, and the solid line is the best fitted polynomial line of $\widetilde{H}$.

p_2 of w=250μm magnet is the highest and located close to the central part of the channel, indicating that most magnetic particles stayed at their initial y position and experienced little vertical deflection from the inlet to the outlet.

As can be seen in Fig. 5 (e), for each total flow rates examined, the mean y position $\bar{y}$ at the outlet is the closest to the lower wall of the channel, with w=500μm. It can therefore be inferred that w=500μm magnet had a superior performance on particle deflection in y-direction. When increasing the total flow rate Q_t, the mean y location at the outlet moved farther away from the lower wall for each width, because the vertical deflection distance is the result of the competition of the vertical magnetic and viscous drag forces. With an increasing flow velocity and a larger drag force, the residence time, t_r, of the particle within the influence range of F_{my} becomes shorter. Despite the same magnetic force (the same vertical velocity), the vertical deflection becomes smaller because of the shorter residence time t_r.

The equivalent magnetic field intensity $\widetilde{H}$ induced by w=250μm, w=500μm, w=750μm and w=1000μm magnets was calculated from the simulations, and were presented in Fig. 5 (f). Here, $\widetilde{H}$ is derived from the total length of the microfluidic channel l=20000μm to reflect the separation performance of different magnet more accurately and fully. From the best fitted polynomial line of $\widetilde{H}$, it can be concluded that as the magnet width w increased from 250μm to 1000μm, $\widetilde{H}$ increased initially and began to decrease after reaching its peak at w close to 550 μm. The dependence of $\widetilde{H}$ on w explains the best separation at w = 500 μm in the experiment observations, and provides a practical guideline for design optimization purpose. Therefore, $\widetilde{H}$ will be used for understanding the effect of g and h in the following sections, 5.2.2 and 5.2.3 .

5.2.2. Effect of rectangular magnet gap distance. Similarly, the effect of the gap distance g between the connected magnets was studied in this section, while the width w and the height h of the microscale magnet were kept the same as 500μm. Fig. 6 (a-1)–(a-3) displays the micro-photographs of the three different microscale magnets with gap distances

of g=500μm, g=1000μm and g=250μm respectively. The corresponding distributions of magnetic particles at the outlet are shown in Fig. 6 (b-1)–(b-3). The inlet flow rate was set as Q_1=Q_2=Q_3=2.0μL/min. Comparing Fig. 6 (b-1)–(b-3), the gap distance of 500μm resulted in the largest vertical deflection and best separation of the particles. This trend was more evident in the bimodal Gaussian distribution plot, as in Fig. 6 (c-1)–(c-3). Although the first peak p_1 of the three gap distances were all close to the lower wall of the microfludic channel, p_1 of g=500μm magnet is much higher than the other two groups, meaning a better trapping performance on the magnetic particles.

With different total flow rate Q_t, Fig. 6 (d) shows that the mean y position $\bar{y}$ of particles at the outlet. At each Q_t, g=500μm magnet performed best on the vertical deflection of magnetic particles. However, when the total flow rate increased, the outlet $\bar{y}$ became farther from the lower wall for each gap distance group because of the shorter resident time t_r of magnetic force. Fig. 6 (e) demonstrates the reason of the different y location distribution under the effect of g=500μm, g=1000μm and g=250μm by using the equivalent magnetic force intensity $\widetilde{H}$ defined in Eq. (11). In Fig. 6 (e), a trend line was plotted for the $\widetilde{H}$ values by fitting numerical results of the g=250μm, g=500μm, g=750μm and g=1000μm magnets. It is seen from Eq. (5) that F_{my} increases first and then declines over the range between g=250μm and g=1000μm, with the peak position near $g \approx 550$ μm. Accordingly, it can be inferred from Eq. (10) that the vertical magnetic velocity u_{my} of the magnetic particles caused by the microscale magnet with g~550μm will be faster and will lead to a better separation performance.

5.2.3. Effect of rectangular magnet height. The effect of the height h is studied in this section. Fig. 7 (a-1)–(a-3) and (b-1)–(b-3) present the micro-photographs of the magnet with different heights and the corresponding particles y-distribution at the outlet of the microfluidic channel. The height varied from 1000μm, 500μm to 250μm. To keep the same condition, the width w and the gap distance g of the microscale magnet were set the same value of 500μm. Also, the flow rates of each inlet were the same and equal to

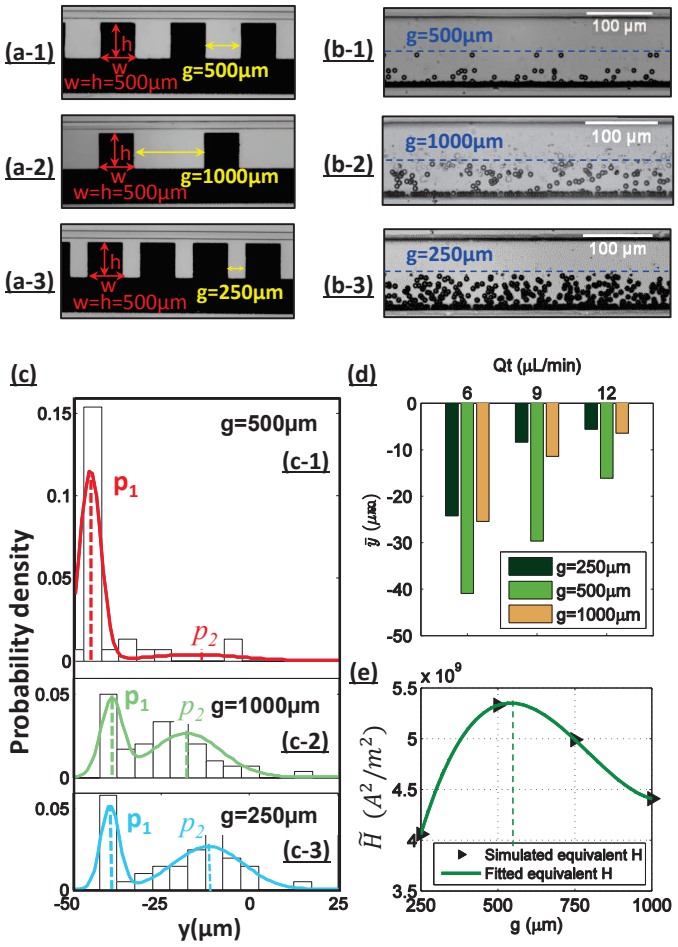

Figure 6. Effect of the gap distance g of multi-rectangular microscale magnet on the vertical deflection of particles. (a-1)–(a-3) are the micro-photographs of the microscale magnet with different gap distance: g=500μm, g=1000μm and g=250μm. The height h and width w of each group are kept at h=w=500μm. (b-1)–(b-3) are the corresponding distribution of magnetic particles at the outlet; (c-1)–(c-3) are the corresponding bimodal Gaussian distribution of the experiment data. (d) is the experimental mean y position $\bar{y}$ of particles at the outlet for different gap distances when varying total flow rate Q_t. (e) is equivalent magnetic force intensity $\widetilde{H}$ for different gap distances. Symbols are the simulated $\widetilde{H}$, and the solid line is the polynomial fitted line of the simulated results.

2.0μL/min to focus the magnetic particles at the central part of the channel at the inlet. As can be seen in Fig. 7 (b-1)–(b-3), most particles were deflected noticeably towards the lower wall when the height of the magnet 1000μm, while the particles vertical movement can be hardly observed at the height of 250μm. To clarify this trend, Fig. 7 (c-1)–(c-3) illustrate

that p_1 of h=1000μm magnet is the highest and closest to the lower wall, indicating that more magnetic particles were deflected towards the bottom part of the microfluidic channel.

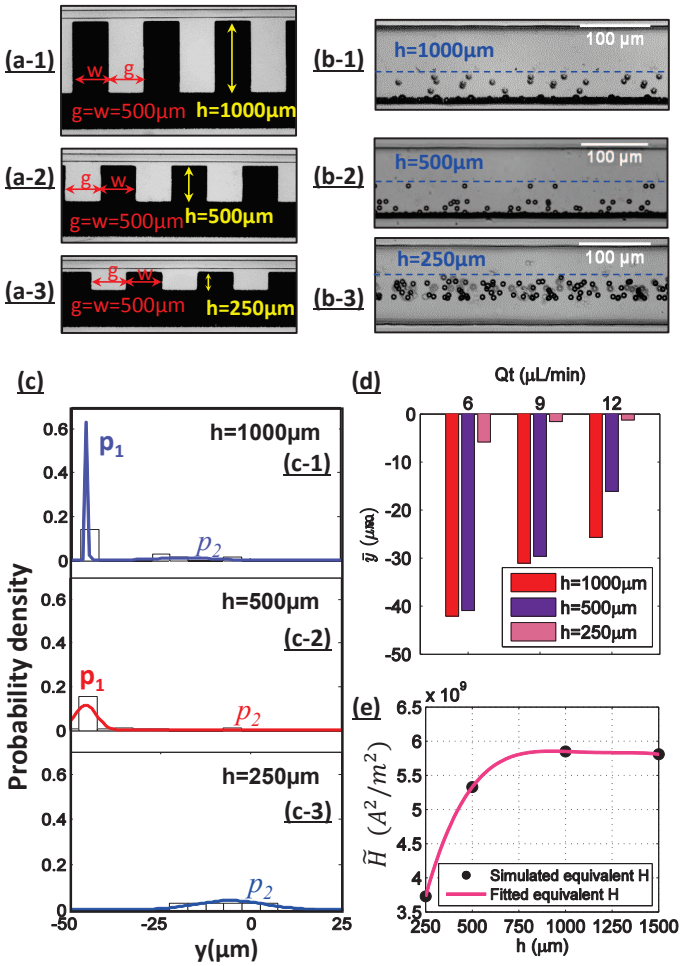

Figure 7. Effect of the height h of multi-rectangular microscale magnet on the vertical deflection of particles. (a-1)–(a-3) are the micro-photographies of the microscale magnet with different hight: h=1000μm, h=500μm and h=250μm. The width w and gap distance g of each group are kept at w=g=500μm. (b-1)–(b-3) are corresponding distribution of magnetic particles at outlet; (c-1)–(c-3) are corresponding bimodal Gaussian distribution of the experiment data. (d) is the experimental mean y position of particles at outlet with the effect of different-hight magnet when varying total flow rate Q_t. (e) is equivalent magnetic field intensity $\widetilde{H}$ in microfluidic channel when varying the hight of the microscale magnet. Symbol is the simulated $\widetilde{H}$ and the green line is the polynomial fitted line of the simulated results.

Fig. 7 (d) demonstrates that h=1000μm microscale magnet has a better separation performance to induce vertical deflection of the particles at each total flow rate Q_t. Similar to the previous discussions of the width and gap distance of the magnet, increasing total flow rate Q_t weakens vertical deflection of the particles due to shorter resident time t_r. As illustrated in Fig. 7 (e), when the height of the magnet increased, the equivalent magnetic force intensity $\widetilde{H}$ kept increasing and then remained more or less constant after a critical height. This trend was derived from the simulated results of g=250μm, g=500μm, g=750μm and g=1000μm magnet. It is evident that the trend in 7 (e) is consistent with the particle distribution in Fig. 7 (b-1)–(b-3) and Fig. 7 (c-1)–(c-3). In all the experiments conducted, the equivalent magnetic force intensity $\widetilde{H}$ provides a reasonable prediction of the separation performance, and can therefore serve as a criterion for the design of practical applications.

5.3. Separation of Yeast Cells and Magnetic Particles. To demonstrate the practical use of the proposed technique, a microfluidic device with multiple microstructures was used to separate a mixture of magnetic particles and yeast cells *Saccharomyces cerevisiae* of similar diameters of 4μm. This yeast strain has been frequently used in toxicity evaluations of heavy metals, anti-cancer drugs, and herbicides[42], because it shares many cellular structural similarities with cells in plants and animals [43]. Another convenience of using yeast cells is their short generation time and easy activation/cultivation procedures [44].

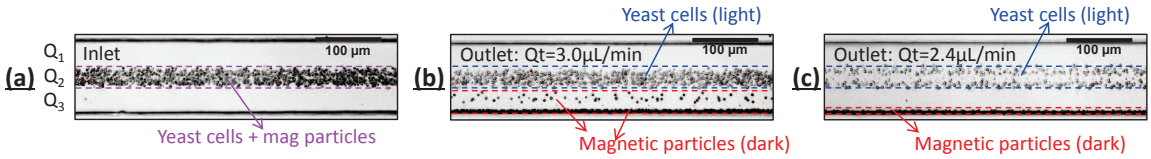

Figure 8. Separation of 4 μm magnetic particles and yeast cells by multi-rectangular microscale magnet of w=g=500μm and h=1000μm. (a) is the inlet stack image with Q_1=Q_2=Q_3. (b) and (c) are the outlet stack image when the inlet are Q_t=3.0μL/min and 2.4μL/min, respectively.

The microfluidic channel was placed next to the multi-rectangular microscale magnet with the size combination of w=g=500 μm and h=1000 μm. This rectangular structure was chosen because of its superior performance. Solutions with the magnetic particles and yeast cells entered into the central part of the fluid channel, as shown in Fig. 8 (a). Fig. 8 (b) and (c) display that the magnetic particles were pulled towards the lower half at the outlet while the yeast cells were not because the yeast cells are nonmagnetic (or diamagnetic). Complete separation was achieved at a total flow rate of 2.4μL/min. The separation can be further improved by integrating multiple parallel channels onto a single chip. Therefore, our proposed method will be useful for high-throughput particle/cell separation.

6. CONCLUSIONS

In summary, we have presented a simple and efficient method of fabricating microfluidic devices that integrates microscale magnets for magnetic particle separation applications. The fluidic and microscale magnets in our approach were fabricated with a simple one-step soft-lithography process. The microscale magnets induce local magnetic forces on magnetic particles to achieve continuous separation of microparticles. We have developed a simulation model to predict the trajectory of the particles by simulating the magnetic fields and computing the corresponding magnetic forces. The numerical simulations showed a good agreement with the experiments. We have conducted systematic experiments to study the effect of geometric designs of the microscale magnet on the separation of magnetic particles. Key results are summarized as follows: first, rectangular NdFeB-PDMS microscale magnet causes larger deflections of the particles than semicircle and isosceles triangle shaped structures; second, the geometric parameters of multi-rectangular microscale magnet influences the device's separation performance, which is correlated with the equivalent magnetic force intensity. The integration of microscale permanent magnets allows both small footprint, and standalone operation without bulky external magnets. The method

allows simple integration of multiple microscale magnets and microfluidic channels onto single chips to achieve high throughput separation of magnetic bio-conjugates, such as magnetically labeled antibody, aptamer or nano-particles.

The authors gratefully acknowledge the financial support from the Department of Mechanical and Aerospace Engineering, the Department of Chemistry, and the Center for Single Nanoparticle, Single Cell, and Single Molecule Monitoring (CS^3M) at Missouri University of Science and Technology, Rolla, Missouri.

REFERENCES

[1] Douglas B. Weibel and George M. Whitesides. Applications of microfluidics in chemical biology. *Curr. Opin. Chem. Biol.*, 10:584–591, 2006.

[2] David N Breslauer, Philip J Lee, and Luke P Lee. Microfluidics-based systems biology. *Mol. Biosyst.*, 2:97–112, 2006.

[3] Véronique Lecault, Adam K White, Anupam Singhal, and Carl L Hansen. Microfluidic single cell analysis: from promise to practice. *Current opinion in chemical biology*, 16(3-4):381–90, aug 2012.

[4] Huabing Yin and Damian Marshall. Microfluidics for single cell analysis. *Current opinion in biotechnology*, 23(1):110–9, feb 2012.

[5] J. Nilsson, M. Evander, B. Hammarstrom, and T. Laurell. Review of cell and particle trapping in microfluidic systems. *Analytica Chimica Acta*, 649(2):141 – 157, 2009.

[6] T. Zhu, F. Marrero, and L. Mao. Continuous separation of non-magnetic particles through negative magnetophoresis inside ferrofluids. In *2010 IEEE 5th International Conference on Nano/Micro Engineered and Molecular Systems*, pages 1006–1011, 2010.

[7] Nicole Pamme. Magnetism and microfluidics. *Lab. Chip*, 6:24–38, 2006.

[8] Martin AM Gijs, Frederic Lacharme, and Ulrike Lehmann. Microfluidic applications of magnetic particles for biological analysis and catalysis. *Chemical Reviews*, 110(3):1518–1563, 2009.

[9] N.-T. Nguyen. Micro-magnetofluidics: Interactions between magnetism and fluid flow on the microscale. *Microfluidics and Nanofluidics*, 12(1-4):1–16, 2012.

[10] Brian D Plouffe, Shashi K Murthy, and Laura H Lewis. Fundamentals and application of magnetic particles in cell isolation and enrichment: a review. *Reports on Progress in Physics*, 78(1):016601, 2015.

[11] Nicole Pamme and Andreas Manz. On-chip free-flow magnetophoresis: Continuous flow separation of magnetic particles and agglomerates. *Analytical Chemistry*, 76(24):7250–7256, 2004.

[12] Jonathan D. Adams, Patrick Thevoz, Henrik Bruus, and H. Tom Soh. Integrated acoustic and magnetic separation in microfluidic channels. *Applied Physics Letters*, 95(25), 2009.

[13] Brian D. Plouffe, Laura H. Lewis, and Shashi K. Murthy. Computational design optimization for microfluidic magnetophoresis. *Biomicrofluidics*, 5(1), 2011.

[14] Safarik Ivo and Safarikova Mirka. Use of magnetic techniques for the isolation of cells. *Journal of Chromatography B: Biomedical Sciences and Applications*, 722(1-2):35–53, 1999.

[15] Ivo Safarik and Mirka Safarikova. Magnetic techniques for the isolation and purification of proteins and peptides. *BioMagnetic Research and Technology*, 2:7, 2004.

[16] GaryP. Yakub and KathleenL. Stadterman-Knauer. Immunomagnetic separation of pathogenic organisms from environmental matrices. In JohnF.T. Spencer and AliciaL. Ragout de Spencer, editors, *Public Health Microbiology*, volume 268 of *Methods in Molecular Biology*, pages 189–197. Humana Press, 2004.

[17] Jeffrey J Chalmers, Yang Zhao, Masayuki Nakamura, Kristie Melnik, Larry Lasky, Lee Moore, and Maciej Zborowski. An instrument to determine the magnetophoretic mobility of labeled, biological cells and paramagnetic particles. *Journal of Magnetism and Magnetic Materials*, 194(1Ű3):231 – 241, 1999.

[18] L. Yang, J.C. Lang, P. Balasubramanian, K.R. Jatana, r D. Schulle, A. Agrawal, M. Zborowski, and J.J. Chalmers. Optimization of an enrichment process for circulating tumor cells from the blood of head and neck cancer patients through depletion of normal cells. *Biotechnology and Bioengineering*, 102(2):521–534, 2009.

[19] P. Balasubramanian, J.C. Lang, K.R. Jatana, B. Miller, E. Ozer, M. Old, D.E. Schuller, A. Agrawal, T.N. Teknos, Jr. T.A. Summers, M.B. Lustberg, M. Zborowski, and J.J. Chalmers. Multiparameter analysis, including emt markers, on negatively enriched blood samples from patients with squamous cell carcinoma of the head and neck. *PLoS ONE*, 7(7), 2012.

[20] R.M. Shenkman, J.J. Chalmers, B.J. Hering, N. Kirchhof, and K.K. Papas. Quadrupole magnetic sorting of porcine islets of langerhans. *Tissue Engineering - Part C: Methods*, 15(2):147–156, 2009.

[21] T. Lund-Olesen, M. Dufva, and M.F. Hansen. Capture of dna in microfluidic channel using magnetic beads: Increasing capture efficiency with integrated microfluidic mixer. *Journal of Magnetism and Magnetic Materials*, 311(1 SPEC. ISS.):396–400, 2007.

[22] Robert S. Molday and Donald Mackenzie. Immunospecific ferromagnetic iron-dextran reagents for the labeling and magnetic separation of cells. *Journal of Immunological Methods*, 52(3):353 – 367, 1982.

[23] Mauricio Hoyos, Lee R. Moore, Kara E. McCloskey, Shlomo Margel, Merav Zuberi, Jeffrey J. Chalmers, and Maciej Zborowski. Study of magnetic particles pulse-injected into an annular splitt-like channel inside a quadrupole magnetic field. *Journal of Chromatography A*, 903:99 – 116, 2000.

[24] Jeffrey J. Chalmers, Maciej Zborowski, Liping Sun, and Lee Moore. Flow through, immunomagnetic cell separation. *Biotechnology Progress*, 14(1):141–148, 1998.

[25] Qasem Ramadan, Victor Samper, Daniel P. Poenar, and Chen Yu. An integrated microfluidic platform for magnetic microbeads separation and confinement. *Biosensors and Bioelectronics*, 21(9):1693 – 1702, 2006.

[26] Nan Xia, TomP. Hunt, BrianT. Mayers, Eben Alsberg, GeorgeM. Whitesides, RobertM. Westervelt, and DonaldE. Ingber. Combined microfluidic-micromagnetic separation of living cells in continuous flow. *Biomedical Microdevices*, 8(4):299–308, 2006.

[27] Ran; P. Brames David; Wang Cheng Zhang, Ziyan; Zhou. A low-cost fabrication system for manufacturing soft-lithography microfluidic master molds. *Micro and Nanosystems*, 7(1):4–12, 2015.

[28] E.P. Furlani. Analysis of particle transport in a magnetophoretic microsystem. *Journal of Applied Physics*, 99(2), 2006.

[29] E.P. Furlani and K.C. Ng. Analytical model of magnetic nanoparticle transport and capture in the microvasculature. *Physical Review E - Statistical, Nonlinear, and Soft Matter Physics*, 73(6), 2006.

[30] Edward P. Furlani. Magnetic biotransport: Analysis and applications. *Materials*, 3(4):2412, 2010.

[31] Ashok Sinha, Ranjan Ganguly, Anindya K. De, and Ishwar K. Puri. Single magnetic particle dynamics in a microchannel. *Physics of Fluids*, 19(11), 2007.

[32] Roel Wirix-Speetjens, Wim Fyen, Jo De Boeck, and Gustaaf Borghs. Single magnetic particle detection: Experimental verification of simulated behavior. *Journal of Applied Physics*, 99(10), 2006.

[33] R. Byron Bird, Warren E. Stewart, and Edwin N. Lightfoot. *Transport Phenomena*. New York: Wiley, 2002.

[34] R. K. Shah, A. L. London, Thomas F. Irvine, and James P. Hartnett. *Laminar Flow Forced Convection in Ducts*. Academic Press, 1978.

[35] Frank M White. *Viscous fluid flow*. New York : McGraw-Hill, 2nd ed edition, 1991.

[36] Ehsan Samiei, Hojatollah Rezaei Nejad, and Mina Hoorfar. A dielectrophoretic-gravity driven particle focusing technique for digital microfluidic systems. *Applied Physics Letters*, 106(20), 2015.

[37] Hojatollah Rezaei Nejad, Ehsan Samiei, Ali Ahmadi, and Mina Hoorfar. Gravity-driven hydrodynamic particle separation in digital microfluidic systems. *RSC Adv.*, 5:35966–35975, 2015.

[38] J. M. Camacho and V. Sosa. Alternative method to calculate the magnetic field of permanent magnets with azimuthal symmetry. *Revista mexicana de física E*, 59(1), 2013.

[39] J.C. McDonald, D.C. Duffy, J.R. Anderson, D.T. Chiu, H. Wu, O.J.A. Schueller, and G.M. Whitesides. Fabrication of microfluidic systems in poly(dimethylsiloxane). *Electrophoresis*, 21(1):27–40, 2000.

[40] R. Zhou and C. Wang. Acoustic bubble enhanced pinched flow fractionation for microparticle separation. *Journal of Micromechanics and Microengineering*, 25(8), 2015.

[41] M.D. Abramoff, P.J. MagalhÃčes, and S.J. Ram. Image processing with imagej. *Biophotonics International*, 11(7):36–41, 2004.

[42] Citlali Garcia-Saucedo, James A. Field, Lila Otero-Gonzalez, and Reyes Sierra-Alvarez. Low toxicity of hfo2, sio2, al2o3 and ceo2 nanoparticles to the yeast, saccharomyces cerevisiae. *Journal of Hazardous Materials*, 192(3):1572 – 1579, 2011.

[43] Voychuk S Gromozova E. *Influence of Radiofrequency Emf on the Yeast Sacharomyces Cerevisiae as Model Eukaryotic System*. Number 167-175. Biophotonics and Coherent Systems in Biology: Springer: Springer, 2007.

[44] A. Goffeau, B. G. Barrell, H. Bussey, R. W. Davis, B. Dujon, H. Feldmann, F. Galibert, J. D. Hoheisel, C. Jacq, M. Johnston, E. J. Louis, H. W. Mewes, Y. Murakami, P. Philippsen, H. Tettelin, and S. G. Oliver. Life with 6000 genes. *Science*, 274(5287):546–567, 1996.

V. MAGNETIC SEPARATION OF MICROPARTICLES BY SHAPE

Ran Zhou, Feng Bai, Cheng Wang

Department of Mechanical & Aerospace Engineering

Missouri University of Science and Technology

Rolla, Missouri 65409

Tel: (573) 341-4636, Fax: (573) 341-4607

Email: wancheng@mst.edu

ABSTRACT

Accurate separation of microparticles by shape has diverse applications in biology and biotechnology, but is a significant challenge in separation science and engineering. We demonstrate a simple and effective mechanism that can achieve shape-based separation of magnetic particles in microscale flows. In this method, a uniform magnetic field is applied perpendicularly to the flow direction, and causes shape-dependent lateral migration of the particles. Using high-speed imaging, we studied the rotational dynamics of the ellipsoidal particles. It is found that the lateral migration is correlated with the asymmetric rotation of the particles. Different from existing techniques that use magnetic forces, our method uses shape-dependent magnetic torque but a zero magnetic force.

1. INTRODUCTION

In biological sciences and bioengineering, shapes are key indicators in specifically identifying micron-sized bio-particles, such as bacteria, viruses, budding yeasts, and marine micro-organisms [1, 2, 3, 4]. The changes in the shapes of red blood cells, from their normal biconcave shapes, to other shapes accompany many diseases, such as sickle-cell disease, anamia, or malaria [5, 6]. Thus, in bio-particle separation applications, the particle shape can

be a specific marker and serve as a useful basis for particle identification and fractionation, which have diverse applications in clinical diagnosis and biology. However, shape-based separation is a significant challenge for traditional methods, e.g., conventional filtration and centrifugation [7]. Recently, several techniques based on microfluidic technology, including hydrodynamic filtration (HDF) [7], deterministic lateral displacement (DLD) [8, 9], and dielectrophoresis (DEP) [10] have been utilized for shape-based separation. However, the requirements for complex features and high resolution have been potential limits for the practical application of HDF, DLD and DEP [7, 8, 10]. An alternative approach, using an inertia effect, has been demonstrated to induce lateral migration of ellipsoidal particles, but this only yields minimal effect [11], i.e., marginally different equilibrium positions. Inertial lift requires both a large flow Reynolds number ($Re > 10$) and a particle Reynolds number ($Re_p > 1$), which could induce substantial shear stresses on living biological matters. There also have been field-flow fractionation (FFF) technique reported by using steric-entropic effect to separate rod-like particles [12, 13]. Viscoelastic fluids have been demonstrated as another non-traditional means of shape-based separation of microparticles by exploiting a subtle and sensitive balance between elastic lift and inertial forces [14, 15]. More recently, by using shape-dependent magnetic and drag forces, negative magnetophoresis has been demonstrated to achieve shape-based separation of diamagnetic particles in a non-uniform mangetic field [16]. In this work, we present a simple and effective method of shape-based separation by combining uniform magnetic fields with pressure-driven flows in a microchannel at a low Reynolds number (Re <1). The magnetic field alters the rotational dynamics of the elongated particles, and results in shape-dependent migration and separation of microparticles.

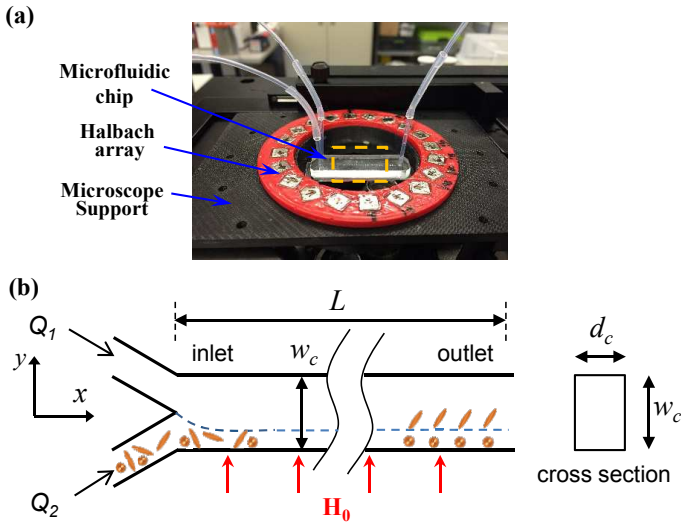

Figure 1. (a) Photograph of the microdevice located in a uniform magnetic field. (b) Schematic of the microfluidic channel.

2. EXPERIMENT

As shown in Fig. 1(a), a microfluidic chip was placed in the center of a uniform magnetic field with strength H_0 generated by a Halbach array [17]. The microfluidic device was fabricated in polydimethylsiloxane (PDMS) by following soft lithography techniques [18, 19]. The microfluidic device consisted of two inlets and one outlet. The main fluidic channel had a width of w_c = 50, and a depth of d_c = 35 μm, and a total length of L = 20000 μm, as in Fig. 1(b). A Halbach array is a special arrangement of permanent magnets that can produce uniform magnetic field [17]. Here, the Halbach array consisted of 20 cuboid permanent $0.25" \times 0.25" \times 0.5"$ magnets (K&J Magnetics, Inc) that were fixed in a holder fabricated by 3D printing. The magnitude of the magnetic field within the central region was $H_0 \approx 35000$ A/m, as measured by a Gaussmeter (see details on the design and measurement of the uniform mangetic field in the electronic supplementary information).

The sample particles used in this work were magnetite-doped and un-cross-linked polystyrene microspheres (micromer®-M 08-02-703, Micromod GmbH, Germany). The original spherical magnetic particles had a mean diameter d = 7 μm (coefficient of variation

$< 5\%$), and a density ρ_p = 1.1 g/mL. The magnetic susceptibility was $\chi_p \approx 0.26$, according to previous measurements [20]. The prolate ellipsoidal particles were prepared from the original spherical particles following a mechanical stretching approach of Ho et al. [21]. The mean aspect ratio of the ellipsoidal particles was $r_p = 3.93$ with a standard deviation of $\sigma_p = 0.43$, as measured from micro-photographs. The ellipsoidal and spherical particles had the same volume and magnetic properties, but had different shapes (details of the fabrication and measurement of the particles are in the electronic supplementary information).

It is worth noting that the magnetic microparticles consisted of a polymer core, a layer of magnetite grains, and a layer of functional polymer encapsulating the grains. The core-shell structure has been confirmed by transmission electron microscopy (TEM) imaging for both the original spherical and ellipsoidal particles [22]. Thus, these paramagnetic particles resemble physically relevant bio-particle complexes that are encountered in magnetic assisted cell sorting, e.g. binding of magnetic nanoparticles to micron-sized biological cells [23, 24].

In our experiments, inlet 1 was injected with 40% (w/w) aqueous-glycerol solution to work as a buffer flow, while inlet 2 was injected with 40% (w/w) aqueous-glycerol solution suspended with the sample particles. The 40% (w/w) glycerol solution has a similar density of that of sample particles in order to prevent particle sedimentation. The buffer and particle solutions were introduced from the two inlets at flow rates of Q_1 and Q_2 respectively. Based on the pinched flow theory [19], the particle solution was confined to a width $w_2 \approx Q_2 w_c/(Q_1 + Q_2)$. To record the trajectories of the magnetic particles during the experimental process, the microfluidic device was mounted on an inverted microscope stage (IX73, Olympus). A high-speed camera (Phantom Miro M310, Vision Research) was used to capture videos through the microscope. In the experiments, the focal plane of the microscope was near the middle plane in the vertical direction. The microfluidic device was illuminated by a fiber optic light for bright-field imaging transmission. Two syringe pumps (NE-300, New Era, and KDS 200, KDS Scientific) were used to control the flow

rate of each inlet separately. The position and orientation of the particles were extracted from the experimental videos by using software ImageJ [25].

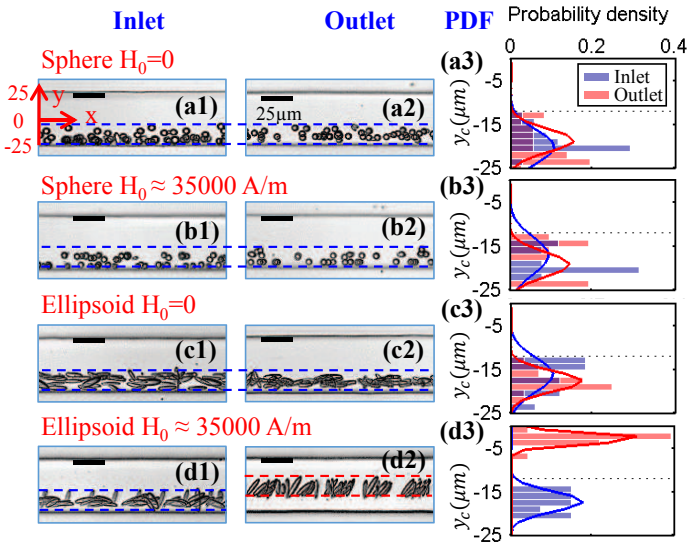

Figure 2. Stacked images at the inlet and outlet, and the corresponding probability density function (PDF) of the particle centroid in the y direction. (a1)-(a3) spherical particles and $H_0 = 0$; (b1)-(b3) spherical particles and $H_0 \approx 35000$ A/m; (c1)-(c3) ellipsoidal particles and $H_0 = 0$; (d1)-(d3) ellipsoidal particles and $H_0 \approx 35000$ A/m. The flow rates were $Q_1 = 1.0$ μL/min, and $Q_2 = 0.2$ μL/min for all experiments.

Fig. 2 shows the superimposed images, and the probability distributions of particle's centroid in the y direction, (y_c) at the inlet and outlet of the microchannel under four different experimental conditions. The probability density data were fitted by Gaussian functions to provide practically useful information, including the mean position and corresponding standard deviation (spreading). As can be seen in Fig. 2 (a1)-(a3), (b1)-(b3), for spherical particles, the mean y_c position and the distribution remained little changed between the inlet and outlet regardless of the presence of the magnetic field. For ellipsoidal particles in the absence of the magnetic field, they displayed 3D rotations, and stayed at a similar mean y_c position at the outlet as they did at the inlet, as shown in Fig. 2 (c1)-(c3). The small changes of $2 \sim 3$ μm for the mean y_c position between the inlet and outlet in the above three conditions (Fig. 2 (a3)–(c3)) could be attributed to measurements from a finite number of

particles (about 15 – 25 particles were used). The results in Fig. 2 (a1)-(c3) confirmed: (1) the effect of inertia focusing [26, 27, 28, 29] was negligible due to the low Reynolds numbers, i.e., $Re < 1$ and $Re_p \ll 1$; and (2) the magnetic force acting on the ellipsoidal particles was zero, due to the uniform magnetic field [30]. In Fig. (c2), the geometric interactions, e.g., steric effect or "pole vaulting" [31], may contribute to the focusing of the ellipsoidal particles. This steric effect tends to push the ellipsoidal particles away from the wall if the initial separation distance from the particle centroid to the wall is smaller than a semi-major axis [31]. Despite the improved focusing, the overall lateral positions of the ellipsoidal particles remained similar. The ellipsoidal particles behaved *much differently* in the presence of the magnetic field: (a) the particles aligned and rotated in the xy plane at the inlet; (b) the ellipsoidal particles migrated towards the channel center; and (c) the particles assumed steady orientations at the outlet, as shown in Fig. 2 (d1)-(d3). The results are surprising, because the magnetic force acting on paramagnetic particles is zero in uniform magnetic fields even for ellipsoidal particles from the basic electromagnetic theory [30, 32]. To understand this unusual lateral migration, we used high-speed (10000 fps) imaging to obtain information on the particle's position and orientation, in order to determine the reason behind the phenomenon. It is well known that axis-symmetric ellipsoidal particles rotate periodically around the vorticity axis in shear flows, and such motions are famously known as Jeffery orbits [33, 34]. Assuming Stokes flows, negligible inertial and Brownian effects, Jeffery showed that in an unbounded shear flow: (1) the particle translates with the undisturbed fluid velocity at the particle's centroid, (2) the particle has zero lateral migration, and (3) the particle rotates periodically around the vorticity axis (z). The period of rotation over a 2π period is $T_0^J = \frac{2\pi}{\dot{\gamma}}(r_p + \frac{1}{r_p})$, where $\dot{\gamma}$ is the shear rate, and r_p is the aspect ratio of the ellipsoidal particle. For convenience, in this study, we define a rotation period $T_0 = T_0^J/2$, which is half of the period in the classical Jeffery theory. The angle of

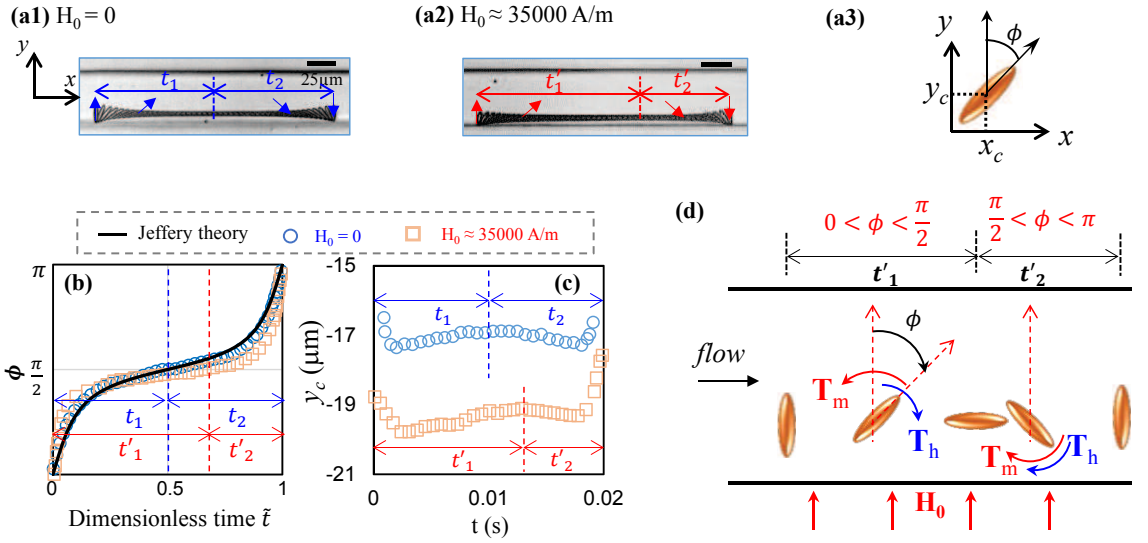

Figure 3. (a1) and (a2) Superimposed images for $H_0 = 0$ and $H_0 \approx 35000$ A/m, respectively. t_1 (t_1') and t_2 (t_2') are the times taken for particle rotation from $\phi = 0$ to $\phi = \pi/2$ and from $\phi = \pi/2$ to $\phi = \pi$, for $H_0 = 0$ and $H_0 \approx 35000$ A/m respectively. (a3) Schematic of the orientation angle ϕ, and the centroid of the particle (x_c, y_c). (b) Angle $\phi(\tilde{t})$ within a π period. The symbols represent experimental measurements, and the solid line represents the prediction using the Jeffery theory. (c) Experimental measurement of y_c as a function of t for $H_0 = 0$ and $H_0 \approx 35000$ A/m respectively. The flow rates were $Q_1 = 1.0$ μL/min, and $Q_2 = 0.2$ μL/min in both experiments. (d) Illustration of the particle rotation in the combined magnetic and flow fields. T_m is the torque induced by the magnetic field, and T_h is the torque induced by the flow field. For $0 < \phi < \pi/2$, T_m and T_h oppose each other, while T_m and T_h act in the same direction for $\pi/2 < \phi < \pi$.

the ellipsoid orientation, ϕ can be expressed as $\tan\phi = r_p \tan(\pi t/T_0 + \kappa)$, where t is time, and κ is the initial phase angle, ϕ is the angle of the ellipsoid's major axis relative to the y axis, as shown in Fig. 3 (a3).

While in unbounded Stokes flows, the rotation and translation of an ellipsoidal particle are decoupled [35], the particle motions are different and more complex when transported near a solid wall. The proximity of a wall induces a coupling between the translation and rotation. Specifically, the rotation of an ellipsoidal particle near a wall will generally result in a force (or lateral translation) in the transverse direction to the wall. At vanishing Reynolds number, the lift force is an anti-symmetric function of ϕ with respect $\phi = \pi/2$, and causes the particle to oscillate away and towards the wall over cycles

[36, 37, 38, 39]. Despite the oscillatory motion, the non-spherical particles have a zero net lateral migration during one period of rotation [35, 36, 38], if there are no external force fields and inertia effects are negligible.

The wall also induces increasing resistance on the particle rotation and results in longer rotation periods. However, the wall effect is only minimal in modifying the overall rotational behaviors of the particles. The approximate validity of Jeffery's theory for ellipsoidal particles or fibers near a wall have been confirmed by experiments [31, 34, 40] and numerical investigations [39, 41].

We first examined the rotational dynamics of the particles from the high-speed images, which were captured at a distance approximately 3 mm from the channel inlet. Fig. 3 (a1) and (a2) are the stacked images of particle rotations without and with magnetic field, respectively; and their corresponding orientation angles, $\phi(\tilde{t})$ within a π period are summarized in Fig. 3 (b). To compare the difference of the particle rotations without and with magnetic field, a dimensionless time $\tilde{t}$ was used here by normalizing time t to the time taken to complete a full π rotation. In the absence of magnetic field, i.e., $H_0 = 0$, the particle rotation agreed well with the prediction by the Jeffery theory. In obtaining the theoretical prediction in Fig. 3(b), the value of the shear rate was $\dot{\gamma} \approx 1100\ s^{-1}$. The good agreement was consistent with earlier observations [37, 38, 39, 40, 42].

In Fig. 3(b), the time intervals t_1 (t_1') and t_2 (t_2') refer to the times taken by the particle to rotate from $\phi = 0$ to $\phi = \pi/2$, and $\phi = \pi/2$ to $\phi = \pi$, respectively. They were determined based on the angle-versus-time curves in Fig. 3(b). These time intervals were then overlapped in Fig. 3(c). As indicated by the data, the particle showed symmetry of rotational angular velocities, i.e., $t_1 = t_2$. However, in the combined magnetic and flow fields, the particle rotation became asymmetric. The particle spent a longer time from $\phi = 0$ to $\phi = \pi/2$, and a shorter time from $\phi = \pi/2$ to $\phi = \pi$, i.e., $t_1' > t_2'$.

We next looked at the lateral dynamics of the particles by tracking the centroid position of the particles. The experimental data of y_c vs. t are shown in Fig. 3 (c). Although the two particles started off at two different initial positions, this difference does not affect the general characteristics of the particle motions between the two cases, i.e., without or with a magnetic field. In both cases, the particles moved first towards and then away from the wall (in the y direction), displaying oscillatory motions. This oscillation of the particle, was due to the presence of the channel wall, consistent with prior studies in the literature [36, 37, 38, 39]. When $H_0 = 0$, the oscillation away and toward the wall was almost symmetric ($t_1 \approx t_2$), similar to the rotational symmetry observed in Fig. 3 (b). The net migration over one period was close to zero. When $H_0 \approx 35000$ A/m, the particle's oscillatory motion became asymmetric. The particles moved upwards for a relatively longer time, and then downwards for a shorter time ($t_1' > t_2'$). Such asymmetric movement corresponded well to the asymmetric rotation observed in Fig. 3 (b). The particle had a larger net migration in the y direction, in the presence of the magnetic field.

The experimental data suggested strong correlations between the rotational dynamics of the particles and the lateral migration. As schematically shown in Fig. 3 (d), T_m is the torque induced by the magnetic field, and T_h is the torque induced by the flow field. The torque T_m always attempts to align the major axis of the particle to the direction of the magnetic field. When the particle orientation angle ϕ is between 0 and $\pi/2$, T_m is in the counter-clock wise direction, opposing T_h. When ϕ is between $\pi/2$ and π, T_m and T_h are in the clock wise direction. Therefore, the particle's angular velocity is smaller in the first half than that in the second half. This also means that a longer time is spent for the particles to rotate from ϕ=0 to ϕ=$\pi/2$ than from $\pi/2$ to π, which is consistent with the experimental measurements of $t_1' > t_2'$ in Fig. 3 (a2).

The observed lateral migration of the ellipsoidal particles was due to three essential elements: the non-spherical shape, magnetic torque, and proximity of a channel wall. With a uniform magnetic field is applied, the magnetic torque breaks the symmetry of the

rotational angular velocities of the particle. This asymmetry in turn breaks the symmetry of the lateral oscillatory motions of the particles, leading to a net lateral migration towards the channel center. As the particle migrated towards the channel center, the shear rate (or velocity gradient) decreases in pressure driven flows, and the relative effect of magnetic field become stronger. When the magnetically induced torque T_m is strong enough to balance the torque due to the flow, T_m, the ellipsoidal particles assumes a steady angle at the end of the microfluidic channel, as shown in Fig. 2 (d2). The measurements of the particle positions show negligible lateral migration when the particles were moving at steady-state angles. These experiments suggests the importance of the particle rotation to the lateral migration of ellipsoids.

There is another regime that will occur with a sufficiently strong magnetic field or a sufficiently weak flow field. In this regime, the particles enter the channel at a steady state angle $0 < \phi < \pi/2$ without rotation. In this case, lateral migration of particle towards the center may still be expected, similar to the case of an ellipsoidal particle that is fixed in a uniform flow [35, 43]. A three-dimensional numerical simulation, however, would be necessary to accurately determine the characteristics of the lift force. The transport behavior in this regime will be further investigated in future studies.

Fig. 4 shows the effect of particle aspect ratio on the lateral migration based on experimental data with ellipsoidal particles that have $r_p \approx 4$ and $r_p \approx 2$. Fig. 4 (a) compares the probability density function (PDF) of y_c at the outlet for the two particles under different total flow rates Q_t, while $Q_1/Q_2 = 5$ is fixed. The more elongated particles ($r_p \approx 4$) moved closer to the channel center than the shorter particles for all flow rates. Fig. 4(b) summarizes the average lateral migration Δy, which is defined as the difference of the mean y_c positions between the outlet and inlet. These results suggest that the lateral migration increased with an increase of the particle aspect ratio. This observation can be explained by the relative changes of the torques: an increase r_p from 2 to 4, results in more increment of T_m than that of T_h. As a result, the particle rotation becomes more asymmetric, thereby leading to

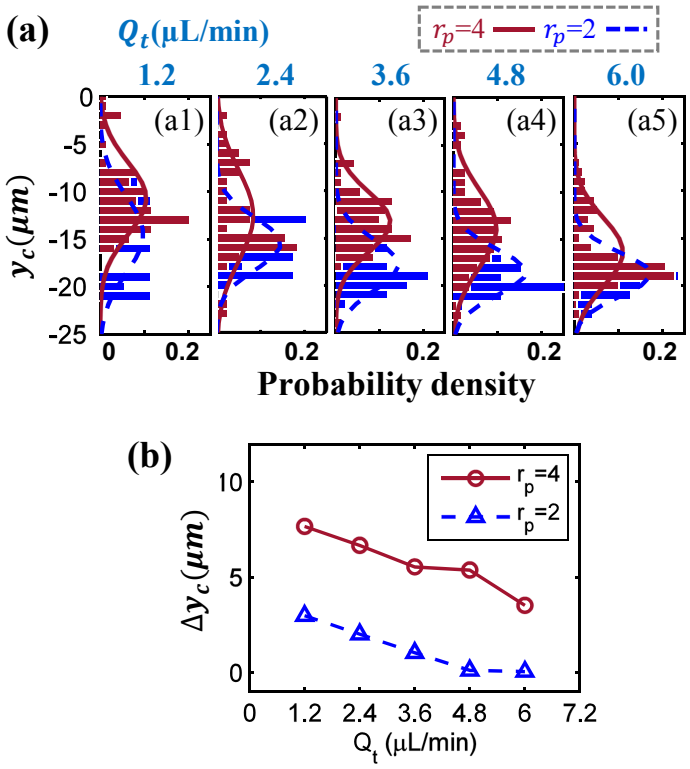

Figure 4. (a) Probability density function (PDF) of the y_c values of the ellipsoidal microparticles ($r_p \approx 4$ and $r_p \approx 2$) at the outlet under different total flow rate Q_t. (b) Effect of particle aspect ratio, r_p on the lateral migration Δy, measured between the inlet and the outlet of microfluidic channel. In these experiments, $H_0 \approx 35000$ A/m, $w_c = 50$ μm, and $Q_1/Q_2 = 5$.

a larger net migration. As the total flow rate Q_t increased from 1.2 μL/min to 6.0 μL/min, the mean y_c positions of both particles at the outlet became closer to the channel wall, i.e., decreasing Δy_c. The reason is that increasing Q_t causes a stronger flow field relative to the magnetic field, so that the asymmetric rotation is weakened, and the induced lateral migration becomes smaller.

The shape-dependent migration can be used to separate microparticles by shape. For example, a complete separation of particles by shape is demonstrated in Fig. 5 (a1) and (a2). In this experiment, a mixture of spherical and ellipsoidal ($r_p \approx 4$) particles was injected from inlet 2 at a flow rate of $Q_2 = 0.2$ μL/min, and the buffer flow was injected from inlet 1 at a flow rate of $Q_1 = 1.0$ μL/min, as shown in Fig. 1(b). By the

end of the channel, the ellipsoidal particles were focused towards the centerline, while the spherical particles remained at a similar initial position, achieving a complete separation. The probability density function (PDF) of particles distribution at the inlet and outlet shows a clear separation of the two kinds of particles (Fig. 5 (b1) and (b2)). In the experiments reported here, the viscosity of 40% (w/w) glycerol solution is about 3.8 times of that of pure water. An increased viscosity would weaken the relative effect of the magnetic strength, because the shear stress and hydrodynamic torque are proportional to the viscosity. If the device operates on particles suspended in water medium, we expect that the flow rate can potentially be increased by 3.8 times while still achieving similar lateral migration and separation.

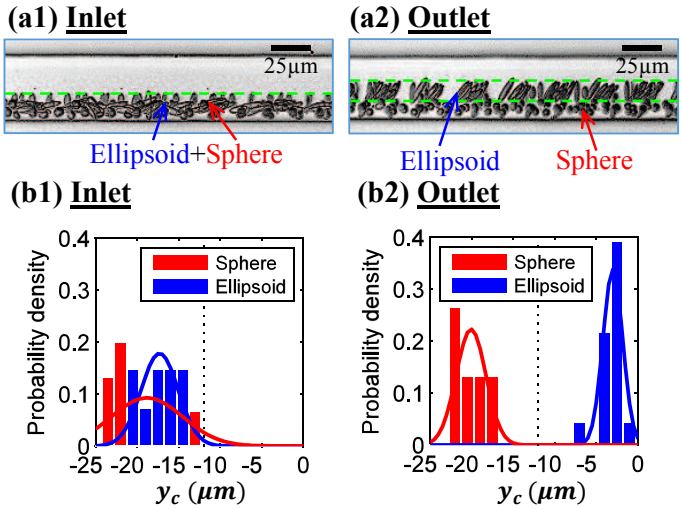

Figure 5. Separation of spherical and ellipsoidal particles in the uniform magnetic field. (a1) and (a2) are the superimposed images of the particles at the inlet and outlet of the channel respectively. (b1) and (b2) are the corresponding probability density function (PDF) of the y_c values of the particles.

In actual rectangular channels, particle position in the height direction and the channel height with respect to the particle dimensions can affect the migration behavior. This is due to a change of relative strength between the magnetic and hydrodynamic fields for particles at different height. The effect is more likely to influence migration speed,

but not migration direction. Provided sufficiently long microfluidic channels, the particles will have enough time to reach to the center of the channel. This may be an important consideration when designing practical sorting devices to ensure complete separation.

3. CONCLUSION

In conclusion, we have demonstrated a simple and effective technique for achieving shape-based separation of microparticles by using a uniform magnetic field. Experimental measurements revealed that the magnetic field breaks the symmetry of the particle rotation dynamics.

The nonspherical shape, together with the asymmetrical rotation of the particles and particle-wall hydrodynamic interactions, resulted in a net lift force (or migration velocity) towards the channel center.

Compared to existing methods of shape-based separation, the current method has several advantages: (1) simplicity – magnetic fields can be implemented through permanent magnets; (2) general applicability – the mechanism only requires a difference in magnetic susceptibility between the particles and surrounding fluids. Although demonstrated with magnetic particles in a nonmagnetic fluid in this work, our experiments have confirmed similar lateral migration of nonmagnetic ellipsoidal particles suspended in a ferrofluid (in electronic supplementary information).

In comparison to single-magnet methods that are often used [44, 45, 46], the uniform magnetic field technique offers two benefits. First, it is easer to place the microfluidic device, because of the large area of the uniform magnetic field. Second, multiple microfluidic channels can be conveniently integrated onto a single chip while being subjected to the same magnetic field. Thus, the use of uniform magnetic field would be favorable for high-throughput parallelization. The demonstrated technique thus provides a general mechanism

for separation of micron-sized particles, e.g., various bio-particles, by shape, and has great potential for biological and biomedical applications that require isolating and sorting of shaped microparticles.

REFERENCES

[1] Mitragotri Samir and Lahann Joerg. Physical approaches to biomaterial design. *Nat. Mater.*, 8:15–23, 2009.

[2] S. Mitragotri and J. Lahann. Boom time for biomaterials. *Nat. Mater.*, 8(6):439, 2009.

[3] Sophie G. Martin. Geometric control of the cell cycle. *Cell Cycle*, 8(22):3643–3647, 2009.

[4] Hamed Amini, Wonhee Lee, and Dino Di Carlo. Inertial microfluidic physics. *Lab Chip*, 14:2739–2761, 2014.

[5] Chansuda Wongsrichanalai, Mazie J Barcus, Sinuon Muth, Awalludin Sutamihardja, and Walther H Wernsdorfer. A review of malaria diagnostic tools: Microscopy and rapid diagnostic test (RDT). *Am. J. Trop. Med. Hyg.*, 77(SUPPL. 6):119–127, dec 2007.

[6] M. Piagnerelli, K. Zouaoui Boudjeltia, D. Brohee, A. Vereerstraeten, P. Piro, J.-L. Vincent, and M. Vanhaeverbeek. Assessment of erythrocyte shape by flow cytometry techniques. *J. Clin. Pathol.*, 60(5):549–554, 2007.

[7] Sari Sugaya, Masumi Yamada, and Minoru Seki. Observation of nonspherical particle behaviors for continuous shape-based separation using hydrodynamic filtration. *Biomicrofluidics*, 5(2):024103, 2011.

[8] Jason P. Beech, Stefan H. Holm, Karl Adolfsson, and Jonas O. Tegenfeldt. Sorting cells by size, shape and deformability. *Lab Chip*, 12:1048–1051, 2012.

[9] Stefan H. Holm, Jason P. Beech, Michael P. Barrett, and Jonas O. Tegenfeldt. Separation of parasites from human blood using deterministic lateral displacement. *Lab Chip*, 11:1326–1332, 2011.

[10] Ana Valero, Thomas Braschler, Alex Rauch, Nicolas Demierre, Yves Barral, and Philippe Renaud. Tracking and synchronization of the yeast cell cycle using dielectrophoretic opacity. *Lab Chip*, 11:1754–1760, 2011.

[11] Mahdokht Masaeli, Elodie Sollier, Hamed Amini, Wenbin Mao, Kathryn Camacho, Nishit Doshi, Samir Mitragotri, Alexander Alexeev, and Dino Di Carlo. Continuous inertial focusing and separation of particles by shape. *Phys. Rev. X*, 2:031017, Sep 2012.

[12] Mehrdad Alfi and Joontaek Park. Theoretical analysis of the local orientation effect and the lift-hyperlayer mode of rodlike particles in field-flow fractionation. *J. Sep. Sci.*, 37(7):876–883, apr 2014.

[13] Joontaek Park and Anand Mittal. An Improved Model for the Steric-Entropic Effect on the Retention of Rod-like Particles in Field-Flow Fractionation: Discussion of Aspect Ratio-Based Separation. *Chromatography*, 2(3):472–487, jul 2015.

[14] Xinyu Lu and Xiangchun Xuan. Elasto-Inertial Pinched Flow Fractionation for Continuous Shape-Based Particle Separation. *Anal. Chem.*, 87(22):11523–30, 2015.

[15] Xinyu Lu, Lin Zhu, Ri-mao Hua, and Xiangchun Xuan. Continuous sheath-free separation of particles by shape in viscoelastic fluids. *Appl. Phys. Lett.*, 107(26):264102, 2015.

[16] Yilong Zhou and Xiangchun Xuan. Diamagnetic particle separation by shape in ferrofluids. *Appl. Phys. Lett.*, 109(10):102405, 2016.

[17] H. Raich and P. Blumler. Design and construction of a dipolar halbach array with a homogeneous field from identical bar magnets: Nmr mandhalas. *Concepts in Magnetic Resonance Part B: Magnetic Resonance Engineering*, 23B(1):16–25, 2004.

[18] J.C. McDonald, D.C. Duffy, J.R. Anderson, D.T. Chiu, H. Wu, O.J.A. Schueller, and G.M. Whitesides. Fabrication of microfluidic systems in poly(dimethylsiloxane). *Electrophoresis*, 21(1):27–40, 2000.

[19] R. Zhou and C. Wang. Acoustic bubble enhanced pinched flow fractionation for microparticle separation. *Journal of Micromechanics and Microengineering*, 25(8), 2015.

[20] Roel Wirix-Speetjens, Wim Fyen, Jo De Boeck, and Gustaaf Borghs. Single magnetic particle detection: Experimental verification of simulated behavior. *Journal of Applied Physics*, 99(10), 2006.

[21] C. C. Ho, A. Keller, J. A. Odell, and R. H. Ottewill. Preparation of monodisperse ellipsoidal polystyrene particles. *Colloid. Polym. Sci.*, 271(5):469–479, 1993.

[22] Oriol Guell, Francesc Sagues, and Pietro Tierno. Magnetically driven janus micro-ellipsoids realized via asymmetric gathering of the magnetic charge. *Advanced Materials*, 23(32):3674–3679, 2011.

[23] Chen Peng, Huang Yu-Yen, Hoshino Kazunori, and Zhang John X.J. Microscale magnetic field modulation for enhanced capture and distribution of rare circulating tumor cells. *Scientific Reports*, 5(8745), 2015.

[24] Wu C-H et al. Huang Y-Y, Chen P. Screening and molecular analysis of single circulating tumor cells using micromagnet array. *Scientific Reports*, 5(16047), 2015.

[25] M.D. Abramoff, P.J. MagalhÃčes, and S.J. Ram. Image processing with imagej. *Biophotonics International*, 11(7):36–41, 2004.

[26] Dino Di Carlo, Daniel Irimia, Ronald G. Tompkins, and Mehmet Toner. Continuous inertial focusing, ordering, and separation of particles in microchannels. *Proceedings of the National Academy of Sciences*, 104(48):18892–18897, 2007.

[27] Dino Di Carlo. Inertial microfluidics. *Lab. Chip*, 9:3038–3046, 2009.

[28] Dino Di Carlo, Jon F Edd, Katherine J Humphry, Howard A Stone, and Mehmet Toner. Particle segregation and dynamics in confined flows. *Phys. Rev. Lett.*, 102(9):094503, mar 2009.

[29] Ali Asgar S. Bhagat, Sathyakumar S. Kuntaegowdanahalli, and Ian Papautsky. Inertial microfluidics for continuous particle filtration and extraction. *Microfluidics and Nanofluidics*, 7(2):217–226, 2009.

[30] Julius Adams Stratton. *Electromagnetic Theory*. Adams Press, 2007.

[31] C. A. Stover and C. Cohen. The motion of rodlike particles in the pressure-driven flow between two flat plates. *Rheol. Acta*, 29(3):192–203, 1990.

[32] Pietro Tierno, Josep Claret, Francesc Sagués, and Andrejs Cēbers. Overdamped dynamics of paramagnetic ellipsoids in a precessing magnetic field. *Phys. Rev. E*, 79:021501, Feb 2009.

[33] G. B. Jeffery. The motion of ellipsoidal particles immersed in a viscous fluid. *Proceedings of the Royal Society of London. Series A*, 102(715):161–179, 1922.

[34] B. Kelli Moses, G. Suresh Advani, and Andreas Reinhardt. Investigation of fiber motion near solid boundaries in simple shear flow. *Rheol. Acta*, 40(3):296–306, 2001.

[35] J Happel and H Brenner. *Low Reynolds Number Hydrodynamics*. Englewood Cliffs, 1983.

[36] F. P. Bretherton. The motion of rigid particles in a shear flow at low Reynolds number. *J. Fluid Mech.*, 14(02):284, 1962.

[37] Seung-Man Yang and Gary L. Leal. Particle motion in Stokes flow near a plane fluid-fluid interface. Part 2. Linear shear and axisymmetric straining flows. *J. Fluid Mech.*, pages 275–304, 1984.

[38] E. Gavze and M. Shapiro. Particles in a shear flow near a solid wall: Effect of nonsphericity on forces and velocities. *Int. J. Multiph. Flow*, 23(1):155–182, 1997.

[39] Nipa A. Mody and Michael R. King. Three-dimensional simulations of a platelet-shaped spheroid near a wall in shear flow. *Phys. Fluids*, 17(11):113302, 2005.

[40] Tolga Kaya and Hur Koser. Characterization of hydrodynamic surface interactions of Escherichia coli cell bodies in shear flow. *Phys. Rev. Lett.*, 103(13):138103, sep 2009.

[41] M. S. Ingber. A numerical study of three-dimensional Jeffery orbits in shear flow. *J. Rheol.*, 38(6):1829, nov 1994.

[42] A. Karnis, H. L. Goldsmith, and S. G. Mason. The flow of suspensions through tubes: V. Inertial effects. *The Canadian Journal of Chemical Engineering*, 44(4):181–193, aug 1966.

[43] Rafik Ouchene, Mohammed Khalij, Anne Tanière, and Boris Arcen. Drag, lift and torque coefficients for ellipsoidal particles: From low to moderate particle reynolds numbers. *Computers & Fluids*, 113:53 – 64, 2015.

[44] Nicole Pamme and Andreas Manz. On-chip free-flow magnetophoresis: Continuous flow separation of magnetic particles and agglomerates. *Analytical Chemistry*, 76(24):7250–7256, 2004.

[45] T. Zhu, F. Marrero, and L. Mao. Continuous separation of non-magnetic particles through negative magnetophoresis inside ferrofluids. In *2010 IEEE 5th International Conference on Nano/Micro Engineered and Molecular Systems*, pages 1006–1011, 2010.

[46] Jian Zeng, Yanxiang Deng, Pallavi Vedantam, Tzuen Rong Tzeng, and Xiangchun Xuan. Magnetic separation of particles and cells in ferrofluid flow through a straight microchannel using two offset magnets. *J. Magn. Magn. Mater.*, 346:118–123, 2013.

SECTION

3. SUMMARY AND CONCLUSIONS

This dissertation has developed novel and simple ways to enhance the separation performance of particles by using acoustic bubble enhanced pinched flow fractionation, soft magnetic microstructures, microscale permanent magnets, multiphase ferrofluid flows and external uniform magnetic field.

First, a novel acoustic bubble enhanced flow fractionation technique to overcome the limitations of conventional PFF devices were proposed. The combination of acoustic streaming flow from the bubble and the pressure driven flow inside the pinched segment provides beneficial features – local acceleration and non-uniform velocity profile. The combined flow field results in improved and robust separation between microparticles.

Second, a simple and efficient method of fabricating microfluidic devices that integrates microscale magnets for separation applications of magnetic particles were presented. The fluidic and microscale magnets in our approach are fabricated with a simple one-step soft-lithography process. The microscale magnets induce local magnetic forces on magnetic particles to achieve continuous separation of microparticles. A simulation model was developed to predict the trajectory and explain the movement of the particles by simulating the magnetic fields and computing the corresponding magnetic forces, which showed a good agreement with experiments.

Third, a simple and low-cost method for separating particles in ferrofluid by combining the multiphase laminar fluid interface and microscale magnets were demonstrated. The microfluidic devices integrated the NdFeB-PDMS microscale magnet next to the microfluidic channels, with a distance of tens of micrometers. The induced magnetic field gradients resulted in strong forces that could deflect magnetic particles and focus them at

the interface between the water and ferrofluid. Systematic experiments were conducted to study the effects of concentrations of ferrofluid, the gap distance and the width of the fluidic channel on the focusing performance of particles.

Fourth, a simple and low-cost method for fabricating microfluidic devices for enhanced separation of magnetic particles were proposed. The microfluidic devices integrated soft magnetic microstructures next to microfluidic channels, with a distance of tens of micrometers. The induced magnetic fields and gradients resulted in strong forces that can deflect magnetic particles perpendicular to the pressure-driven flow. By simulating the magnetic fields and computing the corresponding magnetic forces, a numerical simulation method was developed to predict the particle trajectory, and showed good agreement with the experimental data.

Last, a simple and effective technique for achieving shape-based separation of microparticles by using a uniform magnetic field were proposed. Experimental measurements revealed that the magnetic field breaks the symmetry of the particle rotation dynamics. The nonspherical shape, together with the asymmetrical rotation of the particles and particle-wall hydrodynamic interactions, resulted in a net lift force (or migration velocity) towards the channel center.

BIBLIOGRAPHY

[1] David N Breslauer, Philip J Lee, and Luke P Lee. Microfluidics-based systems biology. *Mol. Biosyst.*, 2:97–112, 2006.

[2] Douglas B. Weibel and George M. Whitesides. Applications of microfluidics in chemical biology. *Curr. Opin. Chem. Biol.*, 10:584–591, 2006.

[3] Ali Asgar S Bhagat, Hansen Bow, Han Wei Hou, Swee Jin Tan, Jongyoon Han, and Chwee Teck Lim. Microfluidics for cell separation. *Med. Biol. Eng. Comput.*, 48:999–1014, 2010.

[4] Ashleigh B. Theberge, Fabienne Courtois, Yolanda Schaerli, Martin Fischlechner, Chris Abell, Florian Hollfelder, and Wilhelm T S Huck. Microdroplets in microfluidics: An evolving platform for discoveries in chemistry and biology. *Angewandte Chemie - International Edition*, 49:5846–5868, 2010.

[5] Eric K Sackmann, Anna L Fulton, and David J Beebe. The present and future role of microfluidics in biomedical research. *Nature*, 507:181–9, 2014.

[6] André A. Adams, Paul I. Okagbare, Juan Feng, Matuesz L. Hupert, Don Patterson, Jost Götten, Robin L. McCarley, Dimitris Nikitopoulos, Michael C. Murphy, and Steven A. Soper. Highly efficient circulating tumor cell isolation from whole blood and label-free enumeration using polymer-based microfluidics with an integrated conductivity sensor. *J. Am. Chem. Soc.*, 130:8633–8641, 2008.

[7] Masaya Murata, Yukihiro Okamoto, Yeon Su Park, Noritada Kaji, Manabu Tokeshi, and Yoshinobu Baba. Cell separation by the combination of microfluidics and optical trapping force on a microchip. *Anal. Bioanal. Chem.*, 394:277–283, 2009.

[8] Soojung Claire Hur, Nicole K Henderson-MacLennan, Edward R B McCabe, and Dino Di Carlo. Deformability-based cell classification and enrichment using inertial microfluidics. *Lab. Chip*, 11:912–920, 2011.

[9] Yuchao Chen, Peng Li, Po-Hsun Huang, Yuliang Xie, John D Mai, Lin Wang, Nam-Trung Nguyen, and Tony Jun Huang. Rare cell isolation and analysis in microfluidics. *Lab. Chip*, 14:626–45, 2014.

[10] P. Sajeesh and Ashis Kumar Sen. Particle separation and sorting in microfluidic devices: A review. *Microfluid. Nanofluid.*, 17:1–52, 2014.

[11] Daniel R. Gossett, Westbrook M. Weaver, Albert J. MacH, Soojung Claire Hur, Henry Tat Kwong Tse, Wonhee Lee, Hamed Amini, and Dino Di Carlo. Label-free cell separation and sorting in microfluidic systems. *Anal. Bioanal. Chem.*, 397:3249–3267, 2010.

[12] Hideaki Tsutsui and Chih Ming Ho. Cell separation by non-inertial force fields in microfluidic systems. *Mech. Res. Commun.*, 36:92–103, 2009.

[13] Nicole Pamme. Continuous flow separations in microfluidic devices. *Lab. Chip*, 7:1644–1659, 2007.

[14] Peter R C Gascoyne and Jody Vykoukal. Particle separation by dielectrophoresis. *Electrophoresis*, 23:1973–1983, 2002.

[15] Benjamin G. Hawkins, A. Ezekiel Smith, Yusef A. Syed, and Brian J. Kirby. Continuous-flow particle separation by 3D insulative dielectrophoresis using coherently shaped, dc-biased, ac electric fields. *Anal. Chem.*, 79:7291–7300, 2007.

[16] Zhigang Wu, Ai Qun Liu, and Klas Hjort. Microfluidic continuous particle/cell separation via electroosmotic-flow-tuned hydrodynamic spreading. *J. Micromech. Microeng.*, 17:1992–1999, 2007.

[17] David G Grier. A revolution in optical manipulation. *Nature*, 424:810–816, 2003.

[18] E Eriksson, J Scrimgeour, A Granéli, K Ramser, R Wellander, J Enger, D Hanstorp, and M Goksör. Optical manipulation and microfluidics for studies of single cell dynamics. *Journal of Optics A: Pure and Applied Optics*, 9:S113–S121, 2007.

[19] Nicole Pamme. Magnetism and microfluidics. *Lab. Chip*, 6:24–38, 2006.

[20] Jian Zeng, Yanxiang Deng, Pallavi Vedantam, Tzuen Rong Tzeng, and Xiangchun Xuan. Magnetic separation of particles and cells in ferrofluid flow through a straight microchannel using two offset magnets. *J. Magn. Magn. Mater.*, 346:118–123, 2013.

[21] Lotien Richard Huang, Edward C Cox, Robert H Austin, and James C Sturm. Continuous particle separation through deterministic lateral displacement. *Science (New York, N.Y.)*, 304:987–990, 2004.

[22] A. Karimi, S. Yazdi, and A. M. Ardekani. Hydrodynamic mechanisms of cell and particle trapping in microfluidics. *Biomicrofluidics*, 7, 2013.

[23] Dino Di Carlo. Inertial microfluidics. *Lab. Chip*, 9:3038–3046, 2009.

[24] A. A S Bhagat, Sathyakumar S. Kuntaegowdanahalli, and Ian Papautsky. Inertial microfluidics for continuous particle filtration and extraction. *Microfluid. Nanofluid.*, 7:217–226, 2009.

[25] Maulik V. Patel, Imaly A. Nanayakkara, Melinda G. Simon, and Abraham P. Lee. Cavity-induced microstreaming for simultaneous on-chip pumping and size-based separation of cells and particles. *Lab Chip*, 14:3860–3872, 2014.

[26] Daniel Ahmed, Xiaole Mao, Jinjie Shi, Bala Krishna Juluri, and Tony Jun Huang. A millisecond micromixer via single-bubble-based acoustic streaming. *Lab. Chip*, 9:2738–2741, 2009.

[27] Cheng Wang, Shreyas V. Jalikop, and Sascha Hilgenfeldt. Efficient manipulation of microparticles in bubble streaming flows. *Biomicrofluidics*, 6, 2012.

[28] Hoang V. Phan, Muhsincan Sesen, Tuncay Alan, and Adrian Neild. Single line particle focusing using a vibrating bubble. *Appl. Phys. Lett.*, 105(19):–, 2014.

[29] C. Wang, S.V. Jalikop, and S. Hilgenfeldt. Size-sensitive sorting of microparticles through control of flow geometry. *Appl. Phys. Lett.*, 99(3), 2011.

[30] Y. Xu, A. Hashmi, G. Yu, X. Lu, H. . Kwon, X. Chen, and J. Xu. Microbubble array for on-chip worm processing. *Appl. Phys. Lett.*, 102(2), 2013.

[31] Priscilla Rogers and Adrian Neild. Selective particle trapping using an oscillating microbubble, 2011.

[32] Safarik Ivo and Safarikova Mirka. Use of magnetic techniques for the isolation of cells. *Journal of Chromatography B: Biomedical Sciences and Applications*, 722(1-2):35–53, 1999.

[33] Ivo Safarik and Mirka Safarikova. Magnetic techniques for the isolation and purification of proteins and peptides. *BioMagnetic Research and Technology*, 2:7, 2004.

[34] E. Verpoorte. Beads and chips: New recipes for analysis. *Lab on a Chip*, 3(4):60N–68N, 2003.

[35] M.A.M. Gijs. Magnetic bead handling on-chip: New opportunities for analytical applications. *Microfluidics and Nanofluidics*, 1(1):22–40, 2004.

[36] Martin AM Gijs, Frederic Lacharme, and Ulrike Lehmann. Microfluidic applications of magnetic particles for biological analysis and catalysis. *Chemical Reviews*, 110(3):1518–1563, 2009.

[37] N.-T. Nguyen. Micro-magnetofluidics: Interactions between magnetism and fluid flow on the microscale. *Microfluidics and Nanofluidics*, 12(1-4):1–16, 2012.

[38] Majid Hejazian, Weihua Li, and Nam-Trung Nguyen. Lab on a chip for continuous-flow magnetic cell separation. *Lab on a Chip*, 15(4):959–970, 2015.

[39] Nicole Pamme and Andreas Manz. On-chip free-flow magnetophoresis: Continuous flow separation of magnetic particles and agglomerates. *Analytical Chemistry*, 76(24):7250–7256, 2004.

[40] R. E. ROSENSWEIG. Fluidmagnetic buoyancy. *AIAA Journal*, 4(10):1751–1758, 1966.

[41] K. D. Young. The Selective Value of Bacterial Shape. *Microbiol. Mol. Biol. Rev.*, 70(3):660–703, 2006.

VITA

Ran Zhou was born in Qingdao, Shandong, China. She received her Bachelor of Science degree in Thermal Energy and Power Engineering and Bachelor of Business Administration degree in Accounting in June 2012 from Shandong University, Jinan, China. During her Bachelor study, she attended the exchange program to study Mechanical Engineering in The Hong Kong Polytechnic University in 2011. In June 2015, she received her Master of Science degree in Refrigeration and Cryogenic Engineering from Shandong University, Jinan, China. In December 2017, she received her Doctor of Philosophy in Mechanical Engineering from Missouri University of Science and Technology, Rolla, Mis-souri, USA. Her research interests include fluid dynamics, micro/nano-scale heat and mass transport, micro/nanofluidics, bioMEMS, lab-on-a-chip, micro/nano-fabrication, bubble dynamics, acoustic streaming and multi-phase flow, thermodynamic system analysis and heating, ventilation, air conditioning and refrigeration (HVAC/R) system.

During her Ph.D. study, Ran worked as a graduate teaching assistant and took charge of the course of Introduction to Engineering Design. She was awarded as Inaugural College of Engineering and Computing (CEC) Dean's Ph.D. Scholar, not only for her scholarly contributions, but also for her academic success and service contributions. She is also a reviewer of Journal of Microfluidics and Nanofluidics.

She received Travel Grant from the American Physical Socienty (APS) to present her research at the 68th Annual Division of Fluid Dynamics Meeting, 2015, Boston, USA. She served for the Council of Graduate Students (CGS) of Missouri University of Science and Technology as a department representative from 2014 to 2015.

During her Ph.D. study, she authored and co-authored 8 journal papers and 8 conference abstracts/papers/presentations.